AFFIDAVIT

I declare that I have authored this thesis independently, that I have not used other than the declared sources/resources, and that I have explicitly indicated all material which has been quoted either literally or by content from the sources used. The text document uploaded to TUGRAZonline is identical to the present master‘s thesis dissertation.

Date

Signature

Acknowledgements:

My thanks go to Prof. Viktor Hacker, who gave me the possibility to join his workgroup. His informative input in many discussions and his guidance was a big support for my work. I also want to thank Prof. Matthäus Siebenhofer in his function as head of the institute who enabled that work under his auspices.

Many thanks go to Stephan Nestl and Gernot Voitic. They always had time to discuss interesting results and helped me particularly in modifying the measurement apparatus. Special thanks to Stephan in his function as supervisor who provided me the background information of this topic.

Additionally a lot of thanks go to Dr. Julian Wagner from the FELMI Graz Institute for Electron Microscopy and Nanoanalysis and Dr. Helmar Wiltsche from the Institute for Analytical Chemistry and Food Chemistry TU Graz for their great collaboration and analytical support.

I also want to thank the whole working group that always took care for a pleasant working ambience as well as Carmen Gehrer in her function as project manager.

Last but not least I want to thank my family and friends that they always supported me in every situation independent of daytime or emotional conditions.

Abstract:

This work considers the production of hydrogen from renewable energy carriers as an essential contribution for prospective sustainable energy supply. Hydrogen is produced by the steam-iron-process. This process is working in two steps. Iron oxide from the contact mass is reduced with hydrogen in the first step and in the second the obtained iron is oxidized with steam. During the oxidation high grade hydrogen is produced.

The experimental investigations concern the stability of the contact mass. The main component of the contact mass was sponge iron powder which was stabilized with 5, 10 and 20 weight percent of aluminium oxide. The measurements were conducted on a thermobalance. Each measurement consisted of a repetition of ten redox cycles. Nitrogen was chosen as a carrier and protective gas. The measurement series were done at 600°C and 750 °C isothermally. One series was carried out with a reduction temperature of 750 °C and an oxidation temperature of 600 °C. Under isothermal conditions the contact mass remained stable over the whole measurement. One sample was chosen for an extended trial of 50 cycles. In the first cycle the sample showed a mass decrease that deviated only by 1 wt % from the calculated value and stayed constant over the whole measurement.

Zusammenfassung:

Diese Arbeit befasst sich mit der Erzeugung von Wasserstoff aus erneuerbaren Energieträgern als wesentlicher Beitrag zur zukünftigen nachhaltigen Energieversorgung. Wasserstoff wird mit dem Dampf-Eisen-Prozess hergestellt. Der Prozess arbeitet in zwei Stufen. In der ersten Stufe wird das Eisenoxid der Kontaktmasse mit Wasserstoff reduziert und in der zweiten das erhaltene Eisen mit Dampf oxidiert. Bei der Oxidation entsteht hochreiner Wasserstoff.

Die experimentellen Untersuchungen befassen sich mit der Stabilität der Kontaktmasse. Der Hauptbestandteil der Kontaktmasse war Eisenschwammpulver welches mit 5 ,10 und 20 Gewichtsprozent Aluminiumoxid stabilisiert wurde. Die Messungen wurden mit einer Thermowaage durchgeführt. Jede Messung bestand aus einer Wiederholung von zehn Redox-Zyklen. Stickstoff wurde als Trägergas und Schutzgas verwendet. Die Messserien wurden bei 600 °C und 750 °C unter isothermen Bedingungen durchgeführt. Eine weitere Messserie bei der Reduktionstemperatur von 750°C und der Oxidationstemperatur von 600 °C. Unter isothermen Reaktionsbedingungen blieb die Kontaktmasse über die gesamte Messreihe stabil. Eine Probe wurde für eine erweiterte Serie mit 50 Zyklen ausgewählt. Diese Probe zeigte im ersten Zyklus lediglich eine Abnahme von 1 Gewichtsprozent vom berechneten Wert und blieb konstant über die gesamte Messung.

Content

1 Introduction

1.1 Energy and environment

Since the industrial revolution in the 1860's population and the demand for energy are rising continuously [1], [2]. Consequently greenhouse gas emissions like carbon dioxide are increasing enormously. Those gases influence our environment and nature dramatically. These influences lead to the loss of living area and extinction of animals and plants which are located in those regions.

Ideally the amount of carbon dioxide that is emitted by animals and biological decay processes is consumed by plants, bacteria and geochemical processes. Thus the amount of carbon dioxide is constant overall. Starting with the industrial revolution and its prodigious use of fossil energy carriers an excess of carbonaceous gases is observed. The development of the energy carrier consumption is shown in *Figure.1*.

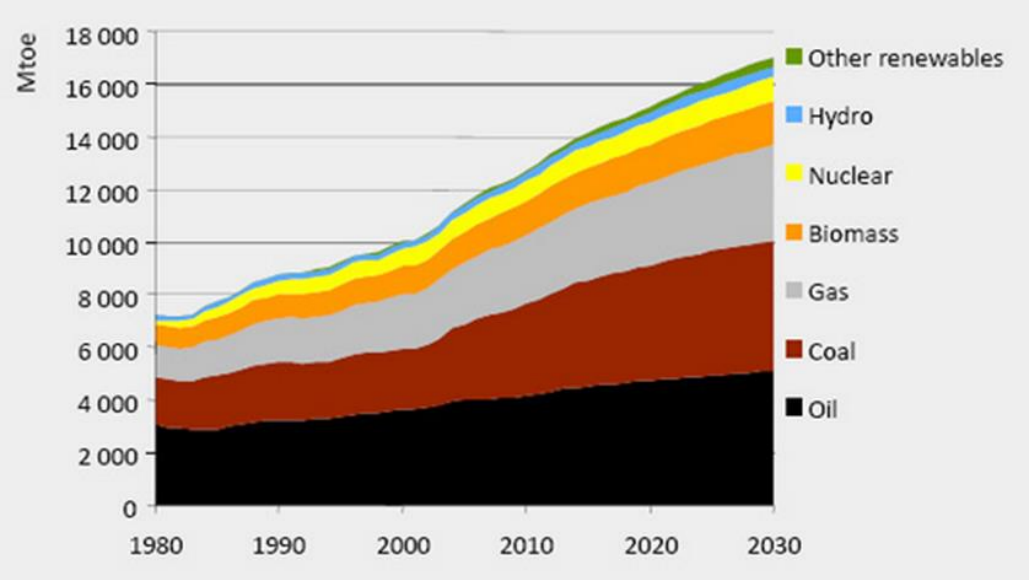

Figure 1: The development of fossil energy carrier consumption [3].

Commercially the energy is supplied by combustion of fossil fuels. These combustion processes up to now simply release the carbon containing gases into the atmosphere. The most common sources for these combustion processes are oil, coal and natural gas. One problem with those primary energy sources is that reserves are limited and it is very difficult to estimate how much can be exploited in the future [4]. Another aspect concerns the geographic distribution of nations owning deposits as producers and industrialized nations as consumers. Whenever there is an imbalance in political, economic or military interests prices tend to fluctuate in highly unpredictable ways. The notorious oil crises of 1973 and 1980, the continuing financial crisis of 2008, turmoil in oil exporting countries [5] and a heavy dependence of the European union on Russian gas are clearly reflected in the cost of fossil energy. The mentioned fluctuation is shown in the *Figure.2*.

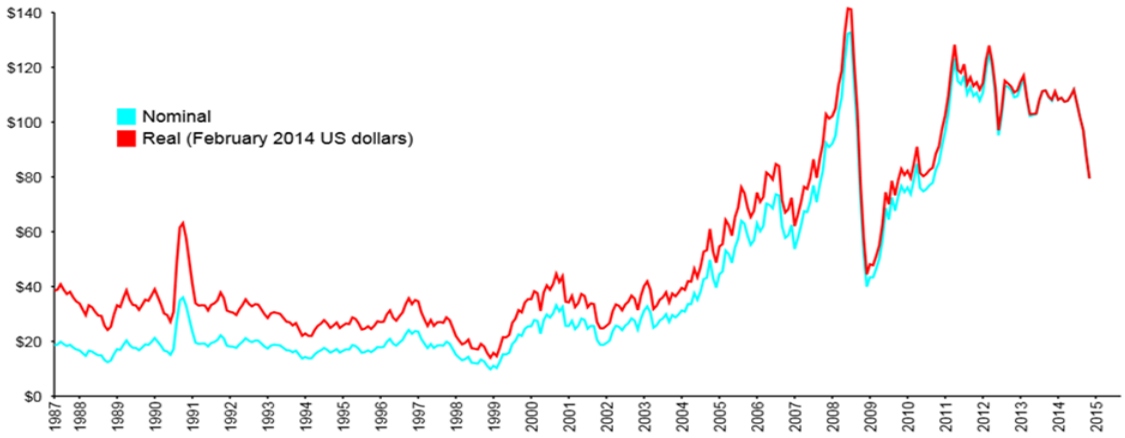

Figure 2: Fluctuation of the oil price since 1987 [6].

New renewable energy sources are in high demand. Nowadays there are a lot of technologies to produce sustainable energy, each one with its characteristic advantages and drawbacks. Some renewable and sustainable technologies are wind power, photovoltaic electricity generation, hydrodynamic power and biogenic energy sources e.g. biofuel and wood chip burning. One of the main drawbacks is that these energy sources are not constantly available like wind or sunlight to produce electricity. These dependencies make the use of storage methods necessary and expensive. Another drawback of biogenic energy sources is that they also produce carbon dioxide. However CO_2 produced from biogenic sources is considered to be 'CO_2-neutral' because the emitted carbon was consumed earlier during plant growth. But the effects of 'CO_2-neutral' carbon emissions for the environment are the same like all other. All these problems gave motivation to investigate hydrogen as a new energy carrier for the future.

1.2 Hydrogen and fuel cells

Hydrogen was found originally by Henry Cavendish in 1766 when he performed experiments with metals and acids. He recognized that a gas is formed and called it 'flammable air' because of its flammability. A more detailed analysis was conducted by Antoine Laurent de Lavoisier in 1787. He purged steam over glowing iron filings which were placed in a closed chamber and realized that less steam left the chamber than was fed into it. In addition a flammable gas was formed that during combustion reproduced the observed water vapour deficit. Lavoisier called this gas 'hydro-gène' because 'hydro' means water and 'gène' means producing [7].

Hydrogen is the smallest, diatomic, linear molecule. It has the lowest density compared to all other gases, is colorless, odorless and highly flammable. Hydrogen has the biggest energy density per mass compared to all other commercial fuels. Despite being the most abundant element in the universe it is present in the atmosphere only in traces. It is used in metallurgic, petrochemical and food chemistry. The two main processes using hydrogen at an industrial scale are the Haber-Bosch- and the Fischer-Tropsch-syntheses. The Haber-Bosch-synthesis

produces ammoniak, mainly used for fertilizers and explosive substances. The Fischer-Tropsch-synthesis produces hydrocarbons out of carbon monooxide and hydrogen. The hydrogen is bound in water and other, mostly organic, energy rich compounds. Energy must be expended to free the hydrogen which in effect reduces its usable energy content and puts it into the category of secondary energy sources. From the economic aspect a large scale centralized hydrogen production is most efficient but there are problems that have to be overcome. These problems mainly refere to storage and delivery. Hydrogen in pressure tanks has to be compressed resulting in loss of useful energy. If stored in liquid form it has to be cooled with corresponding loss of efficiency. A solution would be a decentralized production on demand but cost effectiveness and economic feasibility are favoured with size [8].

1.2.1 Fuel cell systems

Hydrogen can be used in two different ways to generate energy. It can be combusted like commercial fuels e.g. natural gas or it can be fed to a fuel cell system to produce electricity. A fuel cell system is shown in *Figure.3*. In both cases water and heat are the final products after the reaction so there are just negligbile effects on the environment. During commercial combustion the produced energy from the reaction is used to drive a piston or a turbine. The piston or turbine transfers the mechanical energy to an electric generator and finally electricity is produced. This process underlies the efficiency limitations of heat engines (Carnot efficiency) and has the drawback that the moving parts cause friction losses and generators have losses of their own. A fuel cell system has the benefit that it is using the chemical energy directly and no moving parts are involved. There are different kinds of fuel cell systems e.g. PEMFC; AFC, DFC, PAFC, MCFC and the SOFC [9]. The acronyms of the different fuel cell systems are explained in the appendix. They work in different temperature ranges and have specific requirements on the purity of the hydrogen. The PEMFC is working at a low temperature level of 80°C and requires very pure hydrogen (99,999 %) [10]. The need for very pure hydrogen opens a wide field in research for hydrogen production, storage and purification. The required purity values varies depending on the system. For LT-PEM-FC's (low temperature 80 °C) with platinum electrodes 10 ppm is the limit. [11], [12]. CO binds to the active sites of the catalyst and cause catalyst poisoning. Other FC systems are more tolerant against CO. In the case of a SOFC system which is working in a range between 650 – 1000°C CO contaminations do not harm the system [9].

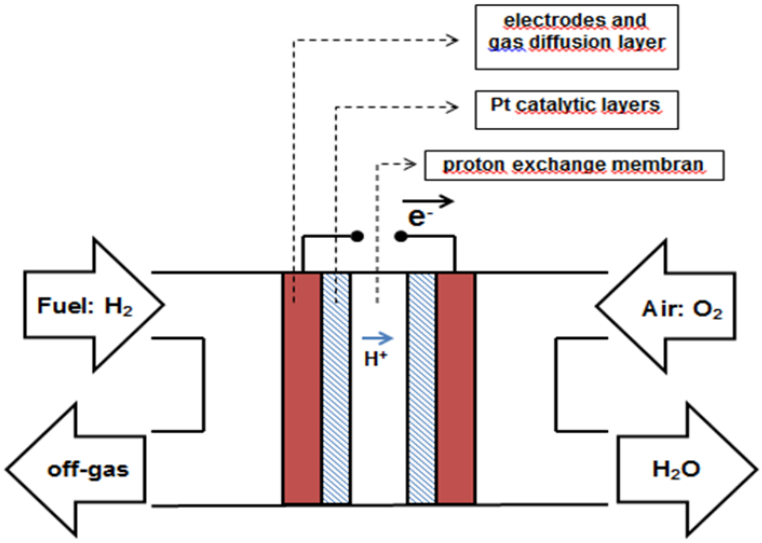

Figure 3: Schema of a PEMFC (proton exchange membrane fuel cell).

1.2.2 Hydrogen generation from hydrocarbons

Hydrogen can be produced from several fossil materials such as oil, natural gas or coal. The most common ways to produce hydrogen in an industrial setting are reforming processes.The ratios of hydrogen that are obtained from these sources are listed in *Table.1*. The amount of hydrogen that is produced per year world wide is around 50 Mt. This quantity is equal to 2 % of the world primary energy demand [13].

Table 1: Comparison of the amount of hydrogen produced from different fossil sources plus electrolysis [13].

Fossil source:	natural gas	liquid fuels	coal	electrolysis
Hydrogen / % :	55	32	10	3

Most of the reforming processes have the disadvantage that the hydrogen is not produced in pure form but mixed with carbonaceous byproducts and sometimes with sulfur- or nitrogen compounds. To obtain high grade hydrogen a cascade of reactors is needed which work at different temperatures and also perform different reactions. Even with the use of more reactors a final clean up is often necessary. The clean up process uses pressure swing adsorption processes or membrane diffusion processes which are highly expensive and lower the overall efficiency [14]. The reforming process needs a catalyst to be practical. The best working catalysts contain noble metals which are very expensive and rare. This created a field of research to find cheaper options and nowadays catalysts like nickel, copper and iron are used depending on the operation temperature and the reaction [15]. There are three primary techniques used to produce hydrogen from hydrocarbon fuels and these are explained below [16].

Steam reforming

Steam reforming *Equation.1* in combination with the water gas shift (WGS) *Equation.2* reaction is the most common way to produce hydrogen on an industrial scale. The reforming process is converting steam and methane into carbon monoxide and hydrogen. This process is working in a temperature range between 750 °C to 850 °C. The WGS reaction converts carbon monoxide and steam to carbon dioxide and hydrogen. Both reactions are reversible and lead to methane and carbon monoxide impurities in the final hydrogen stream [17]. A drawback is that even traces of carbon monoxide impurities are catalyst poisoning agents for catalysts both in the reforming reactor and in the later used fuel cell system.

$$CH_4 + H_2O \leftrightarrow CO + 3\ H_2 \quad (1)$$

$$CO + H_2O \leftrightarrow CO_2 + H_2 \quad (2)$$

The reforming reaction is endothermic, requires external heat and produces synthesis gas. The hot synthesis gas is used in a heat exchanger for steam generation. Also the heat of the flue gas of the burner in the reformer is used in the heat exchanger to produce steam. The burner uses the feed, the residual gas from the CO_2 removal and air to heat up the reformer. The combination with the water-gas-shift (WGS) reaction enables even more hydrogen to be produced and to lower the CO content. The WGS reaction is exothermic and is applied in the temperature range of 250 – 400 °C. The WGS reaction is performed in two different reaction zones with a high temperature WGS reactor and a low temperature WGS reactor to achieve optimal carbon monoxide conversion and to avoid carbon depostion [18]. The need for two water gas shift reactors is explained in two ways. During the high temperature WGS reaction the reaction is thermodynamically disfavoured but the kinetics are fast and the separate reaction room opens the opportunity to feed extra steam to the reaction and shift the equilibrium. During the low temperature WGS reaction the reaction kinetics are hinderd but the formation of CO_2 is thermodynamically more favoured. The single process steps are represented in *Figure.4*. The final clean up is done with a pressure swing adsorption (PSA) system. This system uses a tower that is filled with an adsorbens. This adsorbens can bind the impurities better than hydrogen and with additional pressure hydrogen is enriched in the gas phase. After releasing the pressure pure hydrogen leaves the system and afterwards the impurities are desorbed from the adsorbens. The main impurity is carbon dioxide that can be stored or used in another process.

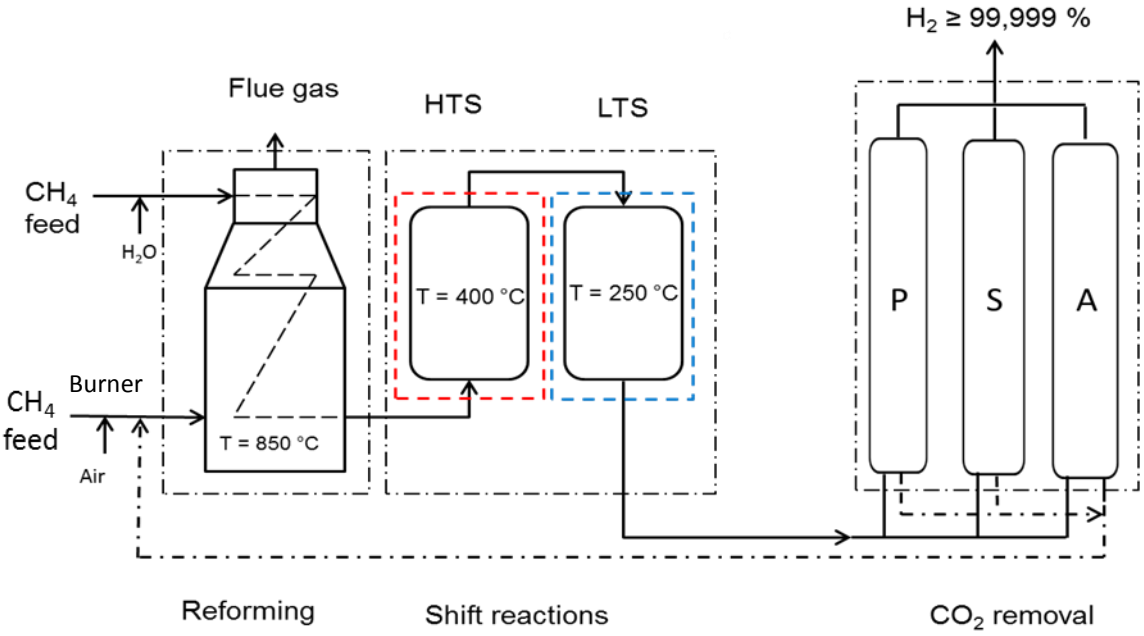

Figure 4: The flow sheet of the reforming (left), the water gas shift (middle) and the clean-up process (right).

Partial Oxidation

The partial oxidation requires oxygen to produce hydrogen out of hydrocarbons *Equation.3*. The oxygen that is fed to the reaction has to be in a substoichiometric ratio in respect to the hydrocarbons. Otherwise the products would be carbon dioxide and water. The oxygen normally is delivered from air that is used as an oxidant. It is normally performed at high temperatures > 1200 °C to ensure best conversion. The reaction temperature is controlled by a defined combustion in terms of oxygen delivery. A drawback of this process is that in most cases carbon formation does occur inside the reactor. An advantage of this process is that no catalyst poisoning occurrs and that carbonaceous or sulfur impurities do not harm the process to the same extent as they do in other systems. Another similar process is the catalytical partial oxidation where normally platin, rhodium, nickel or ruthenium catalysts are used [19]. The catalysts enable the process to run under lower temperatures and favour the thermodynamic equilibrium considering the products. The low reaction temperatures in the catalytical partial oxidation avoid the formation of degradation products of the fuel.

$$C_nH_m + n/2\ O_2 \rightarrow n\ CO + m/2\ H_2 \quad (3)$$

An example for the exothermic reaction enthalpies are shown in *Equation.4* and *5* .

$$CH_4 + ½\ O_2 \rightarrow CO + 2H_2 \qquad H_{R(298\ K)} = -36\ kJ{\cdot}mol^{-1} \quad (4)$$

$$CH_4 + O_2 \rightarrow CO_2 + 2H_2 \qquad H_{R(298\ K)} = -319\ kJ{\cdot}mol^{-1} \quad (5)$$

The catalytical process is energy saving because of the exothermic reactions that take place. The main drawback of this process is that the produced hydrogen is diluted with nitrogen if air is used as an oxidant. The noble catalysts are very expensive and do also lower the cost efficiency.

Autothermal reforming

This is an overall thermoneutral reforming method. Autothermal reforming adds steam to catalytic partial oxidation *Equation.6*. It consists of two reaction areas where the first one is called the thermal- and the second one the catalytical zone. In the thermal zone a partial oxidation or catalytical partial oxidation takes place.

$$C_nH_m + n/2\ H_2O + n/4\ O_2 \rightarrow n\ CO_2 + (m/2 + n/2)\ H_2 \quad (6)$$

This reaction is exothermic and transfers heat to the catalytic downstream steam reforming area. There the endothermal reforming reactions occur. As a result of this combination no external heat source is necessary [19]. Another advantage is that this systems can be started and stopped very fast and produces more hydrogen than the partial oxidation. A disadvantage of this process is that the fuel to oxygen as well as the carbon to steam ratios have to be controlled permanently to achieve the desired temperature and product gas composition.

1.2.3 Hydrogen generation from water

Electrolysis

Electrolysis needs electricty to split the H_2O molecule into oxygen and hydrogen. This method uses the electrochemical redox reaction for water decomposition. Water resists decomposition up to a voltage of 1,23 V relating to the standard hydrogen electrode [20]. Oxygen is generated at the anode and hydrogen at the cathode side of the electrolysis cell. The single reactions and the over all reaction are described by the *Equations.7,8* and *9*.

Anodic reaction: $2\ H_2O \leftrightarrow O_2 + 4\ H^+ + 4\ e^-$ $E_{An} = 1{,}23$ V (7)

Cathodic reaction: $4\ H^+ + 4\ e^- \leftrightarrow 2\ H_2$ $E_{Cat} = 0{,}0$ V (8)

Overall reaction: $2\ H_2O\ (l) \leftrightarrow$ electrolysis $\leftrightarrow 2\ H_2\ (g) + O_2\ (g)$ $E_{Overall} = 1.23$ V (9)

Electrolysis can be performed with a high efficiency depending on the system [22][23]. There are different kinds of electrolytic processes e.g. alkaline electrolysis and high temperature or high pressure electrolysis. The alkaline electrolysis is described by the *Equations.10,11* and *12* [21].

Anodic reaction: $4\ OH^- \leftrightarrow 2\ H_2O + 4\ e^- + O_2$ $E_{An} = 0,4$ V (10)

Cathodic reaction: $2\ H_2O + 2\ e^- \leftrightarrow 2\ OH^- + H_2$ $E_{Cat} = -0,83$ V (11)

Overall reaction: $4\ H_2O \leftrightarrow 2\ H_2 + O_2 + 2\ H_2O$ $E_{Overall} = 1,23$ V (12)

The pressure electrolyses has the benefit that a following compression for storage or transport is not necessary [22][23]. These systems have a very good performance but are only ecologically feasible if the energy that is used can be produced by sustainable processes like photovoltaic, water or wind power. Another aspect is that oxygen is also produced in great amounts. Oxygen demand in industry is limited and ways to use this ‘byproduct’ should be found [13].

Thermolysis

The thermolysis of water *Equation.13* is the thermal splitting of water at high temperatures above 2000°C.

$$H_2O + \text{heat} \leftrightarrow H_2 + ½\ O_2 \quad (13)$$

Because of the high temperatures and expensive separation processes it is not feasible for commercial hydrogen production. New investigations are focused on a process that utilize sunlight in combination with metals to split water. This process uses concentrator lenses to focus the sunlight and to transfer the heat to the metal surface. A common metal in this process is zinc and the reaction is shown in *Equation.14*.

$$Zn + H_2O + \text{heat} \leftrightarrow ZnO + H_2 \quad (14)$$

The advantage of the metal is that the process can be performed at lower temperatures. In the case of zinc the water splitting reaction takes place at about 600 °C [24]. This process is a potential alternative to other hydrogen production methods but further research is neccesary to prove its practicality.

1.3 Hydrogen generation from hydrocarbons and water by use of iron and iron oxides: The steam-iron-process

It is the aim of the steam-iron-process (SIP) to produce pure hydrogen from water in a reversible cyclic redox system. This reaction produces iron oxides and hydrogen in one reaction step (*Equations.15,16*) and in another reaction step the oxides are reduced (*Equation.17,18*) to start with the first step again. The iron species that occur during this process are metallic iron Fe, the first oxide specie the so called wustite FeO and the second oxide specie the magnetite Fe_3O_4. The third oxide specie the haematite Fe_2O_3 is not formed during this reaction because of thermodynamic limitations. The principal of the steam - iron process is known since the 18th century and consists of a tubular reactor, where iron is heated up to 600 - 800°C and water in form of steam is fed through. The iron is binding oxygen from the water creating iron oxide and hydrogen leaves the reactor. After the reaction has completed fresh metal was filled into the reactor and the oxide was recycled in the iron producing industry [25].

$Fe + H_2O \rightarrow FeO + H_2$	(oxidation)	(15)
$FeO + H_2O \rightarrow Fe_3O_4 + H_2$	(oxidation)	(16)
$Fe_xO_y + H_2/CO \leftrightarrow Fe + H_2O/CO_2$	(reduction)	(17)
$Fe_xO_y + C_mH_n \rightarrow x\ Fe + m\ CO + n/2\ H_2$	(reduction)	(18)

Hydrogen production on large scale was first performed by the so called Lane process which worked similar to the later developed Messerschmitt process to fill ballons and airships [26]. The Messerschmitt process was a discontinuously working single retort process were the iron oxide was regenerated to the metallic form by purging syngas ($CO+H_2$) into the reactor [27]. The Lane process was working in the same way as Messerschmitt's but used a multiple retorte system of reactors for better efficiency. With the use of multiple retorts it was possible to perform this reaction as a quasi continuous working process that is shown in *Figure.5*. The process is called quasi continuous because after the reduction has finished the gas supply has to be changed to perform the oxidation. The iron is always located in the same reactor but because of different reaction kinetic of the reduction and the oxidation more reactors are used to produce no idle time. The arrows between the reactors are indicating that the gas supply is changed and not that the iron is moving from one to another reactor.

1 Introduction

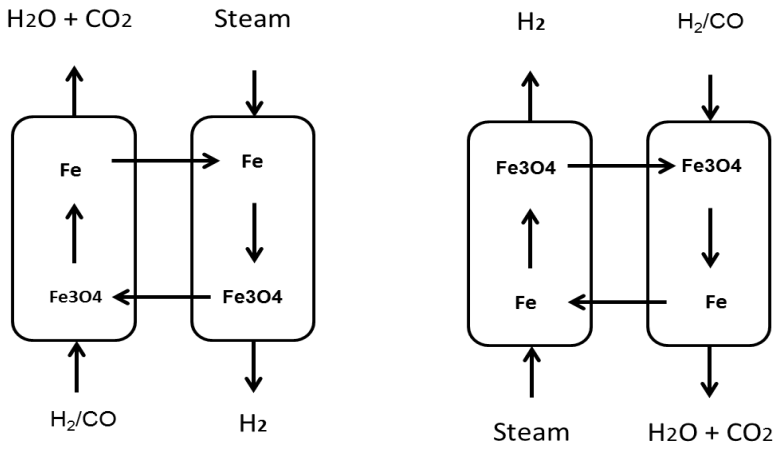

Figure 5: The principle of the quasi continuous working process. During reduction of magnetite in one reactor the oxidation of the iron with steam is performed at the same time in a second reactor (left). The opposite reactions occur after the gas supply switched from reducing gases to oxidizing gases (right).

A significant problem was that after some repeating redox cycles the contact mass deactivated due to sintering effects. The sintering caused a loss of reactive surface and the amount of hydrogen that was produced decreased over consecutive cycles. Messerschmitt improved his system by optimizing the venting system and the heat distribution of the reactor which had significant effect on the performance of the iron oxide contact mass. He was able to decrease the sintering effects and improved the lifetime of the iron oxide. Overall his system was more stable and economic. These types produced hydrogen of good quality but with some impurities. For applications like for the zeppelin those impurities did not harm the performance of the lifting gas. The combination of the iron oxidation and the oxide reduction is commonly called the steam - iron – process. In this work the more accurate description for this process is the sponge iron cycle. Iron and sponge iron are chemically identical and do only differ in their structure. Iron is a tight packed solid and the sponge iron has a porous structure. This porous structure is important to get a large surface for the desired reaction and to achive high efficiency. The sponge iron is also called direct reduced iron and is formed in the blast furnace by reducing gases like H_2 or CO in a temperature region where no melting occurs.

The SIP is part of the RESC that was developed at the Graz University of Technology by Viktor Hacker [28]. The RESC is the so called reformer sponge iron cycle and is the combination of a reformer and the steam-iron process. The reformer delivers the reducing gas to the SIP. The combination of both processes makes the entire system much more efficient. In *Figure.6* the whole process is outlined.

1 Introduction

RESC (reformer sponge iron cycle) :

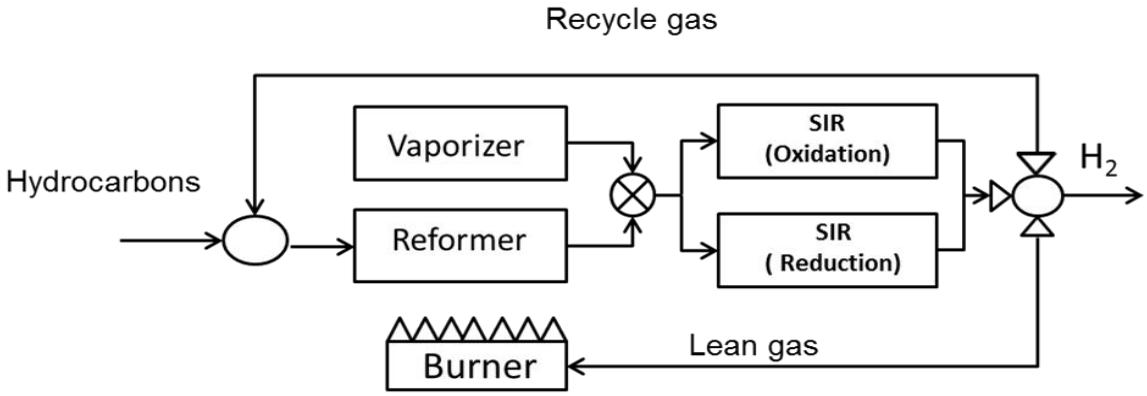

Figure 6: The schema of the RESC (reformer sponge iron cycle)[28].

The reformer is converting long hydrocarbons to shorter ones mostly methane and the methane is further reformed to syngas [28]. The off-gas at the reformer outlet is composed of methane, cabonmonoxide and hydrogen. This reducing gas composition is used to reduce the iron oxides in the SIP. The product gas after this reduction in the SIP is a mixture of carbon dioxide, carbon monoxide and steam. This mixture is used to feed the burner and to be recycled in the reformer to get best hydrocarbon conversion. With a vaporizer and a second SIP reactor it is possible to run the process continuously. As the one SIP reactor is performing the reduction with the reformer offgas the second one is producing hydrogen while becoming oxidized with steam. After this step has finished the gas supplies are changed and the same reactions as before occurs but just in the opposite reactor. All the occurring reactions are listed in *Table.2*.

Reactions in the Reformer: **Reactions in the SIP:**

Table 2: Reactions that occur in the reformer (left) and the reactions that occur in the SIP (right)

Reformer		SIP		
Reduction :		**Reduction:**		**Oxidation:**
$C_7H_{16} + 3\ CO_2 \rightarrow 4\ CH_4 + 6\ CO$		$Fe_3O_4 + H_2 \rightarrow 3\ FeO + H_2O$		$Fe + H_2O \rightarrow FeO + H_2$
$C_7H_{16} + 3\ H_2O \rightarrow 4\ CH_4 + 3\ CO + 3\ H_2$		$Fe_3O_4 + CO \rightarrow 3\ FeO + CO_2$		$3\ FeO + H_2O \rightarrow Fe_3O_4 + H_2$
				Hydrogen Output
$CH_4 + CO_2 \rightarrow 2\ CO + 2\ H_2$		$FeO + H_2 \rightarrow Fe + H_2O$		$\mathbf{3\ FeO + H_2O \rightarrow Fe_3O_4 + H_2}$
$CH_4 + H_2O \rightarrow CO + 3\ H_2$		$FeO + CO \rightarrow Fe + CO_2$		$\mathbf{3\ Fe + 4\ H_2O \rightarrow Fe_3O_4 + 4\ H_2}$
$CO_2 + H_2 \rightarrow CO + H_2O$		$CO_2 + H_2 \rightarrow CO + H_2O$		

1 Introduction

The SIP was already investigated at this institute [29]. The researchers used commercially available iron ore pellets instead of sponge iron as it is considered in this work. They found that it was possible to conduct 20 redox cycles without noticable decrease of hydrogen production. The redox cycles were performed between magnetite and wustite. The best working contact mass was the ore with the biggest gangue content.

The mentioned drawback of the steam iron process is the long term stability behaviour of the iron contact mass due to cycling stress exposure [29][30]. Most common problems occur because of carbon formation on the surface and through sintering effects of the iron grains. The process was investigated by reducing the contact mass with hydrogen to avoid coke formation completely. Hydrogen also shows the fastest reduction kinetics and was therefore used to investigate the stability behaviour of the contact mass. Best results were obtained with a mixture of 90 % haematite and 10 % aluminium oxide at 800 °C. This sample showed a decrease in the oxygen exchange capacity of just **5 % over 500 cycles** [31]. The different oxide states of iron as well as the metallic form are well know. Although a lot of investigation has been performed on the reduction and the oxidation of iron the entire reaction is not completely understood. The origin of the complexity of this reaction is that many factors influence the stability of the contact mass. To determine the kinetics and the mechanism of these processes some interdisciplinary collaborations are necessary. From the point of heterogenic catalysis there are seven general processes that occur in gas solid reactions.

- Diffusion through the gas-solid interface (film diffusion)
- Diffusion of the molecule into the pores (pore diffusion)
- Adsorption of the molecule on the catalytically active site
- Chemical reaction with other molecules on catalyst surface
- Desorption of products from surface
- Diffusion of product out of pores (pore diffusion)
- Release of the product through solid gas interface (film diffusion)

In the case of steam-iron-process it is more complicated because iron in the contact mass is clearly not behaving like a catalyst. A catalyst is defined as a chemical promotor which decreases the activation energy, fasten up the reaction but is not consumed during reaction and does not shift the equilibrium. During the SIP iron and its oxides continously undergo structural, electrical and chemical changes. So it interacts with the gaseous reactants as a reaction partner. The different oxide layers that are formed during oxidation have different cell parameters and therefore the contact mass alternatingly undergoes expansion and contraction. The growth of these layers is not linear over all these oxide states and so the kinetic order changes. If the SIP is performed only between magnetite and wustite Bohn et al. found that no stabilizing support is necessary [30]. In the focus of this work the reversible redox reaction between magnetite and iron is investigated because the hydrogen output is four times better and is illustrated in *Table.2*. The mentioned drawback is that the

grains of the contact mass start to sinter even after the first redox cycle if the reduction is done till iron. Due to that the production of hydrogen tends to deteriorate. Previous work showed that there are stabilizing metal oxides that can prevent the sintering of the iron particles. Some additives like alkali and earth alkali compounds can fasten up the reaction but have less stabilizing effect than others e.g. oxides of Al, Ca and Si. Those additives are called **chemical promotors**. Other metal oxides can stabilize the structure during the redox reaction but slower the reaction kinetics e.g. Al_2O_3. These additives are called **physical promotors**. There are several ways to make the contact mass. The simplest way is to mix the dry oxide powders in the desired proportions and form pellets. After a calcination step the pellets are used in the SIP. Another method is the wet-impregnation of the metals with a metal salt solution of the additive [31]. Other methods are the dry impregnation with the metal salt solution [29], the sol-gel method [28]., and the copreciptitation [32,34]. The addition of stabilizing additives has different effects. A positive effect is the improvement of stability over consecutive redox cycles, a negative effect is the reduction of the amount of reactive metal inside the reactor [30].

One of these stabilizing metal oxides is aluminium oxide. The behaviour of the various oxide phases as well as the function of the support additive will be explained in the next chapter. The specific informations about the oxides and the other starting materials are summarized at the end of the next chapter.

2 Properties and Characteristics of the starting materials

In this chapter the properties of the starting materials are discussed. For the electrical and magnetic transitions that occur some notations are used which are described in the *Table.3*.

Table 3: Summary and description of the different magnetic and electric phase transfers.

Name of transition	Acronym	Description
Curie temperature	T_C	valid for ferromagnetic materials: above this temperature the material loses its ferromagnetic properties and becomes paramagnetic
Néel temperature	T_N	valid for antiferromagnetic materials: above this temperature the material loses its antiferromagnetic properties and becomes paramagnetic
Morin temperature	T_M	only known for haematite: below T_M the spins of the iron layers align perpendicular to the c – axes and above they align parallel with a slight kink resulting in a weak net magnetic moment
Verwey temperature	T_V	valid for electrical conductors: above this temperature the material is a conductor and below it is an isolator

Haematite: α-Fe_2O_3

Under standard conditions haematite $Fe^{+3}{}_2O^{-2}{}_3$ is the most stable iron oxide species. It has a trigonal crystal system and a rhombohedral crystal structure. The cell constants are: a = 5.03 Å and c = 13.73 Å. The unit cell is built up of 6 formula units [35]. Haematite is a red ore with a density of approx. 5.2 $g \cdot cm^{-3}$ and a Mohs hardness of 5 – 6 [35]. The melting point of haematite is 1565 °C [36]. Depending on temperature, three different magnetic phases are known. Below Morin-temperature (-13.15 °C) haematite exists in its antiferromagnetic form, above it shows a weak ferromagnetic behaviour [37]. In the antiferromagnetic form the single spins of the atoms sum up to zero and no magnetic behaviour is observed. Because of the distorted structure of the rhombohedral elementary cell the iron ions cannot interact efficiently and the resulting ferromagnetism is much weaker than in other structures e.g maghemit γ-Fe_2O_3 with a spinel structure and strong ferromagnetic properties. At the Curie-temperature of 675 °C, a second phase change occurs and the ferromagnetic behaviour changes to paramagnetic [38]. This effect is caused by the thermal energy which disorders the spins of the iron ions. All the iron ions are in the +3 charge state and all the oxygen ions in the -2 charge state. The oxygen ions are in the noble gas configuration and do not participate in the magnetic behaviour. At room temperature it acts as an isolator but becomes a semiconductor at high temperatures [39].

This structure is also called the corundum structure where the oxygen ions build up a hexagonal closest packed structure. The iron ions are placed in 2/3 of the octahedral gaps. In the *Figure.7*, *8 and 9* the hexagonal structure of the oxygen ions and the octahedral as well as the tetrahedral gaps are shown.

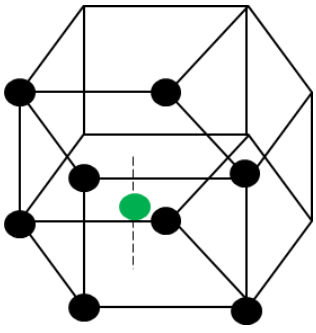

Figure 7: The unit cell of a hexagonal / trigonal crystal system [40]. The whole object shows the hexagonal unit cell and black dots are representing the trigonal unit cell.

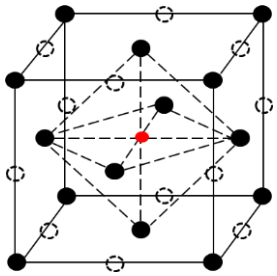

Figure 8: The crystal structure of a cubic face centered crystal structure. Black dots are representing the oxygen ions in the crystal. The empty doted circles are the octahedral vacancy sites. The red dot shows a metal ion that occupies a octahedral vacancy site [41].

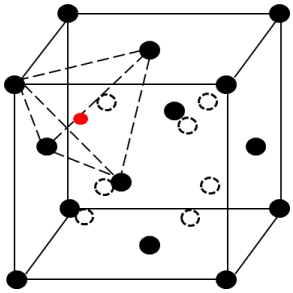

Figure 9: The cubic face centered structure with all possible tetrahedral vacancy sites. The red dot is a metal ion occupying a tetrahedral vacancy site [41].

Magnetite: Fe_3O_4

Magnetite $Fe^{+2}(Fe^{3+})_2O^{-2}{}_4$ is a black oxide with mixed valences. It crystallizes in a cubic crystal system and an inverse spinel structure. The cell constant is a = 8.39 Å and the unit cell contains 8 magnetite molecules. Magnetite has similar physical properties like haematite with respect to the density 5.2 $g \cdot m^3$ [42]. The hardness is 6 and the melting point is 1535 °C [43]. Depending on the temperature it behaves as an isolator below the Verwey-temperature of -153 °C and changes to a bad conductor above this temperature. Up to the Curie temperature of 576 °C it is ferromagnetic and changes to paramagnetic above this temperature [38]. The ferromagnetic behaviour is a result of a super interaction between the iron ions above the oxygen orbitals.

The Fe^{+3} ions have the electron configuration $3d^5$ and the Fe^{+2} ions have the configuration $3d^6$. The d-orbitals can contain 10 electrons but are only half filled. So a good electronic conductivity is expected. At room temperature it acts like a semiconductor with a band gap of 0.1 eV but the conductivity is much weaker than expected [44]. A simplified explanation for this behaviour is that the electrons interact with each other thereby minimizing their energy. Because of the Coulomb repulsion the electrons are located in positions with maximum distance and decrease the conductivity. According to the Pauli principle only 5 of the 10 electrons in the d-orbitals are allowed to have the same spin. And according to Hund's rule of maximum multiplicity the electric situation after an electron transfer from a Fe^{+2} ion to a Fe^{+3} ion the valences and the spins of the ions have to be the same as before. There are some possible transfer processes but in the case of magnetite only one is following Hund's rule and this is the transition that is shown in *Figure.10* [45].

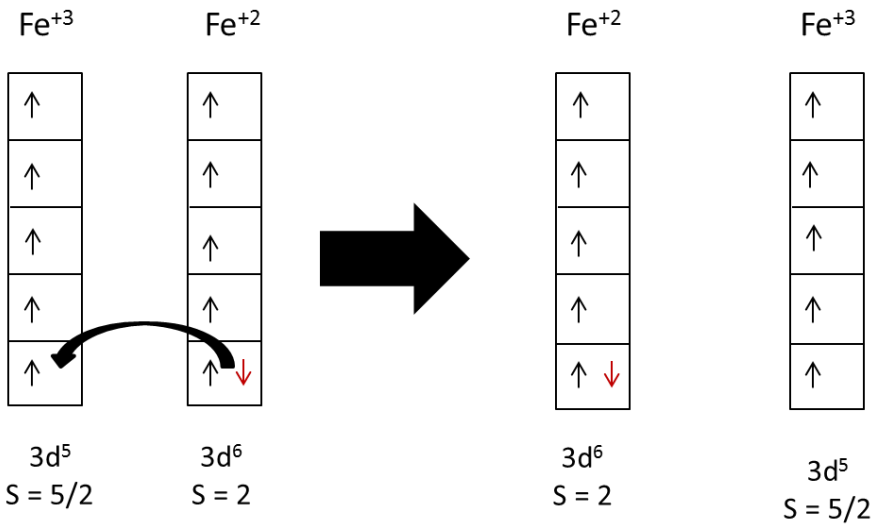

Figure 10: The only allowed electron transfer mechanism according to Pauli's law and the Hund's rule.

The spinel structure is formally built up of $A[B_2]O_4$ units where A ions are the A^{+2} ions and B ions are the B^{+3} ions. In this structure the O^{-2} anions are building up a tight cubic face centred lattice. The tetrahedral gaps are occupied by the A^{+2} iron ions by 1/8 of the possible gaps. The octahedral gaps are occupied by the B^{+3} iron ions by ½.

In the inverse spinel the formula unit is B $[AB]O_4$ and ¼ of the octahedral gaps are occupied by the A^{+2} ions. The B^{+3} ions are located in ¼ of the octahedral gaps and 1/8 in the tetrahedral sites.

Wustite: FeO

The wustite $Fe^{+2}O^{-2}$ crystallizes in a cubic crystal system in a deficit NaCl-structure with a lattice constant of a = 4.18 Å. One unit cell is built up of 4 formula units. Wustite has a density about 5.99 $g \cdot cm^{-3}$ depending on the impurities and the number of iron vacancies in the lattice [46]. The Mohs hardness was determined to 5.5 and it has a melting point of 1369 °C [47],[48]. It can be considered as two staggered cubic face centered lattices which are built up of the oxygen and the iron ions. The deficit in the NaCl structure is expressed by the modified sum formula $Fe_{1-x}O$ where 1-x can have values between 0.83 – 0.95 [49]. This non stoichiometry is caused by iron vacancies in the lattice. To fulfill the electro neutrality some Fe^{+2} ions are replaced by Fe^{+3} ions.

It is antiferromagnetic below the Neel-temperature at – 75 °C and strongly paramagnetic above this temperature. Wustite is only stable above 560 °C and below this temperature it tends to dissociate into iron and magnetite [50]. This behaviour is expressed with the equilibrium equation below.

$$4\ FeO \leftrightarrow Fe_3O_4 + Fe \qquad (19)$$

In this structure the iron ions are mostly located in the octahedral gaps and some are located in the tetrahedral gaps. In contrast to the inverse spinel the octahedral gaps are occupied only by ions with the same oxidation state +2. Equilibrium occurs between magnetite and wustite above 560 °C and can be expressed with *Equation.20* [50]:

$$2\ Fe(^{+2})Fe(^{+3})_2O_4 \leftrightarrow 6\ FeO + O_2 \qquad (20)$$

Researchers found out that the percentage of the lattice vacancies is strongly dependent on temperature and oxygen partial pressure and can vary from 5 % between the Fe/FeO interface to 15 % at the FeO/Fe_3O_4 interface at 1000 °C [51].

Wustite is a semiconductor with a band gap of 1.83 eV. Magnetite in contrast has a band gap about 0.1 eV and haematite has a band gap of 2.2 eV [52].

To illustrate the magnitude of disorder that is caused by the replacement of an iron Fe^{+2} ion with an iron Fe^{+3} ion a theoretical ideal wustite unit cell is shown in *Figure.11*. It is known that wustite has an iron deficit that is balanced by the insertion of an iron Fe^{+3} ion. In *Figure.11* a Fe^{+3} ion is placed on a tetrahedral site and the Fe^{+2} ions are removed to get electric neutrality.

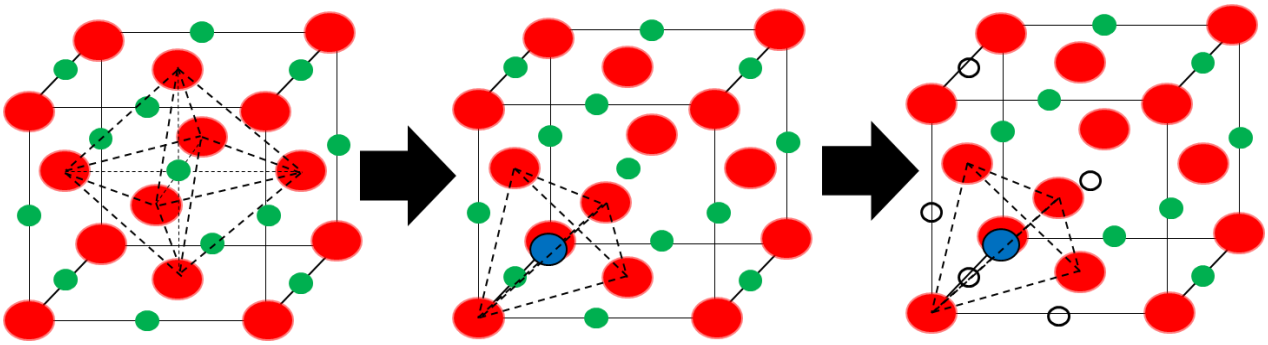

Figure 11: A perfect NaCl- structure (left), NaCl- structure with a Fe^{+3} ion (blue) occupying a tetrahedral side (middle), theoretical situation in an ideal wustite without the Fe^{+2} (green) ions to get electric neutrality (right).

Iron: Fe

Beside cobalt and nickel, iron is the third of the three existing ferromagnetic metals. Iron crystalizes in a cubic crystal system. Under ambient conditions up to 911 °C it appears in a cubic room centered structure with two iron atoms in its unit cell. This iron structure has a cell constant of a = 2.86 Å and is called α-iron or ferrite [53]. The Curie temperature is 760 °C where it changes its behaviour from ferromagnetic to paramagnetic [37].

Between 911 °C and 1392 °C the structure changes to a cubic face centered modification with a cell constant of a = 3.43 Å. This structure of iron is called γ-iron or austenite. The unit cell is built up of four iron atoms. Above 1392 °C the structure changes again into a cubic room centered unit cell [54]. This type of iron is called δ-

iron. All the different cell structures and the according temperature ranges are illustrated in *Figure.12*. The melting point of iron is 1538 °C [55]. The Mohs hardness is about 4 – 5 and the density is 7.87 $g \cdot cm^{-3}$. The electron configuration of metallic iron is $3d^6 4s^2$. As expected for a metal it is a conductor. Its conductivity is $1 \cdot 10^7$ $A\ V^{-1} \cdot m^{-1}$ and electronegativity is 1.83 according to the Pauling-scale. The normal potential is 0.44 V based on the normal hydrogen electrode.

Iron readily reacts with acids like diluted hydrochloric acid, sulfuric acid and nitric acid producing hydrogen and the corresponding salt. Iron is produced by indirect reduction of iron ores with coal and melts in the blast furnace. The iron produced by this process is tightly packed and has no pores.

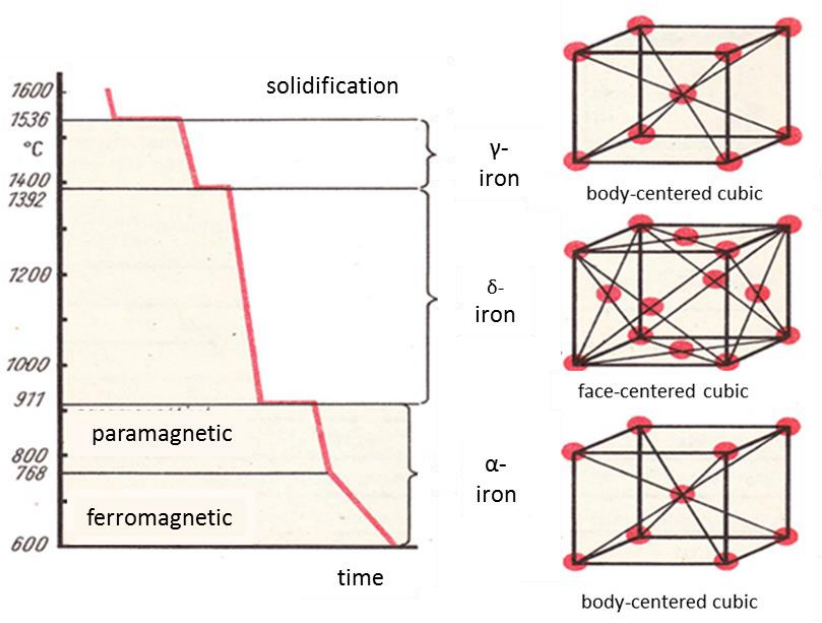

Figure 12: The iron cell structure changes depending on the temperature: bcc → fcc → bcc

Sponge iron:

Sponge iron *Figure.13* is produced by direct reduction of iron ores with hydrogen, carbon monoxide or methane. The iron sponge does not melt during it is produced and has a sponge like structure with many pores. The direct reduction enables the process to run at lower temperatures and the porous structure makes it more interesting for solid-gas reactions. The iron content of common sponge iron is between 93 – 97 % and the remaining percent consist of oxides and impurities [56].

2 Properties and Characteristics of iron, iron oxides and aluminium oxide

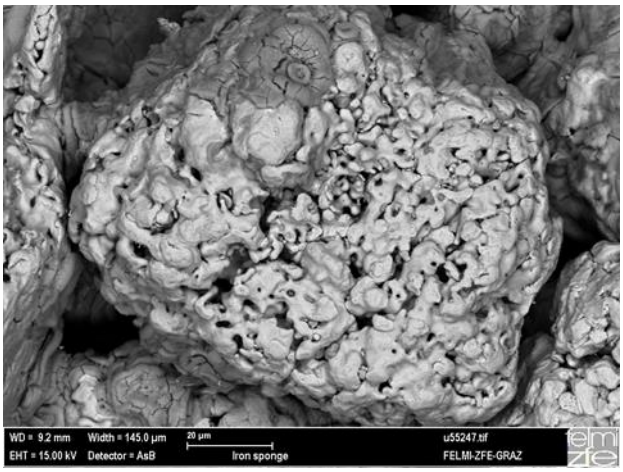

Figure 13: The porous structure of a sponge iron pellet with high surface [FELMI-ZFE-Graz].

Aluminiumnitrate (nonahydrat): $Al(NO_3)_3 \cdot 9\,H_2O$

The aluminium nitrate is considered here because it was used to impregnate the sponge iron and has some extraordinary properties. It has a molecular weight of 375.13 $g \cdot mol^{-1}$ and appears as colorless crystals. It has a density of 2.36 $g \cdot cm^{-3}$.

At 73 °C the crystal water is released and the aluminium nitrate dissolves. It degrades at 135 °C to nitric acid/ HNO_3 and alkaline aluminates / $Al(OH)_x(NO_3)_y$. Above this temperature nitric gases / NOx leave the liquid.

When dissolved in water it acts like an acid with a pH of 3. This acidic behaviour makes it feasible for impregnation because it is known that acids attack the surface of metals and enlarge them. It has a high solubility of 419 g / l in water [57],[58].

Aluminium: Al

Aluminium crystallizes in a cubic face centred structure with a cell parameter of a = 4.04 Å. Aluminium is paramagnetic, has a density of 2.7 $g \cdot cm^{-3}$ and a Mohs hardness of 2.7 [59]. The melting point is 660 °C. It is very ignoble but forms a protective layer of oxide in aqueous solutions and in contact with air that effectively stalls further corrosion. The oxide layer is stable in a pH range from 4 to 9 [60].

The electron configuration is much simpler than that of the iron and is $3s^2 3p^1$. So aluminium only has s and p valences. The most common oxidation state is +3 but it can also have the states +2 and +1. The electronegativity according to the Pauling scale is 1,61 and the normal potential is – 1.67 V. Comparing this normal potential with the one of iron +0.41 V it can be seen, that in the presence of iron oxide the aluminium will reduce the oxide to its metallic form and will be oxidized. This reaction *Equation.21* is well known and is called the thermite reaction.

$$2\,Al + Fe_2O_3 \rightarrow Al_2O_3 + 2\,Fe \qquad (21)$$

Aluminium Oxide Al_2O_3 [corundum]:

Aluminium oxide $Al^{+3}{}_2O^{-2}{}_3$ has a trigonal crystal system and a rhombohedral structure. Aluminium oxide belongs to the hexagonal crystal class and the structure is known as the corundum structure. The trigonal, rhombohedral structure is similar to the one of haematite. Aluminium oxide is normally produced by heat treatment of aluminium hydroxide or aluminium oxohydroxides. The thermodynamically most stable aluminium oxide is the α-modification. There are several other modifications but after thermal treatment at high temperature the final form is always α-aluminium oxide. Another interesting modification is the γ- aluminium oxide because it is known to develop a very large surface of up to 100 $m^2 \cdot g^{-1}$ but it is only stable up to 700 °C. This modification has a cubic crystal system and a defect spinel structure so it is very similar to the structure of wustite and magnetite.

The corundum structure is built up of repeating A-B layers of hexagonal tight packed oxygen ions. Between every second layer there is an aluminium layer called C layer where every third octahedral vacancy is unoccupied. The α-aluminium oxide has a Mohs hardness of 9 and a density of 3.94 $g \cdot cm^{-3}$. The lattice parameters are a =b = 4.75 Å and c = is 12.99 Å. Corundum is an isolator and mechanically very stable at high temperature. The melting point is determined to be 2072 °C [61].

The isolation behaviour can be explained easily by the electron configuration of the oxide. Metallic aluminium has an electron configuration of $3s^2 3p^1$ and in the oxidized state $2s^2 2p^6$. So all the orbitals are filled and no free electrons are available. In the case of oxygen the neutral molecular electron structure is $2s^2 2p^4$ and in the reduced state $2s^2 2p^6$ so here the orbitals are also completely filled and no free electrons are available.

Hercynite $FeOAl_2O_3$:

Hercynite $Fe^{+2}O^{-2}Al^{+3}{}_2O^{-2}{}_3$ is no starting material for the experiments in this work but it is formed during the reaction and therefore it is considered here. The chemical formula of hercynite is $FeAl_2O_4$ and it also has a cubic spinel structure like magnetite and wustite. It is formed if the concentration of Al_2O_3 exceeds the possible solubility in the wustite matrix. The solubility of Al_2O_3 differs for every oxide. Hercynite has a cubic crystal system and a spinel structure. The cell parameters are a=b=c= 8.13 Å and the unit cell consists of 8 formula units. The density is in the range of 4.25 – 4.32 $g \cdot cm^{-3}$ and the Mohs hardness is in a range of 7.5 – 8. The melting point of hercynite is 1780 °C and is higher than all involved iron species [62]. In the normal spinel the oxygen ions are arranged in a face centered cubic close packed lattice and the cations are distributed along the octahedral and tetrahedral sites. The Al^{+3} ions prefer to occupy one half of the octahedral interstitial sites and the Fe^{+2} ions are located on one eighth of the tetrahedral sites. At high temperatures the cation distribution changes to an inverse spinel structure where the Fe^{+2} ions occupy one fourth of the octahedral sites.

The conductivity is only slightly temperature dependent and the charge transfer is explained by an electron-transfer model between the Fe^{+2} and Fe^{+3} ions on the octahedral sites. So it is assumed that the conductivity is proportional to the concentration of the involved iron ion species and the temperature. A comparison of the conductivity of hercynite, hercynite mix with magnetite / 80:20 and pure magnetite is shown over a temperature range in the appendix. Also the miscibility of magnetite and hercynite is represented in the appendix. A summary of the crystal properties is given in *Table*.4 and the physical properties are listed in *Table.5*. In *Table.4* it can be seen that all participating species have a kind of spinel structure with the exception of metallic iron. This is interesting because it is known that a uniform solid solution can just exist if the crystal systems of the different compounds are similar. Other important relationships are the melting points of the materials which are listed in *Table.5*. There it is pointed out that all compounds have very high melting points except aluminium. This is very important for the application in the steam-iron-process because if melting would occur the contact mass would not be feasible in this process.

Table 4: Comparison of the crystal properties of the solid starting materials

species	Crystal system	Crystal structure	Cell Parameter / Å	Formula units / Unit Cell	Cell Volume / $Å^3$
Fe_2O_3	trigonal	rhombohedral	a=b=5,03 c=13.77	6	302.72
Fe_3O_4	cubic	Inverse spinel	a=b=c= 8.39	8	591.46
FeO	cubic	Inverse spinel (deficit NaCl structure)	a=b=c= 4.34	4	81.80
Fe (RT,1 atm)	cubic	bcc	a=b=c= 2.86	2	23.55
Fe (900°C, 1 atm)	cubic	fcc	a=b=c=3.64	4	48.50
Al	cubic	fcc	a=b=c=4.04	4	66.89
Al_2O_3	trigonal	rhombohedral	a=b=4.76 c=12.99	6	254.98
FeOAl2O3	cubic	spinel	a=b=c=8.155	8	542.50

Table 5: comparison of physical properties of the staring materials

species	Melting point / °C	Density / $g \cdot cm^{-3}$	Mohs hardness	Electric property @ RT
Fe_2O_3	1565	5.2	6	insulator
Fe_3O_4	1535	5.2	6	weak conductor
FeO	1369	5.9	5	semi-conductor
Fe	1535	7.87	4	conductor
Al	660	2.7	2,75	conductor
Al_2O_3	2050	3.95	9	insulator
$FeOAl_2O_3$	1780	4.3	7.75	insulator

2.1 Reaction mechanisms

In this chapter the notation introduced by Kröger and Vink is used to describe the chemical solid state reactions. The principle of this notation is that in a crystal structure the ions have a charge according to their element. In this notation the charge difference to the ideal lattice site is considered. In general a cation or anion can be written as M^{C}_{S} were M describes the element, S is the site that is occupied by the element and C denotes the electrical charge relative to the normally located ion. The superscript C can have different symbols where every symbol represents the formal charge of the species. Instead of C the charge is written as x according to neutral charge, ● is a single positive charge and ‘ denotes a single negative charge. These charges are related to the normal position of an ion in the lattice. So if an O^{-2} ion is located on its regular site it has the notation O^{x}_{O}. The subscript S can also have the denotation i that indicates an interstitial site. An interstitial site is located between two normal sites and can be used to illustrate that an ion is located on a vacancy site e.g. octahedral or tetrahedral vacancy site. There are three main rules that have to be maintained to use the notation in its right form. The whole lattice object has to stay in electric neutrality, the entire mass of the participating atoms/ions has to stay constant and the number of cation sites in a composition K_xA_y has to be in the right ratio to the anion sites. In *Table.6* and *7* the single acronyms that are used in this chapter are described. In *Table.7* additional symbols are described but are not used in this chapter.

Table 6: The symbols and descriptions that are used in this chapter in the Kröger-Vink notation

species / ions	description
O^{x}_{O} ; Fe^{x}_{Fe}	oxygen on an oxygen site with neutral charge; iron on an iron site with neutral charge
$V^{\bullet\bullet}_{O}$; V''_{Fe}	oxygen vacancy site with an effective charge of +2; iron vacancy site with an effective charge of -2
e^{-} ; $h^{\bullet}$	electron with -1 charge and a hole with +1 charge

Table 7: Additional symbols in the Kröger-Vink notation which are not used in this chapter

$K^{\bullet}_{I}$; A'_{i}	cation on interstitial site with +1 charge; anion on interstitial site with -1 charge
$Ca^{\bullet}_{Na}$; Br^{x}_{Cl}	A substitute Ca-ion on a Na-site with effective charge +1; A substitute Br-ion on a Cl-site with neutral charge.

2.1.1 Reduction mechanism of iron oxides in hydrogen atmosphere

The reduction of iron oxides has been investigated by many researchers [63–69] with the purpose to get information about the reduction mechanisms and the kinetics of the iron oxide reduction. To predict and simulate the behaviour of iron oxides in a reducing atmosphere mathematical model equations were developed. A significant problem of these model equations is that they normally just fit one mechanism and in case of iron oxide reduction the reaction mechanism is shifting from transport to diffusion control with consecutive reaction. Some researchers already found kinetic equations that can describe the reduction kinetic but if any parameters of the experimental setup are changed the equation is no longer valid [63-68].

The oxide species that are involved in the reduction reaction of iron oxide can be seen in the Baur-Glaessner diagram in *Figure.14*.

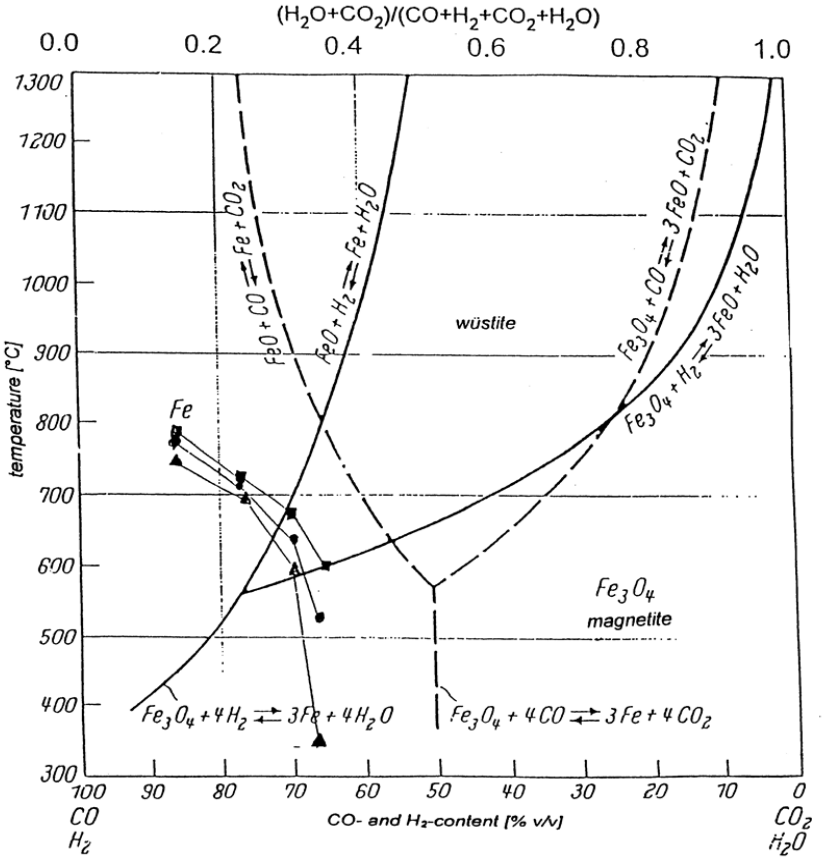

Figure 14: The equilibrium states of the iron oxide species in H_2/H_2O (straight line) and in CO/CO2 (dotted line) atmosphere [71].

2 Reaction mechanisms

An iron – oxygen equilibrium diagram is presented in the appendix for a more detailed view of the Baur-Glaessner diagram. The Baur-Glaessner diagram in combination with the Ellingham-Richardson diagram can be used to estimate if additives act as an oxidizing or reducing agent for the iron oxides. The Richardson diagram shows in addition the standard free energies of metal oxides as function of the temperature and the gas composition (see appendix).

The reactions during the reduction can be summarized as:

$$3\ Fe_2O_3 + H_2 \leftrightarrow 2\ Fe_3O_4 + H_2O \quad (22)$$

$$2\ Fe_3O_4 + 2\ H_2 \leftrightarrow 6\ FeO + 2\ H_2O \quad (23)$$

$$6\ FeO + 6\ H_2 \leftrightarrow 6\ Fe + 6\ H_2O \quad (24)$$

This three step mechanism is valid above 570 °C because the wustite phase is only stable above this temperature. The reaction kinetics below this temperature consists of a two-step reduction mechanism and is described by *Equation.25 and 26*:

$$3\ Fe_2O_3 + H_2 \leftrightarrow 2\ Fe_3O_4 + H_2O \quad (25)$$

$$2\ Fe_3O_4 + 8\ H_2 \leftrightarrow 6\ Fe + 8\ H_2O \quad (26)$$

The reaction is surface controlled at the very beginning of the reduction. This behaviour changes to a diffusion controlled mechanism after a specific time of reaction. The single process steps are shown in *Figure.15*.

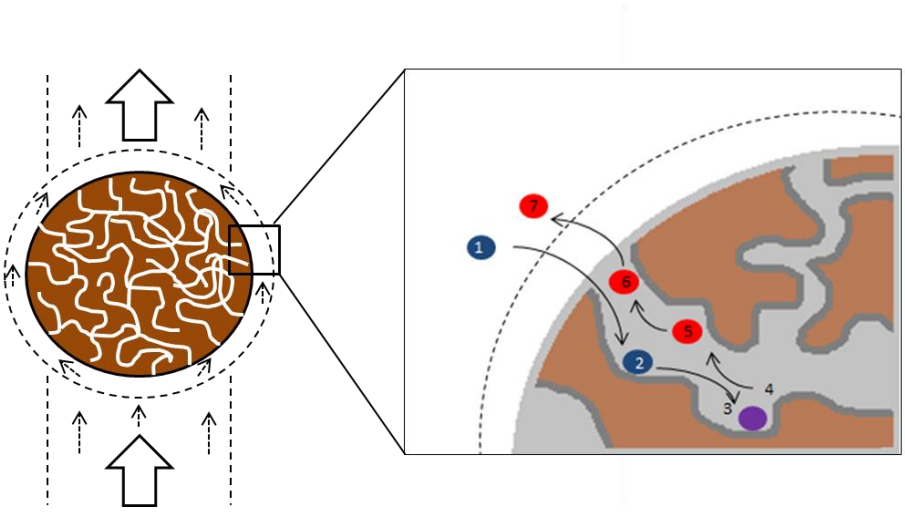

Figure 15: The gas flow surrounding a particle (left) and the building up of the gas/solid interface (right).

2 Reaction mechanisms

Figure.15 shows the mass transport mechanism from the gas solid interphase. The unreacted molecules diffuse through the gas/solid interphase, into the pores and get adsorbed on an active site. There the chemical reaction occurs and the products diffuse out of the pores through the interphase and leave the reaction zone with the gas stream. There are three general processes that control the reaction kinetics of a gas/solid reaction. These three processes are:

- Diffusion;
- Phase boundary reactions;
- Nucleus growth.

In every gas/solid reaction diffusion processes occur and they can be the rate determining process in the reduction. Three different diffusion processes are distinguishable. They differ in the place of appearance and the activation energy. These three processes are:

- Volume diffusion
- Grain boundary diffusion
- Surface diffusion

In this work volume diffusion is not considered because this kind of diffusion becomes important only at high temperatures above 900 °C [70]. In the case of iron oxide reduction the active sites are not just located inside the pores. The entire particle acts as an active surface and so the first reaction is the reduction of the highest iron oxide haematite to magnetite on the particle and the pore surfaces. This reaction can be formulated as a simple change from haematite to magnetite. To understand this transformation of the iron oxides it is important to remember that the magnetite is a mixed crystal built up of haematite and wustite compounds. To go further in the detailed consideration the magnetite Fe_3O_4 is better described as $FeOFe_2O_3$. During this initial reaction the oxide matrix changes from a hexagonal/trigonal to a cubic crystal system causing tensions inside the contact mass. The change in the crystal system causes an initial reduction time period. This is obvious because the different crystal systems have different activation energies to remove the oxygen out of the lattice. The schematically reaction is illustrated by *Figure.16*.

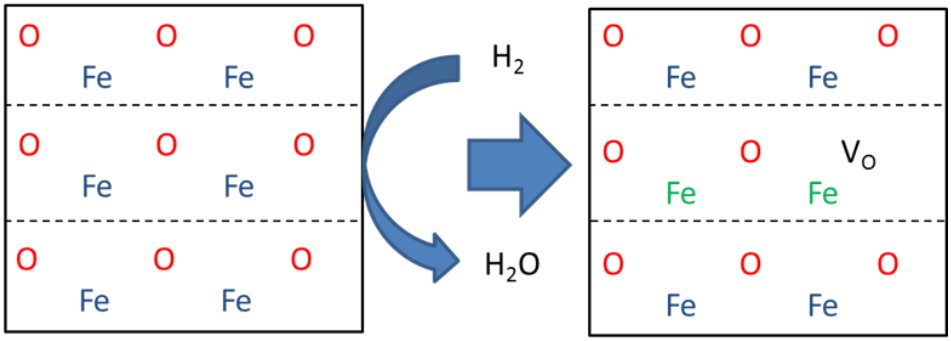

Figure 16: A simplified illustration of the oxygen removal of the theoretical stoichiometric haematite; red: O^{-2}; blue: Fe^{+3}; green: Fe^{+2}.

2 Reaction mechanisms

The *Equation.27* describes the oxygen removal from the surface of the haematite to form magnetite. As described above magnetite, is correctly described by $FeOFe_2O_3$ instead of Fe_3O_4.

$$3\ Fe_2O_3 + H_2 \rightarrow 2\ FeOFe_2O_3 + H_2O\ (surface) \qquad (27)$$

In *Equation.27* no defect electrons or vacancies appear. To keep them in mind, this reaction can also be expressed with the Kröger-Vink notation and is illustrated in *Equation.28*.

$$2\ Fe^{x}_{Fe} + O^{x}_{O} + H_2 \rightarrow 2\ Fe'_{Fe} + V^{\bullet\bullet}_{O} + 2h^{\bullet} + H_2O \qquad (28)$$

3 haematite compounds react to 2 magnetite compounds. The oxide states of the iron ions are +3 in the haematite, to acquire electric neutrality. The oxidation states have to be an even number and that is the reason why the magnetite occurs in a mixed crystal. To illustrate this explanation the oxide state of iron ions in formal magnetite would be 8/3 and this oxidation state is not allowed. The consequence of this forbidden oxidation number is that two +3 iron ions changes to +2 ions to acquire electrical neutrality. The compound of a Fe^{+2} ion in combination with the O^{-2} ion is representing the wustite FeO phase of the iron oxide. So the first occurrence in the reaction is the formation of a thin film of wustite compounds with Fe^{+2} ions. As soon as the wustite containing film is formed mass transport processes occur. Wustite is known to have a cation deficit crystal structure and has a lot of vacancies in the lattice. So once the wustite compounds have formed the reaction mechanism of the surface reaction gets overlaid by an internal diffusion process *Equation 29*.

$$Fe_2O_3 + FeO \leftrightarrow Fe_3O_4\ \ [=FeO(Fe_2O_3]\ \ (inside\ the\ oxide) \qquad (29)$$

It is pointed out that the wustite compound appears already in the very beginning of the reduction. The consecutive intrinsic reduction can be written as the wustite reduction at the gas/solid interface [71,72].

$$V''_{Fe} + 2h^{\bullet} + FeO + H_2 \rightarrow Fe^{+2} + H_2O \qquad (30)$$

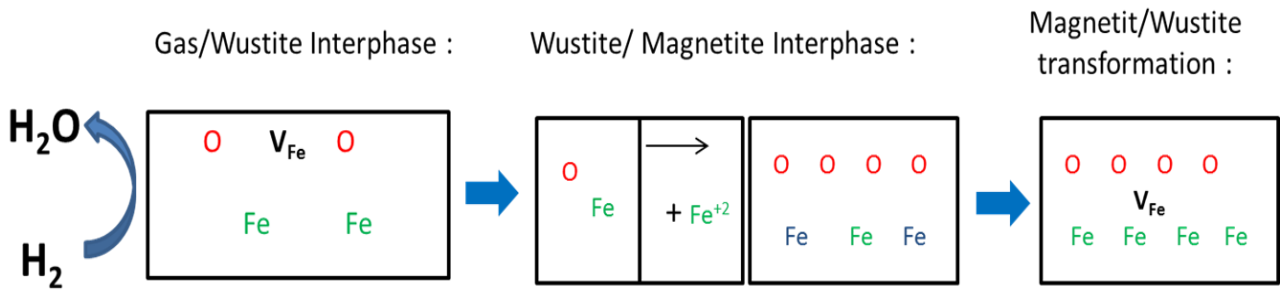

Figure 17: At the first reaction step a vacancy site is eliminated as described by *Equation 27* at the gas/solid interphase (left). In the second reaction step at the wustite/magnetite interphase, the so called internal reduction occurs, the released Fe^{+2} ion moves to the magnetite phase (middle). The insertion of an Fe^{+2} ion into the magnetite phase with vacancy site production finalizes the transformation to wustite (right).

2 Reaction mechanisms

During this gas/solid interphase reaction Fe^{+2} vacancies, defect electrons and oxygen are removed out of the lattice *Equation.30*. Simultaneously Fe^{+2} ions are produced and placed on iron vacancy sites inside the lattice. The consumed vacancies are reproduced during the reaction on the wustite/magnetite interphase. This reaction can formally be described by the *Equation.31*.

$$Fe_3O_4 + Fe^{+2} \rightarrow 4\ FeO + V''_{Fe} + 2\ h^{\bullet} \quad (31)$$

This reaction is in the beginning of the process much faster than the gas/solid H_2/FeO interphase reaction and so there is a thermodynamic equilibrium at the wustite/magnetite interphase. This reaction requires Fe^{+2} ions diffusion from the gas/wustite interphase to the wustite/magnetite interphase and a counter current diffusion of vacancies and defect electrons. The removal of oxygen from the wustite surface leads to a decrease of iron vacancies. The formation of metallic iron only occurs if the accumulation of iron ions reaches the concentration of the equilibrium value between wustite and iron according to the Baur-Glaessner diagram. When the transition between vacancy refilling and iron formation starts is depending on the velocity of the oxygen removal and the additional delivery of vacancies from the inside of the oxide**.** The iron formation itself produces vacancies according to *Equation.32.*

$$Fe^{+2} \rightarrow Fe_{metal} + V''_{Fe} + 2\ h^{\bullet} \quad (32)$$

It has to be kept in mind that no hydrogen is consumed during this reaction and if the reaction proceeds long enough the produced Fe^{+2} ions can occupy iron vacancies or form metallic iron following *Equation.33* [68,72]. The iron formation can also be caused by a reversible wustite transformation/disproportion that is formulated by *Equation.34.*

$$3\ Fe^{+2} \leftrightarrow 2\ Fe^{+3} + Fe_{metal} \quad (33)$$

$$Fe_3O_4 + Fe \leftrightarrow 4\ FeO \quad (34)$$

The reaction from *Equation.34* just takes place below 570 °C and above the opposite reaction direction is dominant. Formation of metallic iron is favoured on defect sides of the surface. Those defects are grain boundaries, lattice defects, dislocation lines and heterogeneous agglomerations [68]. Also during the lattice formation from the hexagonal/ rhombohedra haematite lattice to the cubic magnetite/wustite lattice a lot of defects are produced. There are two main reasons for this phenomenon. One is a volume expansion from the hexagonal to the cubic lattice and the second is the anisotropic reduction velocity of the hexagonal lattice. The resulting tension and the anisotropic reaction velocity forces the crystal to brittle and create breaks in the oxide [70-73]. Once the metallic iron is covering the wustite the mass transport changes from cation Fe^{+2} diffusion to a mixed cation and anion O^{-2} diffusion.

The iron ions move to the inside of the iron oxide and the oxygen ions move through the iron lattice to the outside of the particle. This oxygen diffusion through the iron is very slow and can be the rate determining step in the reaction. The slow diffusion kinetic is easily explained by comparing the ionic radii of iron and oxygen ions which are shown in *Table.8*.

Table 8: Comparison of the radii of the participating species [75]

elements	O^{-2}	Fe^{+3}	Fe^{+2}	Fe°	Al^{+3}
Radii [pm]	136	64	78	140 - 156	50

The metallic iron precipitation can have three different morphologies which influence the sintering behaviour enormously. As mentioned before sintering is one of the main reasons for causing a weak long time stability of the contact mass.

These three morphologies are classified into: tight, oriented and porous. The porous form is favourable because it creates a bigger surface and the wustite is not totally covered by iron. The tight form lowers the reduction kinetics dramatically and the orientated morphology causes agglomeration [71-76].

Which kind of morphology is produced is dependent on the iron ion production rate and the diffusion ability of the ions. In the case of the tight morphology the production rate is faster than the diffusibility of iron ions. As a consequence new iron particles form and melt together with the surrounding ones. The opposite situation is the case if oriented morphology occurs. Here the production rate is lower than the diffusibility and the produced ions Fe^{+2} migrate to the few already existing iron precipitates and enable length growth there. The desired porous form will only result if both parameters are balanced. The different morphologies are shown in *Figure.18*.

2 Reaction mechanisms

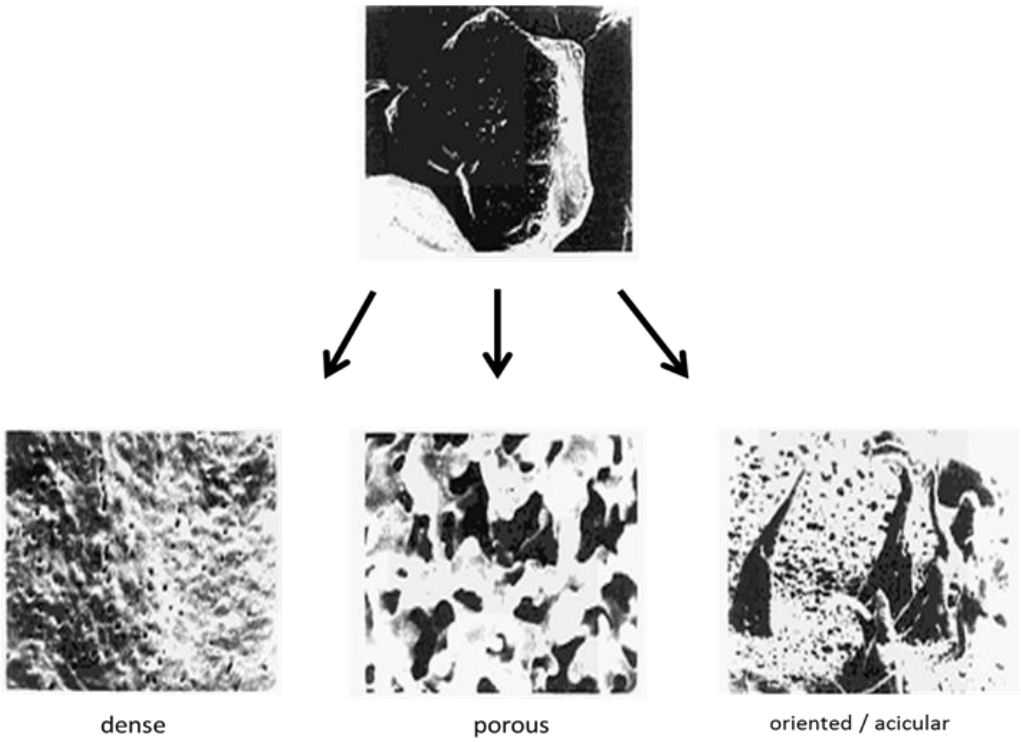

Figure 18: The three different morphologies of fresh released iron; tight (left); porous (middle); whisker growth (right) [76].

The orientated morphology is built up of needles which are also called whiskers and these needles can agglomerate resulting in a loss of surface. Another mechanism that can cause sintering is the formation of a liquid interphase between the wustite and its additives. This formation is just considerable at high temperatures above 850°C. In the case of reduction with hydrogen no orientated morphology will be observed because the production rate of the ions is high. Also the liquid interphase should not appear if pure iron oxide without any gangue is used. The mechanism that can cause sintering is described by the chemical activity of iron. The reactivity of freshly formed iron is much higher than that of earlier produced one. That is the reason why they tend to smaller surfaces and adhesion forces are active during reduction. If the amount of fresh produced iron is high enough sintering can happen. The presence of enough fresh iron is necessary for sintering [72,79,81]. The whole reactions that are explained in this chapter are summarized, simplified and graphically shown in the flow schema in *Figure.19*.

2 Reaction mechanisms

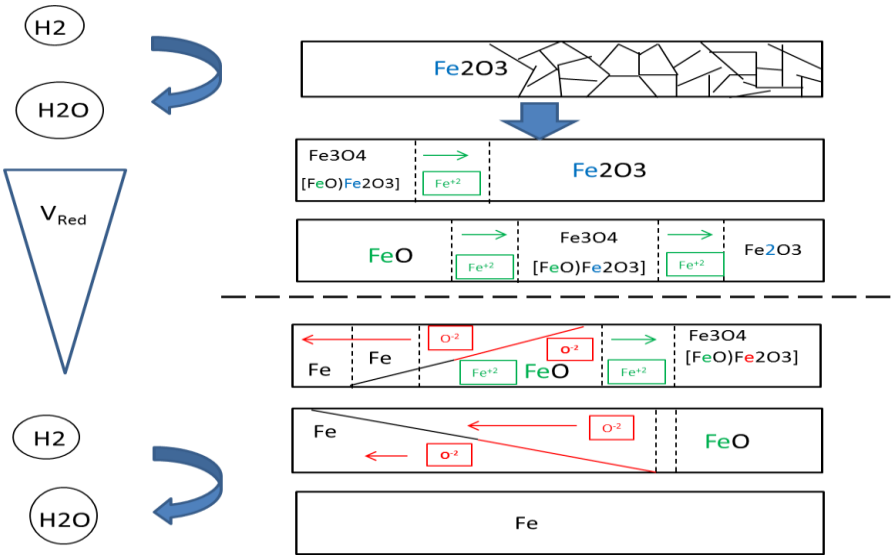

Figure 19: The reaction schema and the solid diffusion processes during reduction of the iron oxides with hydrogen

The first iron oxide species in the flow schema is haematite. The angled objects in the first rectangle are representing many grains of this species. In the following reaction steps the graphic represents one single grain and one can mention that the left side is meant to be the grain boundary and the right side the center of the grain. The phase boundary reactions are favoured on grain boundaries but also enter the inside of the grain. These boundaries are also often the origin of cracks. Because of simplicity just a single grain is represented here. It is highlighted that below the dotted line in *Figure.19* the metallic iron is covering the particle and the reduction kinetic becomes very slow with continuing iron production. This situation was proven to be true for an oxide pellet that was not completely reduced. *Figure.20* shows a particle with a tight metallic outer layer and a porous oxide inside. The magnification of the particle edge shows that tight metallic iron is covering the residual oxide of the particle.

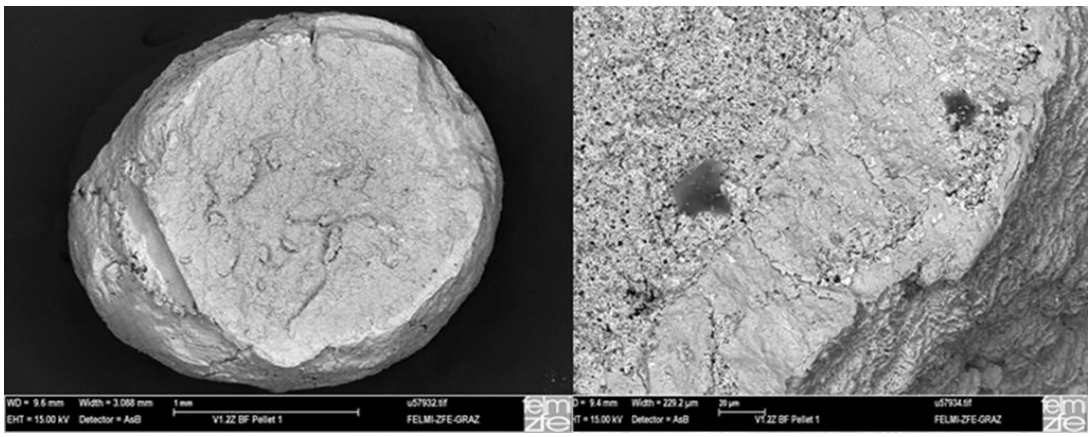

Figure 20: A crushed iron oxide pellet where just the outer region is reduced and the inside is still porous (left). The magnification of the edge of the pellet (right) [FELMI-ZFE-Graz].

2.1.2 Interactions of the aluminium oxide with the contact mass

The influence of aluminium oxide on the iron oxide has been investigated by many scientists [82]. Most of the literature that can be found comes from the field of metallurgy because aluminium is a typical gangue. A very common topic is the iron production via the blast furnace process [83]. The results always showed the same trends and so there appears to be a collective sense of agreement among all the researchers. Aluminium oxide is solved in the iron oxide lattice and Fe^{+3} ions got replaced by Al^{+3} ions. The solubility of aluminum oxide in wustite at 900°C is 0.5 wt % (0.33 mol %) [78]. If more aluminium oxide is added a wustit aluminium oxide intermediate is formed that is called hercynite. This hercynite can cover the wustite particle and act as a diffusion barrier. Aluminium oxide lowers the reduction rate and enhances the formation of tight iron morphology at the surface of the oxide. The reason for this behaviour is explained by a contraction of the oxide lattice. The contraction is caused by the smaller ion radii of aluminium ions compared to the size of iron ions. This contraction decreases the diffusion ability of the ions. The tight iron layer on the oxide particle causes very slow transport processes and this is also a reason for the decrease of the reduction velocity. Hercynite formation happens mostly at the surface of the oxide particles because the formation enthalpy on the surface is lower than anywhere else in the particle. If hercynite particles are formed they can cover the surface and act as specimen foreign compounds. These specimen foreign particles are equal to surface defects and surface defects favour iron precipitation. So the hercynite itself acts as a catalyst for the iron precipitation and it was shown that the first iron is formed at the wustit/hercynite interphase [84]. If the hercynite is covering the whole particle or the hercynite precipitations on the surface are big enough they show good ‘spacer’ properties and hinder the particles to get in contact with each other. Another feature of the hercynite is that it lowers the chemical activity of freshly formed iron and decreases attractive forces between the particles [85,86]. In the experimental setup of this work the contact mass consists of pure haematite and pure aluminium oxide. During the first reduction the aluminium oxide is dissolved and the excess aluminium oxide reacts with wustite to form hercynite. The hercynite cannot be oxidized with steam but reduction to Fe and Al_2O_3 with hydrogen is possible. The three situations how hercynite interacts with the iron oxides are illustrated in a simplified way in the *Figure.21*.

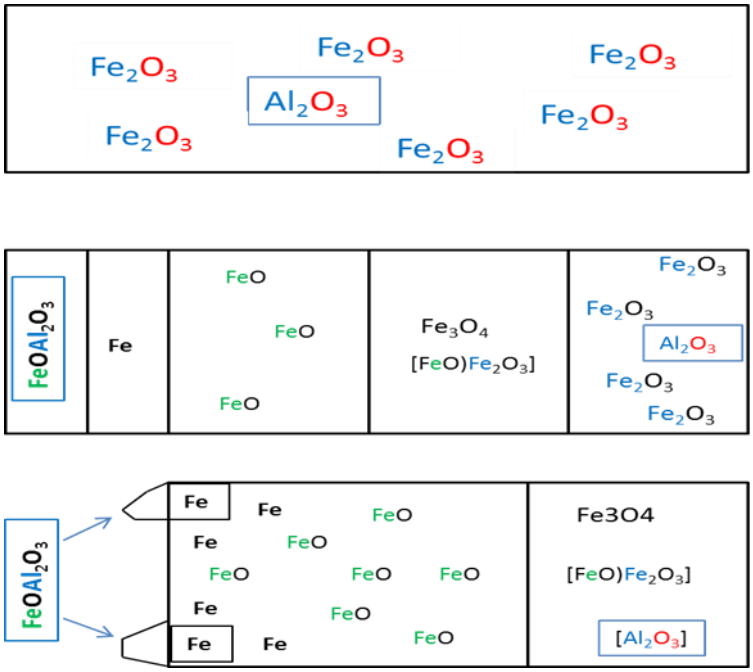

Figure 21: Aluminium oxide is dissolved in haematite and no hercynite is formed (top). During the reduction wüstite reacts with aluminium oxide to form hercynite and covers the contact mass (middle). Because it acts like a catalyst the first iron is formed at the hercynit/wustite interphase. Hercynite formation if the aluminium oxide is not dispersed well (bottom).

2.1.3 Mechanism of the iron oxidation

In this chapter the reverse reactions of the iron oxide reduction are considered. The situation with the mathematical description concerning the reaction kinetics is the same as it is in the reduction process. The same species are involved but the reaction mechanisms and the kinetics differ widely. The information about the oxidation of iron is commonly related to oxidation conditions in air or in other oxidizing atmospheres and they do not evaluate the influence of moisture in the oxidizing atmosphere. Thanks to metallurgic research there is some information available about the oxidation of iron under humid conditions [86,103]. The reactions that take place can be formulated as a reaction of iron with water to its different oxides and hydrogen. The schematic process of the reaction is shown in *Figure.22*. In this figure the formula Fe_xO_y represents the first and second oxide species of iron. The mass transport processes are shown and described by the formal chemical reaction. The flux of vacancies was ignored but is equivalent to the flow of electrons in the opposite direction. It is to note that this figure represents a single grain.

2 Reaction mechanisms

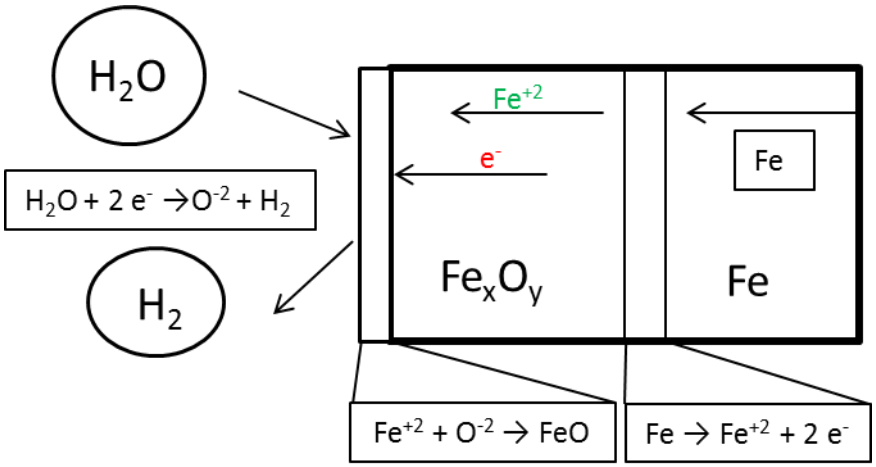

Figure 22: Mass transport processes during oxidation of iron with steam.

The reaction kinetic is quite similar to the reduction in terms of an initial phase, a following linear kinetic that is shifting to a parabolic one when the reaction proceeds. The initial period is surface controlled and is described by adsorption of a water molecule following *Equation.37* and the insertion of oxygen *Equation.36*. In the following equations S denotes a vacancy surface site and the straight line (|) shows the situation of an adsorbed molecule on an ion [92].

$$2e^- + H_2O \mid S \leftrightarrow k_1 \leftrightarrow O \mid S + H_2 \quad (35)$$

$$O \mid S \leftrightarrow k_2 \leftrightarrow O^x_O + S \quad (36)$$

$$H_2O + S \rightarrow H_2O \mid S \quad (37)$$

The water molecule in the hot stream is in an excited state and is oscillating between other gas molecules. To react with the iron it has to hit a vacant surface site of iron. The frequency of the hits is strongly temperature and concentration dependent. The concentration dependency becomes unimportant above a specific concentration were the vacancy sites are saturated or diffusion processes dominate the process. This situation can be described by *Equation.35* and *36* if k1 is smaller than k2 and vice versa.

The *Equations.35* describes the electron transfer and the oxygen insertion which is correlated to hydrogen generation. This reaction is the rate determining step at the beginning of the reaction. It is supposed to be a two-step mechanism that is taking place here. This reaction can be written by the *Equations.38* and *39*.

$$H_2O + S \rightarrow OH \mid S + \tfrac{1}{2} H_2 \quad (38)$$

$$OH \mid S \rightarrow O \mid S + \tfrac{1}{2} H_2 \quad (39)$$

The electrons which are consumed during this step are freely available on the surface because of the electron delocalization in the metal. The electron availability decreases with consecutive reaction. This effect becomes dominant when magnetite

starts to form. *Equation.40* shows the insertion of the oxygen into the lattice on a regular oxygen position and the regeneration of the vacancy surface side.

$$H_2O \rightarrow H_2 + O^x_O + V''_{Fe} + 2\,h^\bullet \quad (40)$$

If the vapor adsorption takes place inside a crack or a hole, hydrogen formation will appear. This hydrogen can react like described before with an oxide to form water or it interacts with the lattice and produces point defects [88,89]. This situation is illustrated in *Figure.23*.

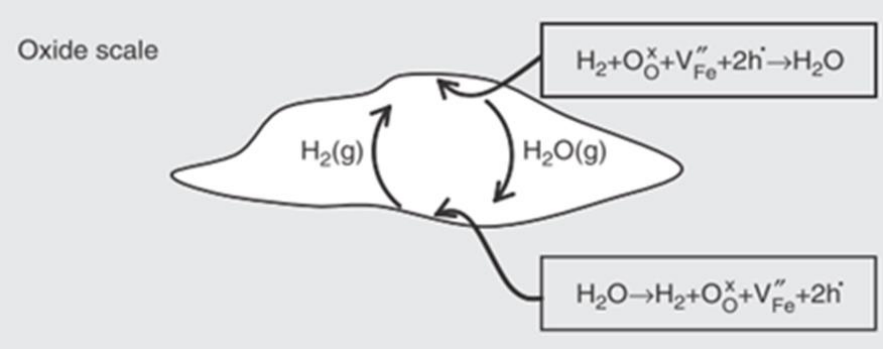

Figure 23: Schematic oxygen insertion within a cavity supported by H2O [85]

Also this situation can be described by Kröger-Vink-notation. The molecular hydrogen interacts with lattice oxygen which is located on a normal oxygen side inside the lattice to produce negatively charged hydroxyl ions on this side. The lonely hydrogen ion occupies an intrinsic lattice site and has a positive charge. Intrinsic means that it is located between two regular occupied sites.

$$H_2 + O^x_O \rightarrow OH^\bullet_O + H'_i \quad (41)$$

It was mentioned before that electron and ion transport decrease if magnetite is formed. This assumption can be explained by the growth rate and the diffusibility of the different oxides [91– 96]. Wustite has the fastest growing rate of the iron oxides and forms tight or porous layers [97]. This behaviour has been verified by many researchers and is shown in *Figure.24*. The wustite has a very good permeability with respect to iron ions because of its non-stoichiometric nature. Because of this property the mass transport happens so fast that the surface reaction is the rate determining step. When the wustite scale becomes too thick and the ways of mass transport are very long or if the oxide magnetite is formed the transport processes decrease. To understand this change in transport processes it is important to know that at the phase boundaries the transport processes are behaving like a quasi-equilibrium reaction. The phase boundary equilibrium reactions start immediately after a new phase of oxide is formed. These reactions become more and more dominant with continuing scale growth. The decrease of transport processes can be described by the reduction of the concentration gradient which is the common driving force in a diffusion process. From another aspect the decrease is explained by the degradation of the electric field that is caused by the different oxygen potentials of the oxides.

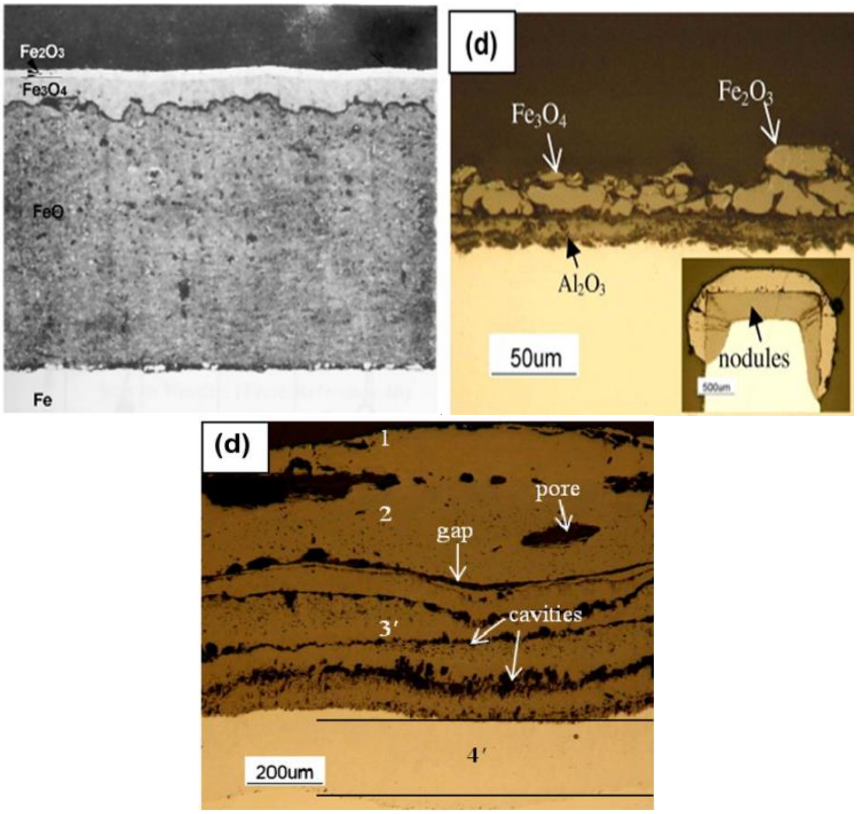

Figure 24: Scale growth in dry oxidizing atmosphere (left); Scale growth in wet atmosphere of a 6wt % Al sample (right); Scale growth with wet atmosphere of a 2wt % Al sample (bottom) [98,99].

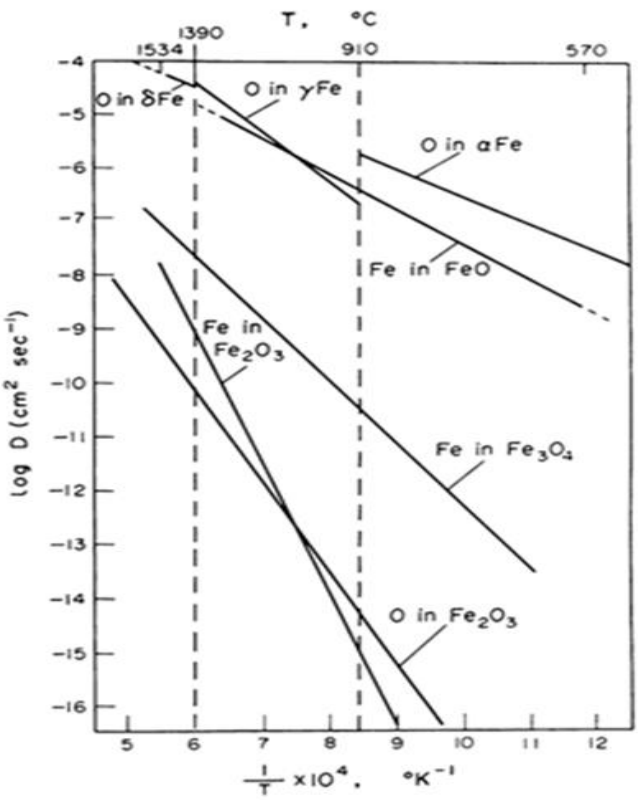

Figure 25: The diffusion coefficients of the different ions in the metal/metal oxide matrix [100]

In *Figure.24* and *25* the diffusibility of iron ions in different oxides and the difference between dry and wet oxidation are shown. It has to be kept in mind, that the oxide scales shown in *Figure.24* at the left side, were produced in dry atmosphere with oxygen and without vapor in the oxidizing atmosphere. Water reacts much faster than oxygen and shows a totally different reaction path. Water produces a porous structure with holes in it. Grain boundaries are favoured for transport processes and in the case of water molecules it seems to have enormous effects. The consequences of the oxidation in humid atmosphere are illustrated in *Figure.24* on the right side and on the bottom. All of the described processes that can happen are responsible for this phenomenon. To finish this chapter the occurring stresses during oxidation and temperature changes are considered. Oxidation is connected with volume change which can cause deformation or strains inside the oxide. Pilling and Bedworth suggested an oxide growth by inward oxygen transport [103]. They found that if the ratio V_{Ox}/V_M is greater than one the resulting expansion can put the oxide into compression whereas if the ratio is lower than one, tension and a discontinuous oxide results. They defined V_{Ox} as the oxide volume at a specific reaction state and V_M as the metal volume at the same state. In the practical situation where $V_{Ox}/V_M > 1$ and outward metal transport is the dominant mechanism the formation of new oxide will occur on the free gas/solid interphase and no stresses will be produced [102,103]. As mentioned before that during oxidation both of the described mass transport paths occur. If the inward oxygen transport is favoured the new oxide formation will be located on the oxide/metal interphase. Because of the mixed reaction paths new oxide formation will occur on both the surface and the bulk of the oxide lattice. This mixed transport processes become possible if grain boundaries and/or microcracks facilitate oxygen access. Formation of new oxides on the grain boundaries causes lateral stress and deformation. The stress development is illustrated in *Figure.26*.

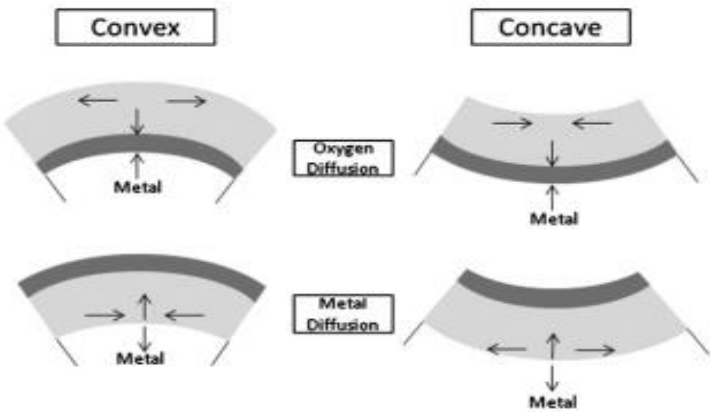

Figure 26: The different ways of mechanical stress development during oxide growth.

They also suggested that plastic deformation increases by decreasing oxygen activity and smaller grain size. Oxidation can stress the contact mass (growing oxide) also in other ways like a dissolution of oxygen inside the metal and internal precipitation of

heterogeneous oxides ($FeOAl_2O_3$). Finally it can be concluded that all these strains developed by volume expansion will result in tensile stress.

The stress development caused by temperature changes is derived by the significantly different thermal expansion coefficients between the orin oxides and aluminium oxide. The expansion coefficients of iron and its oxides as well as for aluminium oxide are listed in the *Table.9*. It is clear that the thermally induced stress is dependent on the magnitude of temperature change and the difference between the expansion coefficients.

Table 9 : Thermal expansion coefficients of the different contact mass materials [98]

Material	$10^6 \alpha$ / K^{-1}	T / °C
Fe	15.3	0 – 900
FeO	15	400 – 800
Fe_2O_3	14.9	20 – 900
α Al_2O_3	5.1 – 9.8	30 - 1100

Both stress processes are considered without stress relieving processes which in reality do happen. One stress relieving process is plastic deformation, a process that occurs at low temperatures by dislocated movement and by creep at high temperatures. If the produced stress is too high to get released by plastic deformation mechanical breakdown of the grain will occur. This mechanical breakdown can cause voids, cracks and spallation of the iron oxide scale. So it is assumed that the contact mass changes its morphology during the oxidation especially through cyclic exposure. This change of the grain shape will be minimal if all adjustments in terms of gas composition, grain-, pore size and additives are well balanced. If these adjustments are not well balanced the effects will be noticeable. The voids and cracks can favour the reaction kinetics because of easy gas accessibility. If spallation of the oxide scale happens the performance of the contact mass will decrease. It can be mentioned that small pieces of the oxide scale will fall down on the bottom of a tubular reactor and will plug the gas entrance or exhaust depending on the reactor design. So the knowledge of all possible stress producing factors is important to influence the stability of the contact mass. It is required that the contact mass shows a stable and homogeneous reaction path to use it in long time applications. Because of the complexity of the influence factors it was till now not possible to estimate the cyclic long time behaviour satisfactorily. Consequently more experimental data and mathematical models have to be acquired. In the next chapter the experimental procedure and the results are considered.

3 Experimental:

Because of the absence of analytical data in the literature there are still many factors that are not completely understood or optimized, e.g. the composition of the contact mass, the reaction temperature, the gas flows and the grain size. In this work the stability of the contact mass was investigated for a 5 wt %, 10 wt % and 20 wt % sample (weight percent aluminium oxide on haematite) at 600°C and 750°C under isothermal reaction conditions.

To verify the assumption that changing the temperatures will harm the sample a dynamic measurement mode was performed in which the reduction temperature was 750°C and the oxidation temperature was 600°C. Before every reaction step a purge phase with inert gas N_2 was conducted to get a defined atmosphere. The measurements were carried out with six different samples which were either self-prepared or supplied by team colleagues. The used samples were:

Iron sponge powder: direct reduced iron from Alpha Aersa

Fe / Al_2O_3 5 % self-prepared with 5 wt % aluminium oxide

Fe / Al_2O_3 10 % self-prepared with 10 wt % aluminium oxide

Fe / Al_2O_3 20 % self-prepared with 20 wt % aluminium oxide

V2: Haematite with 10 wt % aluminium oxide

V7: Haematite with 10 wt % aluminium oxide

3.1 Sample preparation

3.1.1 Wet Impregnation

With the exception of V2, V7 and the pure sponge iron the samples were prepared using an impregnation method similar to the one described by C.D Bohn et al. [30].

The impregnated iron samples were produced with sponge iron powder (≤ 100 mesh; 99.9 % purity; Alfa Aersa) and aluminium nitrate (≥ 98 % purity; Fluka). The nitrate had nine parts crystal water bound per molecule and the correct name is aluminium nitrate nona hydrate. $Al(NO_3)_3 \cdot 9 \cdot H_2O$ was dissolved in deionized water and heated up to 80 °C degrees in a three neck flask with an attached thermometer. The amount of water, which was tested before, was chosen in the way that it was just enough to cover the iron powder. Then the iron powder was added in small doses to ensure that every particle got in proper contact with the support solution. After adding the iron a reflux condenser was attached to avoid that any water left the reaction flask. The mixture was held at 80 °C for 24 hours because the wet impregnation is diffusion

controlled and needs time to reach equilibrium. The aluminium nitrate nona hydrate is known to release its crystal water at 73 °C and the salt has a degradation temperature of 150 °C. The flask was shaken several times to achieve a good mix. Magnetic stirring was not possible because of the ferromagnetic nature of iron. To evaporate the water the condenser was replaced and the temperature was slightly increased. The dry impregnated powder was transferred to an oven and heated up to 350°C for 2 hours to get rid of the nitrates NOx and to form the aluminium oxide. Then the sample was spread out on a ceramic bowl and calcined at 900°C for 10 hours. The calcination was important because at this temperature structural changes occur and the aluminium ions can distribute homogeneously through the whole iron matrix in terms of surface and pores. After the calcination the ready and fully oxidized contact mass was one solid piece. The mass was crushed and fractionized by sieving. The selected grain size was between 90 and 125 µm.

3.1.2 Dry mixing

The pure iron sponge did not undergo any treatment and the V2 and V7 samples were prepared by dry mixing of haematite (≤ 325 mesh; 98 % purity; Alfa Aersa) and aluminium oxide (purum p.a.; Fluka) with the desired aluminium oxide loading. The samples were pelletized and calcined. The calcination was done in the same way as in the wet impregnation method. After the calcination the compact mass was crushed in an agate mortar. A final sieving step was done to obtain the same grain size as in the other testing series.

3.2 Measurement apparatus

Hardware:

The contact mass was analyzed in an STA 449C Jupiter from Netzsch company. The STA (**S**imultaneous **T**hermal **A**nalysis) provides the opportunity to perform a thermo gravimetric (TG) and a differential scanning calorimetric (DSC) measurement at the same time. The principal construction of the STA is shown in *Figure.27*. The apparatus had a top loading system for the samples. The oven was connected with a lifting system for easy accessibility to the sample carrier. The different gas flows in the apparatus are shown. The balance chamber was thermally isolated and the temperature was kept at a constant value with a thermostat.

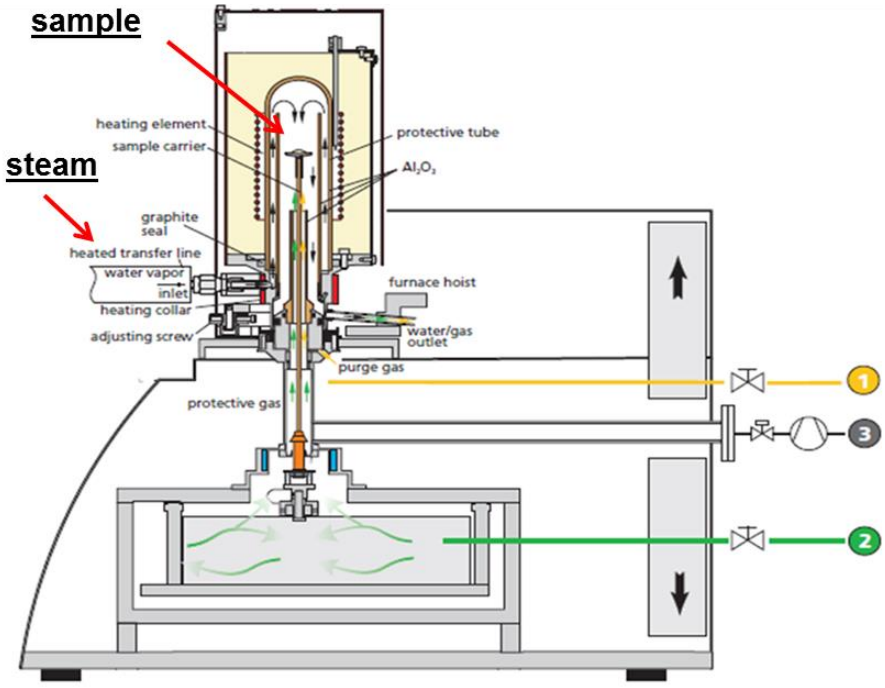

Figure 27: The STA 449C (Simultaneous Thermal Analysis) measurement apparatus with a water vapor oven. (1) gas supply for reactive gases. (2) Gas supply for filling gas of the balance chamber. (3) vacuum connection for evacuation of the apparatus.

There were two types of sample carriers for the different measurement techniques that could easily be changed between measurements. The sample carriers were attached on a sample holder and the sample holder had an electrical junction which was connected to the balance. The electrical junction on the end of the sample holder transmitted all information in terms of temperature, weight change and calorimetric changes to the balance and subsequently to the PC. The sample carriers / holders for the thermo gravimetric and the differential scanning calorimetric measurements are shown in *Figure.28*. Both were built up of an aluminium oxide capillary that had a type S thermocouple embedded and an electrical junction for the balance connection. The thermocouple at the end of the capillary detects the temperature change of the sample and is highlighted with the red arrows in *Figure.28*.

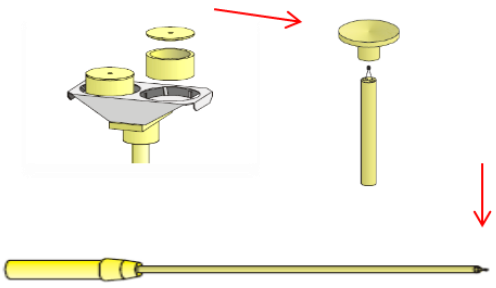

Figure 28: The DSC sample carrier for the STA (top, left); The TG sample carrier (top, right). The sample holder with the electric junction for the balance (left side) and the thermocouple (right side) (bottom).

4 Experimental Results and Discussion

In the case of a thermo gravimetric measurement no reference crucible is required. In case of a differential scanning calorimetric measurements the sample carrier has two crucibles and two thermocouples. The two crucibles and the thermocouples are shown in *Figure. 29*. The specifications of the STA apparatus are shown in *Table.10*.

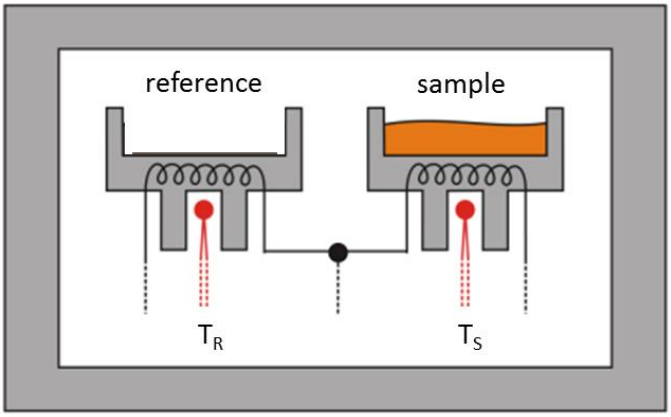

Figure 29 : The schematic construction of an heat-flux DSC sample carrier, (red dot) thermocouples, (black wire) heat-flux sensor, (gray housing) oven [99].

Table 10: The specifications of the STA apparatus.

Temperature range:	From room temperature to 1200 °C
Initial weight:	Max. 5 g
mass resolution:	0.1 µg
temperature accuracy:	< 1K
Enthalpy determination	± 3 %
Gases: inert N_2	0 – 250 ml / min
Reduction H_2	0 – 250 ml / min
Oxidation Steam	0 – 20 g / h

The measurement apparatus had several other devices like a separately heated transfer line, a heating collar inside the oven, a safety shut down system for the steam and a temperature controlling unit for the exhaust gas outlet adapter.

With all these extra devices the STA is capable to measure in humidified atmosphere. To prevent damage of the balance chamber a filling gas was always flushed through the balance system. The dry gases enter from the bottom and the steam from the top of the oven. A detailed view of the flow of the gases inside the oven is given in *Figure.33*. The arrangement of the gas flows was necessary to

enable the steam to get best contact with the sample. The measurement apparatus was attached to the controlling unit and the PC. With the measurement software (Proteus 6, Netsch) it was possible to control user specific temperature and gas profiles for the inert heating phase, the isothermal reduction, the purge phase and the subsequent oxidation.

3.2.1 TG/DSC

Thermo gravimetric analysis (TG)

The thermo gravimetric analysis is an analytical method where the change of mass as a function of temperature and time is detected. The sample is placed on an inert sample carrier and heated up inside a furnace. The sample carrier is connected with a micro balance and the balance measures the mass changes as function of temperature change. The sample chamber is normally purged with gas during the measurement. Mostly inert gases like nitrogen are used to avoid reactions of the sample with the gases.

If a heterogeneous reaction is under investigation the desired reactive gases are fed to the sample room. If a mass change occurs during the inert heating ramp this indicates that volatile impurities are contained in the sample or that the sample is not stable at this temperature. With the use of reactive gases a sample will change its mass according to the products produced. With this information a conclusion about the composition of the sample is possible. A TGA consists of an adjustable furnace, the sample carrier, the balance and a gas delivering system. In modern devices the apparatus is connected with a PC to evaluate the measurement data.

To determine the accuracy of the apparatus calcium oxalate monohydrate as common reference sample was tested. This substance decomposes in three defined steps and at specific temperatures. The ratios of mass loss are used to evaluate the accuracy of the balance. The decomposition process starts with the release of water and a mass loss of 12.3 wt %. In the second step carbon monoxide is released with a mass loss of 19.17 wt %. Finally calcium carbonate decomposes to calcium oxide with the corresponding mass decrease of 30.1 wt %. The measurements were highly reproducible (deviation < 1 %). The reference measurement is shown in *Figure 30* and *31*.

$$CaC_2O_4 \cdot H_2O \rightarrow CaC_2O_4 \rightarrow CaCO_3 \rightarrow CaO \quad (42)$$

4 Experimental Results and Discussion

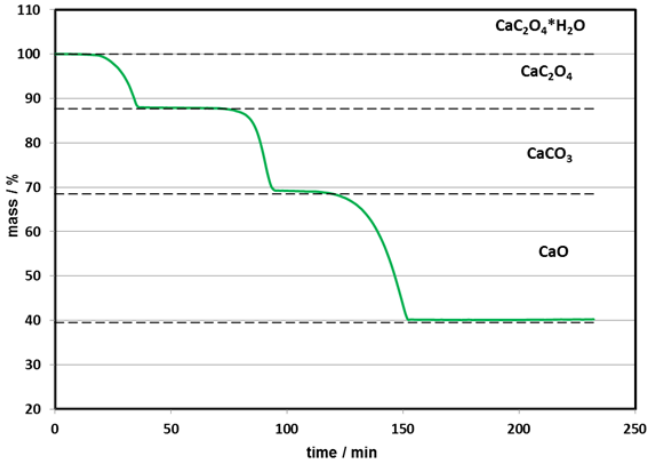

Figure 30: The reference measurement with calcium oxalate with a 5 K·min^{-1} heating ramp [ICVT Graz].

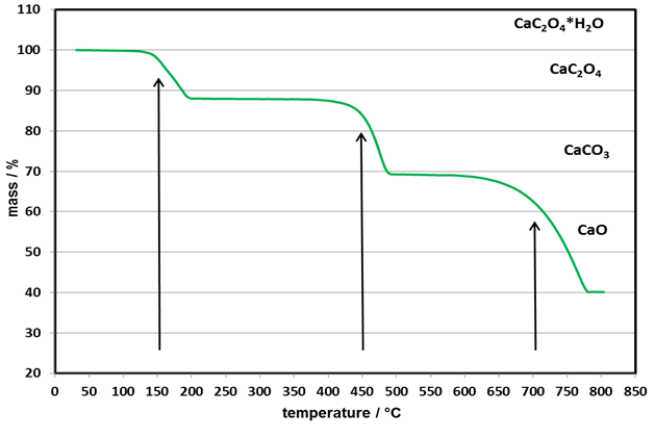

Figure 31: The oxalate measurement plotted against the temperature.

Difference scanning calorimetry (DSC)

The DSC method determines the heat absorption or release of the investigated sample. The sample is placed inside the STA in the measurement crucible next to an empty reference crucible. Both crucibles are located inside the furnace and undergo the same heating programm. The different heat capacities or occuring exothermic / endothermic processes yield to a temperature difference between the two crucibles. To determine the heat flux which is proportional to the temperature difference, a defined distance between the two crucibles is required. The heat flux sensor is located next to the crucible thermocouples *(Figure. 29)* and measures the thermovoltage between the sample and the reference. This allows for recording both the temperature difference and the absolute temperature of the sample and the reference. The temperature difference causes a thermo voltage (µV) in the senor and is converted into a heat flux difference (mW) by means of an appropriate calibration. The heat flux difference is finally converted into the reaction / transition enthalpies (J/g).

4 Experimental Results and Discussion

During a DSC measurement a defined and pure atmosphere is important to obtain correct results. A reference measurement was conducted to check the purity of the inert atmosphere during the heating ramp. Calcium oxalate mono hydrate was selected for the reference measurements. The three decomposition reactions are endothermic if the atmosphere is inert. If the atmosphere contains oxygen the decomposition of calcium oxalat to calcium carbonat is exothermic. This effect is caused by the formation of carbon dioxid instead of carbon monoxide Equations.43 and 44 [104].

$$CaC_2O_4 \rightarrow CaCO_3 + CO \qquad \text{(endothermic)} \qquad (43)$$

$$CaC_2O_4 + 1/2\ O_2 \rightarrow CaCO_3 + CO_2 \qquad \text{(exothermic)} \qquad (44)$$

The measurement started at 30 °C and ended at 850 °C with a heating rate of 5 $K \cdot min^{-1}$. Nitrogen was selected to produce a inert atmosphere. The first measurement showed an exothermic peak at the second decomposition step and indicated that some oxygen was present inside the STA Figure.32. After retightening the gas sealings a second measurement with a heating rate of 10 $K \cdot min^{-1}$ was conducted. The second measurement did not show a exothermic peak and the atmosphere was considered to be inert Figure.32.

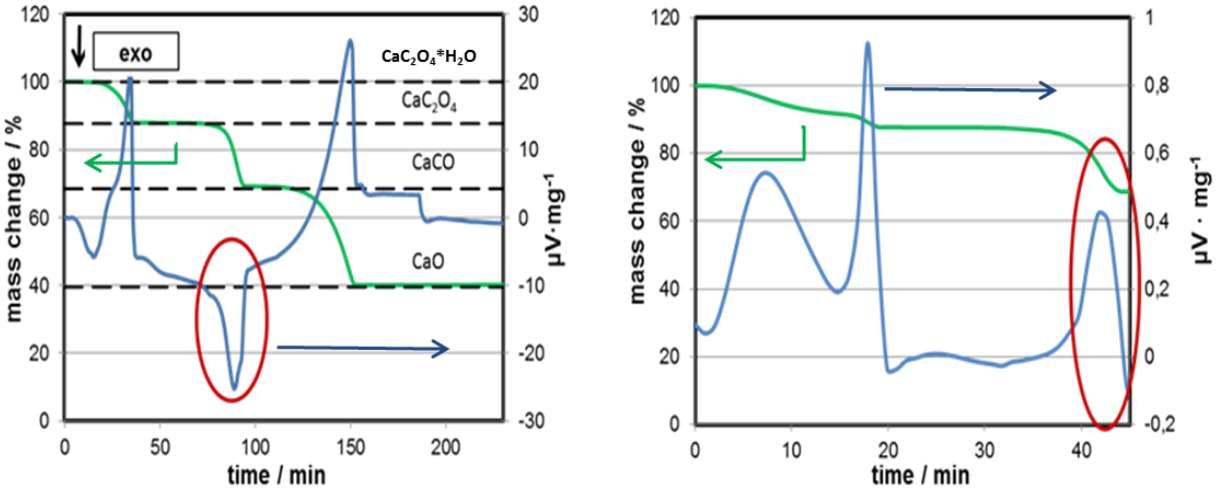

Figure 32: The DSC/TG signals from two reference measurements; The exothermic peak at the second decomposition reaction (left) and the second reference measurement without an exothermic peak (right) .

.

3.2.2 Temperature and reaction program

To start an STA measurement, heating ramps, isothermal periods and the gases are to be selected (software Proteus 6). The software controls the temperature of the oven and the segment temperature control (STC). The STC button activates the thermocouple controller of the sample. This controller is a PI regulator and actuates the PI regulator of the oven. The consequence of this arrangement is that the sample regulator controls the oven regulator. If the STC is not selected the oven regulator ignores the sample temperature and follows the chosen temperature program. If the STC is activated the oven regulator tries to keep the sample at the chosen temperature programmed in the software. The STC is necessary if a reaction under defined isothermal conditions is investigated. A disadvantage of the STC is that it produces overheating and undercooling of the sample temperature. These effects are caused by the heat capacities of the samples. The sample requires some time for heat absorption. Because of this delay the oven will always have a higher temperature than the sample during the heating ramp. At the end of the heating ramp the oven still has a higher temperature and the sample will be overheated. The STC regulates the temperature down and undercooling of the sample is the consequence. This effect is increased with the spatial separation of the thermocouples by the protective tube between them. Both thermocouples are shown in *Figure.33* and highlighted by the red arrows.

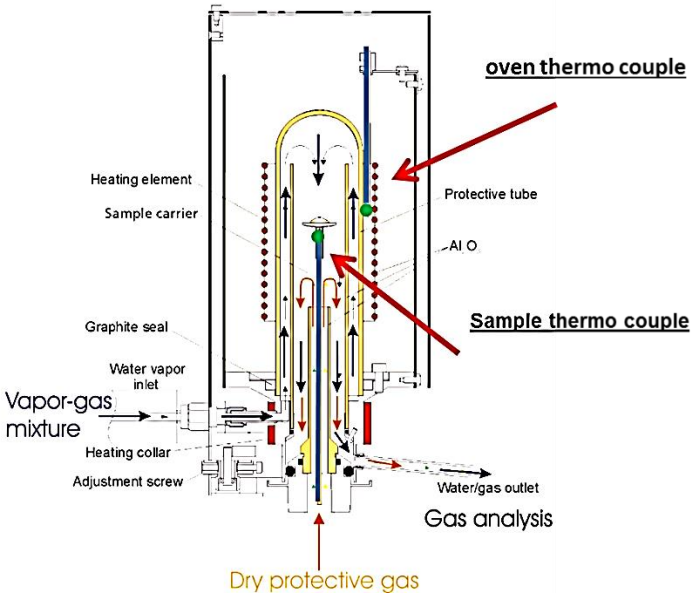

Figure 33: The STA 449C (Simultaneous Thermal Analysis) water vapor oven with gas flows and thermocouples (blue rod with green head).

The effects of overheating and undercooling are shown in *Figure.34*. The given temperature ramp included the heating of the sample up to 750 °C, then to keep the temperature constant and finally to cool the sample down to 600 °C. During the heating phase the sample temperature rose up to 765 °C and produced a peak in the temperature curve that can be seen in *Figure.34*. This peak is followed by a second one that was produced by changing the gas atmosphere inside the oven from inert to reducing atmosphere N_2/H_2. During the cooling phase the temperature fell below the programmed value. After the sample reached 600 °C a little overheating peak occurred that was followed by a second little one. The first peak shows the overregulation of the oven and the second one is affected by the change of the gas atmosphere from inert to oxidizing atmosphere N_2/H_2O.

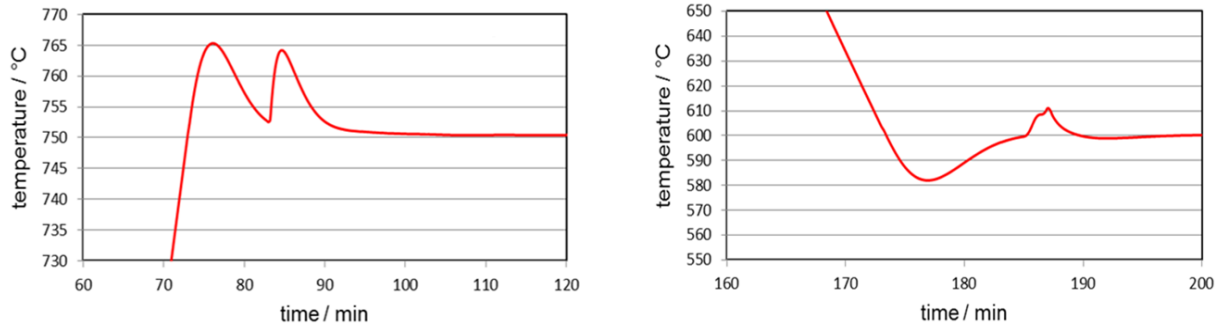

Figure 34: Characteristic behaviour of the STC mode during a heating (left) and a cooling period (right).

After the change of the gas atmosphere it took some minutes to reach the desired temperature. After the desired temperature was reached the oven managed it to keep the temperature constant. The problem of the overheating peak was solved by selecting slower heating rates at the end of the temperature ramp. The heating ramp was set to 10 $K \cdot min^{-1}$ till the temperature was approximately reached. Then the heating rate was set to 5 $K \cdot min^{-1}$ and at last set to 2 $K \cdot min^{-1}$. The heating curve of the newly adjusted program is shown in *Figure.35*. This measurement was conducted without changing the atmosphere so the second peak after the heat up is missing. The temperature change that is produced by the different atmospheres could not be excluded because it is a real signal from the measurement and not caused by the regulators.

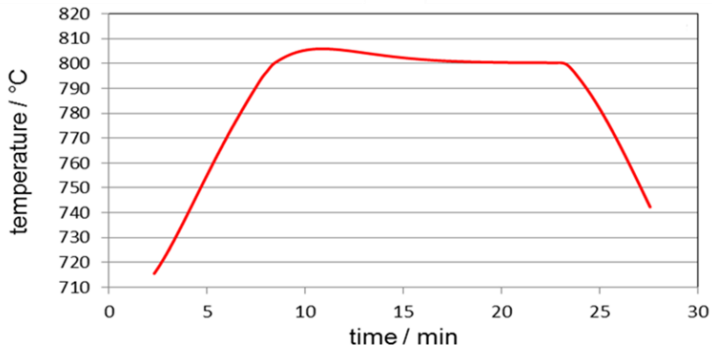

Figure.35: Characteristic behaviour of the STC mode during heating period with segmented temperature ramp.

After these adjustments, the overheating peak was reduced to one third. For the measurements in this work three different temperature programs were developed. They all started with a heating ramp to the desired temperature followed by an isothermal reaction period. In two programs the temperature during the reactions was set constant and in the third the temperature was changed between the single reaction steps. During the heating period, the sample chamber was purged with inert gas. During the reaction periods the reactive gas was diluted with inert gas in a predefined ratio. After every reaction step the measurement chamber was purged with inert gas. The applied temperature programs are listed in *Table.11*.

Table 11: The temperature adjustments of the three measurement programs.

	end of heating ramp	reduction	purge	oxidation	purge
program 1:	600 °C	600 °C	600 °C	600 °C	600 °C
program 2:	750 °C	750 °C	750 °C	750 °C	750 °C
Program 3:	750 °C	750 °C	cooling	600 °C	heating

The gas compositions were varied in some experiments and are listed in the experimental section at every measurement. Some preliminary measurements were done to evaluate the accuracy and the reproducibility of the measurements. The conditions of the preliminary measurements are described for each measurement and can also be found in chapter 4.1.

3.2.3 Troubleshooting of the additional accessory units

For the purpose of the present work the measurement apparatus had to be disassembled and reassembled again. This was done according to the user manual. After the apparatus was built up the first measurements were performed with inert gas N_2 and a reference sample. After this measurements the first tests with reactive gas H_2 were conducted which are shown in chapter 4.1. All these tests showed the expected results. The gas flows were controlled by mass flow controller (MFC-Box, Netzsch) and the steam was generated by a steam generator (a Drop) which was equipped with gas and liquid flow controller (Bronkhorst). All gases were obtained with a purity of 99,999 % (Linde). There have been some artefacts in the measurement curve that were obviously produced by pressure drops and temperature changes. These effects came from the location of the workstation and no solution for these problems was possible. In some cases vibrations also caused artefacts but they were easy to detect and influenced the results only marginally. With the analysis program ‘Proteus analysis’ it was possible to filter the measurement curves and smooth the artefacts. Much more problems occurred during the first test with two reactive gas compositions H_2/N_2 and H_2O/N_2. The measurement showed no discrepancies to the earlier ones till the steam was supplied. The addition of steam caused big challenges in terms of artificial peaks shown in *Figure. 36*.

4 Experimental Results and Discussion

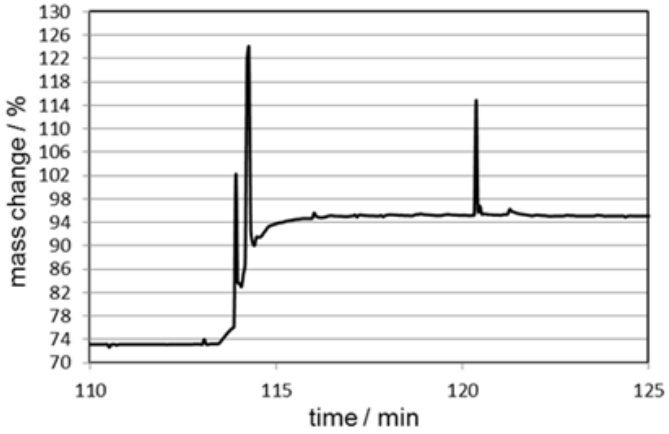

Figure 36: Artificial peaks produced by inhomogeneous steam exhaust flow.

At first it was noticed that water condensed at the outlet of the measurement furnace choking the exhaust. This plugging caused steam accumulation inside the apparatus and was one reason for the peaks during the oxidation. The solution for this problem was to adapt an exhaust heater to the gas outlet. The modified outlet is shown in *Figure. 37*.

Figure 37: The heated exhaust of the furnace.

After this construction the results were better but still not satisfying. After intensive literature research and cooperation with the manufacturers (Netzsch and a Drop) reasons for the unwanted peaks were identified. At first the vaporizer was analyzed and it was pointed out that this kind of vaporizer was not ideal for our application. The system consists of a water reservoir, a liquid and gas flow controller, a direct evaporation unit and a gas/steam mixing unit. The gas flow controller was unnecessary for the steam supply but could adjust the dilution with steam. The problem with this setting was that the direct evaporator consisted of a solid porous material and water was dosed with a liquid flow controller on this material. The wet porous material was heated with heating wires and the steam was transferred to the mixing chamber. Even if no liquid was fed to the evaporator a steam-equilibrium between the direct evaporator and the mixing chamber developed. The reason for this was that there was already a liquid in the evaporator coming from an earlier measurement. Adjusting of the steam-equilibrium was not possible because there was no vent between these two chambers. These setting resulted in a continuous transport of steam to the measurement furnace. The principle setup of the vaporizer is shown in the Figure.38.

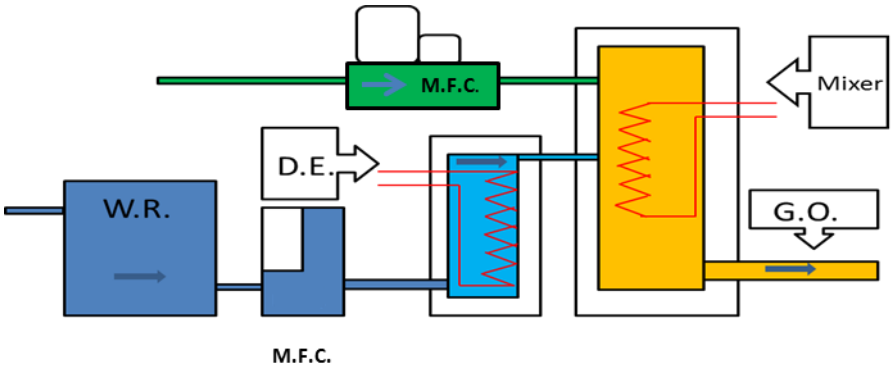

Figure 38: The evaporator unit: W.R. = water reservoir; M.F.C. = Mass Flow Controller; D.E. = direct evaporator; G.O. = gas outlet.

All gases related to the external MFC-box were controlled by magnetic valves. This was not the case for the steam that was supplied by the water vapor generator (WVG)

There was no possibility to insert an extra valve between the direct evaporator and the mixing chamber so another solution was needed. The original installation plan is shown in *Figure. 39*. All involved units are connected with the controlling unit which directly transferred the data to a PC. During the reduction or the purge phase gases were supplied by the external mass flow controller (MFC-box). During the oxidation phase the purge gas was fed through the evaporator (WVG). Therefore the steam controlling unit (SC) switched a vent and applied pressure to the liquid flow controller unit and steam entered the measurement chamber. However, after switching on the steam controlling unit too much water entered the STA. Consequently, no defined steam flow was feasible. This phenomenon is also described in the operating manuals of the vaporizer. It takes several minutes to achieve a constant steam flow.

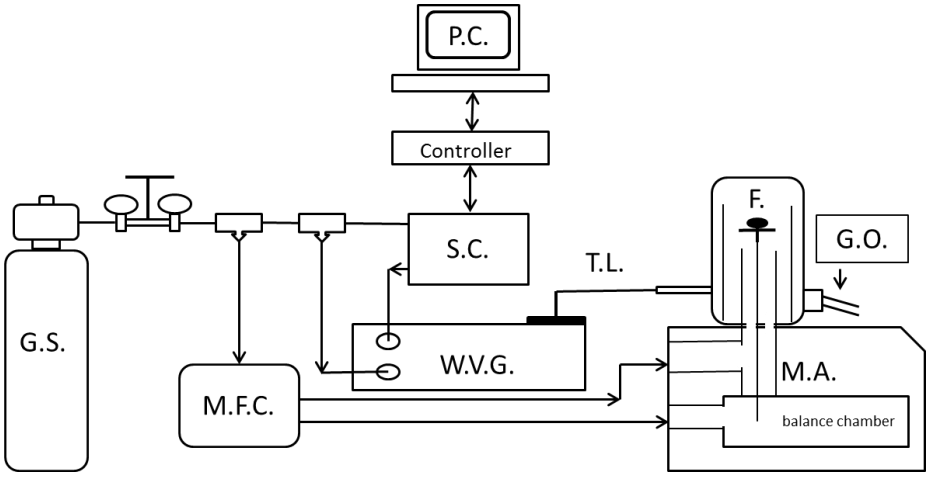

Figure 39: Units involved in STA measurement with steam (G.S. gas supply N_2; M.F.C.-box. external mass flow controller for purge and reducing gases; S.C. steam controller that applied pressure on the MFC of the vaporizer The controller was connected with all other units and commands the steam controller to apply pressure or not; W.V.G. water vapor generator; T.L. heated transfer line; F. furnace with sample (black dot); M.A. measurement apparatus; G.O. gas outlet).

4 Experimental Results and Discussion

To eliminate steam plugging at the exhaust of the STA an adapter between the vaporizer and the measurement apparatus was constructed. The problem of excess water supply after switching on the steam controller was solved by a permanent steam flow. The steam went through a heated pipe into the adapter, passed a vent and was condensed outside the adapter. If steam was required for an oxidation reaction, the vent closed and another vent connected to the transfer line was opened. This construction allowed a constant predefined stream of steam during the whole measurement. The controlling of the vents was realized with a pneumatic 5/2 way valve and a piezo-pressure sensor (Festo). The pressure sensor was attached to the outlet of the steam controlling unit and the 5/2 way valve was connected to a compressed air tank. The vents (Parker) had the adjustment ”normally closed”. The compressed air used to open the vents by the moving piston was sealed gas tight. The mechanism of switching and opening the vents is shown in *Figure.40* and *41*.

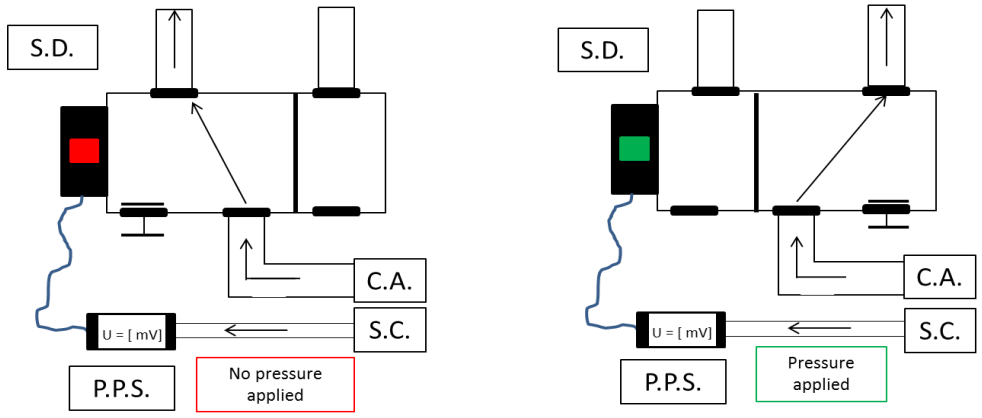

Figure 40: The mechanism of switching pressure from one steam vent to another (S.C. = steam controller; C.A. = compressed air; P.P.S. = piezo-pressure-sensor; S.D. = signal delivery that controls the 5/2 way vent; the blue wire is representing the electric signal junction).

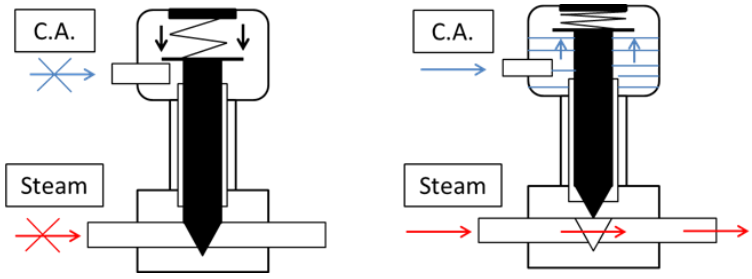

Figure 41: The principle of a (normally closed) steam vent.

The 5/2 way valve always applied pressure to one of the two vents. When the steam controller set no pressure the vent leading to the condenser was opened. When the steam controller set pressure the piezo senor produced an electric signal and relayed this to the 5/2 way vent. Consequently the vent switched according to the way of

pressure delivery and opened the other vent. The vent to the condenser closed at the same time as the vent to the STA opened. The vents and the entire vapor adapter were encapsulated in a metallic box. In *Figure.42* the single parts of the adapter are shown. For the possibility of steam dilution and to avoid the steam to stay in the transfer line a gas line with purge gas was attached to the T after the vent.

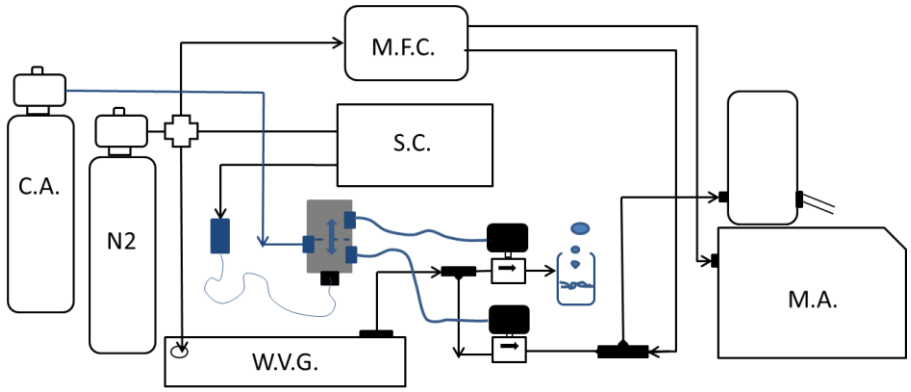

Figure 42: The single parts of the vapor adapter are represented (C.A.: compressed air; MFC: mass flow controller; S.C.: steam controller; W.V.G.: water vapor generator; M.A.: measurement apparatus; the fat blue wires are representing the pneumatic tubes).

Additionally the setting of the six different temperatures was evaluated. With cooperation of the Netzsch company a sufficient working temperature setting for the steam supply without exhaust plugging was achieved. The single thermal units and the temperatures are shown in *Table.12*.

Table 12: Temperature adjustments of the single application parts of the STA

Name:	Vaporizer	Vaporizer Adapter	Transfer Line	Heating Collar	Measurement Apparatus	Exhaust Furnace
Acronym:	V.	V.A.	T.L.	H.C.	M.A.	E.F (G.O.)
Temperature / °C:	200	140	210	230	variable	230

After the modifications the measurement signal during oxidation did not show artificial peaks. To illustrate this a single redox cycle is shown in *Figure.43*.

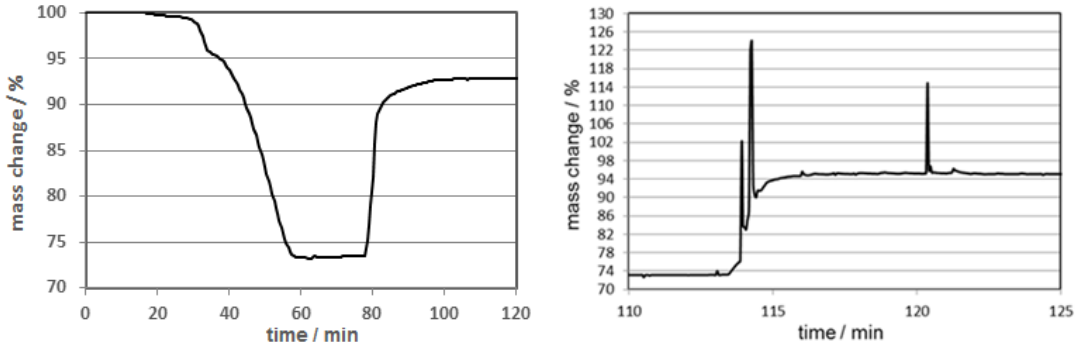

Figure 43: The measurement signal after modifying the steam generator (left). The measurement signal during an oxidation before the installation of the vapor adapter (right).

4 Experimental Results and Discussion

4.1 Elemental analysis

To evaluate the efficiency of the impregnation method and the dry mixing procedure the prepared samples were analyzed at the Institute of Analytical Chemistry and Food Chemistry of Graz University of Technology. The efficiency describes the amount of measured aluminium support to the amount that was meant to be coated on the iron. ICPMS (inductive coupled plasma mass spectroscopy) was used for elemental analysis. The results were provided as the aluminium content in mg per g of the sample. The results of the elemental analysis are shown in *Table.13*.

Table 13: Results of the element analysis and the comparison of the impregnation efficiency.

Sample	desired concentration Al_2O_3 / %	measured concentration / $_{mg}Al \cdot g^{-1}{}_{sample}$	calculated from measurement / %
5 % Al_2O_3	5	15.9 ± 0.5	3.02
10 % Al_2O_3	10	37 ± 1	6.98
20 % Al_2O_3	20	114 ± 3	21.72
V7	10	50 ± 1	9.44

Table.13 shows that the wet impregnation method was not as efficient as the dry mixing method of the V7 sample. All wet impregnated samples show a small difference to the desired aluminium loading. The impregnated sample that worked best was the 20 % sample with a deviation of 1.72 % to the desired loading. The one with the weakest conformance was the 10 % sample with a deviation of 3.02 %.

The mass change, which is directly correlated to the oxygen insertion and release, was observed and evaluated. A series of preliminary measurements was done to confirm that the apparatus is performing accurately. Derived from these analytical data the theoretical mass changes during the redox cycles were calculated and compared with the originally intended ones. The comparisons are shown in *Table.14* and the results are in agreement with the calculations done before.

Table 14: The comparison of the theoretical mass changes from the calculated additive concentration and the measured ones

Sample :	Calculated mass change between magnetite and iron [%] :	Corrected mass change with respect to the ICPMS measurements [%] :
Pure:	26.7	
5 %:	25.1	25.7
10 %:	23.5	24.4
20 %:	20.3	19.7
V7:	23.5	23.6

This accordance describes the change in mass with respect to the additive concentration in the sample. The reaction equation without support is represented in *Equation.45*. The calculation without support is shown in *Table.15* and the calculation with 10 % aluminum support is shown in *Table.16*.

$$3\ Fe_2O_3 \rightarrow 2\ Fe_3O_4 \leftrightarrow 6\ FeO \leftrightarrow 6\ Fe \quad (45)$$

It should be noted that the calculation with support was done with respect to the hercynite formation in the wustite state and it was assumed that the hercynite was able to get reduced to Fe and Al_2O_3 but stayed stable during the oxidation. So the mass change with support was calculated between the reduced sample (Fe + Al_2O_3) and the oxidized form of the sample (Fe_3O_4 + $FeOAl_2O_3$). In *Table.16* the transitions during reduction are only related to the first reduction.

Table 15: Mass change calculation of an iron oxide sample without support.

stoichiometric factor	species	MW/g·mol^{-1}	mol	mass/g	percent/%	sample transition	difference/%
3	Fe_2O_3	159,6	0,0062	1	100	haematite → magnetite	3,34
2	Fe_3O_4	231,4	0,0041	0,96	96,65	magnetite → wustite	6,68
6	FeO	71,8	0,0125	0,89	89,97	wustite → iron	20,05
6	Fe	55,8	0,0125	0,69	69,92	sum:	30,07

Table 16: Mass change calculation of a sample with 10 wt % aluminium oxide support

Species	MW/g·mol^{-1}	mol $Fe_{bulk}/Al_{support}$	mass	percent/%	sample transition	difference/ %
Fe_2O_3 + Al_2O_3	159,6 + 102	0,00563 + 0,00098	0,9 + 0,1	100	haematite + corundum → magnetite + corundum (during reduction) magnetite + hercynite → magnetite + hercynite (during oxidation)	3
Fe_3O_4 + $FeOAl_2O_3$	231,4 + 173,8	0,00343 + 0,00098	0,79 + 0,17	96,47	magnetite + corundum → wustite + hercynite (during reduction) wustite + hercynite → magnetite + hercynite (during oxidation)	6,01
FeO + $FeOAl_2O_3$	71,8 + 173,8	0,01029 + 0,00098	0,73 + 0,17	90,97	wustite + hercynite → iron + corundum	18,04
Fe + Al_2O_3	55,8 + 102	0,01127 + 0,00098	0,62 + 0,1	72,93	sum:	27,07

4.2 Preliminary measurements

To evaluate the gas uplift effect of nitrogen during a heating ramp a blank measurement was conducted. The empty TG sample carrier was placed into the furnace and a temperature profile was programmed. The program started with an isothermal phase at 30 °C for 20 minutes. The following heating ramp was set to 700 °C with a heating rate of 10 $K \cdot min^{-1}$. The nitrogen flow was set to 30 $ml \cdot min^{-1}$. *Figure.44* shows the result of the blank measurement. In the initial isothermal phase the gas uplift affected the sample carrier to show an apparent decrease of mass. This initial decrease is the result of the temperature change inside the oven. During the heating ramp a mass increase is visible and is explained by the change of gas density and the correlated different uplift effect. There is one distinct peak in the mass curve that came from a pressure drop in the laboratory. The gas uplift effect was considered to be negligible.

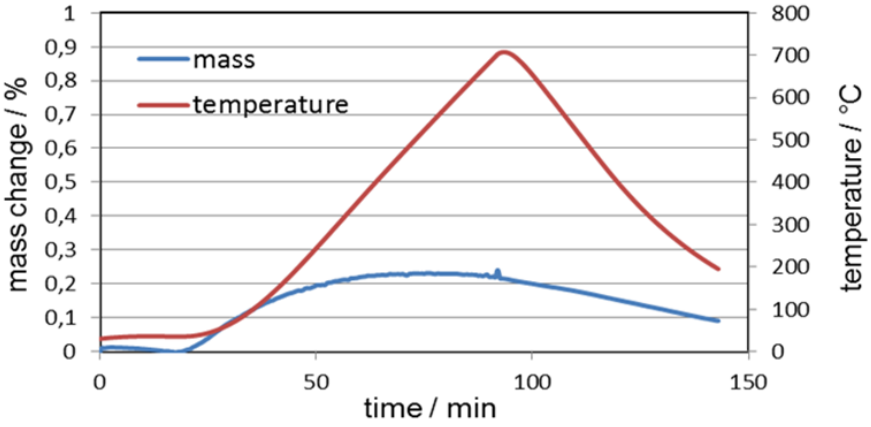

Figure 44: Blank measurement with a empty TG sample carrier during an heating ramp.

The first measurement was done to see the maximum amount of mass decrease that can be achieved with pure sponge iron powder as starting material. Therefore the sample was completely oxidized in an oven at 900 °C with air. The sample mass was about 50 mg and the gas flows were set to 60 $ml \cdot min^{-1}$ N_2 and 30 $ml \cdot min^{-1}$ H_2 immediately at the beginning. The heating ramp was set to 10 $K \cdot min^{-1}$. The measurement is shown in *Figure.45*. During this measurement the segment temperature control was deselected and the final temperature was set to 1000 °C. The TG curve shows no significant change up to a temperature of 320 °C. At 320 °C the first mass change occurred and reached a plateau at 370 °C. This mass change shows the transformation from haematite to magnetite. The theoretically calculated mass change from haematite to magnetite was 3.3 wt % and the measured one was 4.1 wt %. The difference of theoretical and measured value is 0.76 % and can be explained by the gas uplift effect. The plateau is explained in the literature by a reduction delay caused from the lattice change of the iron oxide from a

hexagonal/trigonal to a cubic lattice [74]. The change from magnetite to wustite is not observable in the TG curve. The reason for this is that the reaction takes place below 570 °C and wustite is only stable above this temperature. A constant mass change from 370 °C to 600 °C is observable. Above this temperature the mass decrease is very slow and is explained by diffusion processes from oxygen through the already produced iron. The final mass was about 70 % of the initial sample. This change in mass is in good agreement with theory (30 wt %).

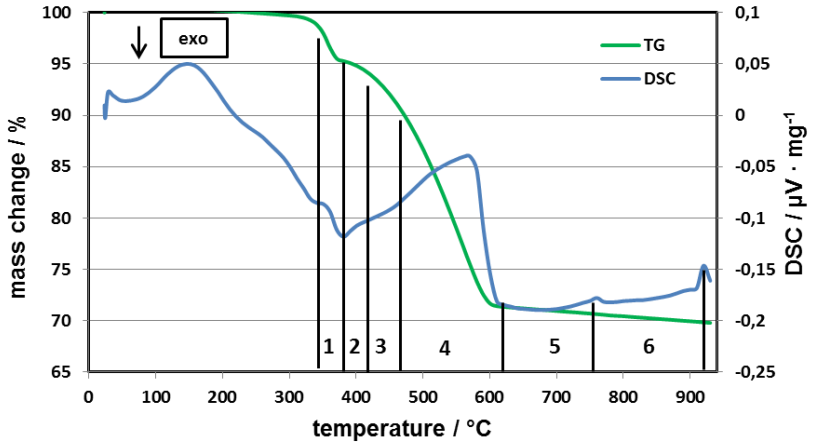

Figure 45: The TG and DSC signal from the measurement of the oxidized sponge iron powder without aluminium oxide.

The DSC signal was not calibrated before because the main focus of this work was set on the mass change of the contact mass. After consultation with Netzsch company it was possible to explain all peaks of the DSC curve. The first peaks are shown in *Figure. 46* and the correlation between the DSC signal and the temperature change are pointed out with double arrows. The first peak is produced by the apparatus and is called the starter or onset swing effect. This effect comes from the temperature conditioning of the sample carrier, the sample, the gases and the oven. The second one is related to the start of the heating ramp and the ensuring temperature change. The third one is related to the change of the heating rate.

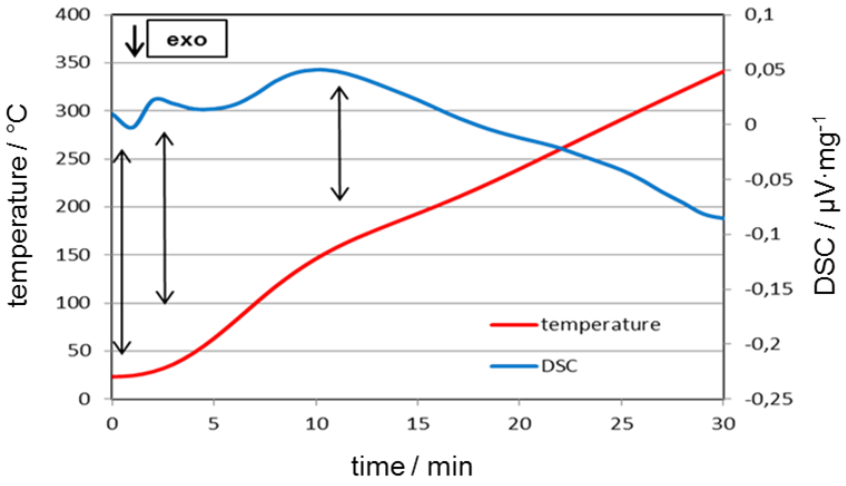

Figure 46: The magnification of the first peaks in the iron reduction measurement

After the third peak the curve falls continuously due to heat uptake of the sample. The other peaks are pointed out in *Figure.45*. The first peak (1) selected in *Figure.45* is produced by the reduction reaction from haematite to magnetite and is endothermic. After this peak there is a change in the DSC curve that came from the temperature assimilation of the sample (2). In the third section (3) that is selected the curve rises and is indicating an endothermic process. The second and third regions are correlated with the transformation from magnetite to wustite. In the fourth section (4) a big endothermic peak occurs that is produced by the final reduction from magnetite / wustite to iron. Beyond the fourth section most of the sample consisted of metallic iron. The peak at the end of the fifth area shows the change from the ferromagnetic to paramagnetic iron. The Curie temperature of iron is 766 °C. The last peak indicates the change from α- iron to γ- iron at around 910 °C.

4.3 Multi cycle measurements

Before every multi cycle measurement, the desired sample was weighted on an analytical lab balance. Then it was transferred on the TG sample carrier and dispersed with a flat spatula and finally with a spoon to obtain a thin and well distributed sample. Before the measurement started a purge phase of about 10 minutes with 100 ml·min^{-1} N_2 was conducted to avoid reactive gases inside the sample room. In the first measurement shown some details concerning the shape of the measured curve are explained which are also valid for all other measurements.

4.3.1 Multi cycle measurement:

stabilized 5 % sample @ 600 °C / 200 mg:

Table 17: Reaction times and gas flows of the redox cycle measurement.

Reaction phase	Time / min	N_2 / ml·min^{-1}	H_2 / ml·min^{-1}	H_2O / ml·min^{-1}
Reduction	20	20	80	
Purge	5	50		
Oxidation	20	50		80

Figure.47 shows the complete cycling experiment of the 5 % sample at 600 °C. The initial signal in the measurement disappears because of the uplift effect during the heating ramp and the scaling of the y axes. The first reduction curve of the measurement falls from haematite to the iron mass level. The end of this slope seems not to develop a constant value indicating that the reaction was not completed but later evaluation showed that the reaction indeed came to an end. The signal after the reduction shows an edge which is produced by switching the gas supply from H_2/N_2 to just N_2. This switching caused an apparent mass increase that was around 2 %. The oxidation reaction was conducted after the purge phase. Some little peaks are observable at the plateau during the oxidation which came from vibrations and

pressure drops in the laboratory. During the oxidation the mass signal developed a constant value in all cycles. This behaviour indicated a sufficient reaction time and steam feed.

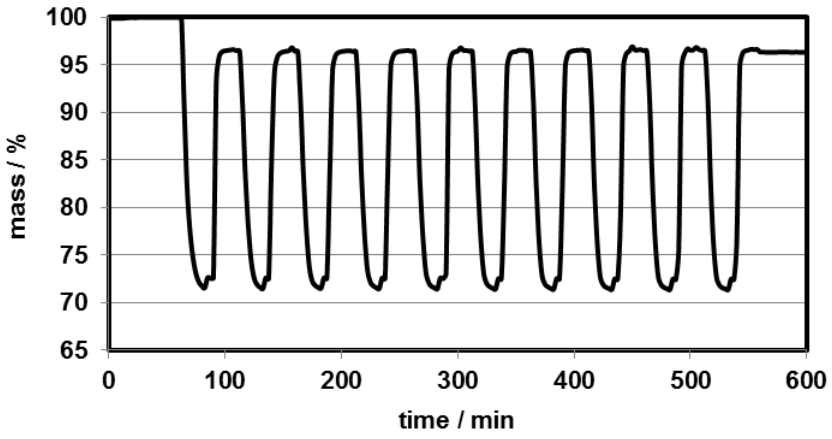

Figure 47: The TG measurement of the 5 % sample at 600 °C over ten redox cycle.

To evaluate the measurement the analysis was done in two ways and is shown in *Figure.48 and 49. Figure.48* shows a bar diagram with the mass changes related to the three different gas atmospheres during the measurement and the magnification of the top of the bars. The different gas atmospheres in the bar diagram are marked that way that red ist representig the reduction, blue the oxidation and green the pugre phase. *Figure.49* shows four single curves of the reduction and oxidation to evaluate the change in the reaction kinetic over consecutive cycles.The mass change of the first reduction is not used for the interpretation of the long time stability.The mass changes that are used are related to the mass difference between the purge phases. This was done because it was assumed that the evalution just becomes feasible if the mass changes are compared in the same gas atmosphere.

The mass changes started with 23.94 % in the first cycle and became 23.95 % in the second. The next two cycles were very similar and about 23.94 %. After the fourth cycle the mass change reached a value of 24 %. The following cycles did not change their value and were constant at 24.6 %. The theoretically possible value for the mass change was evaluated to be 25.1 %. This level was never achieved but the measured results and the theoretically differ by just 0.5 %. The entire performance of the sample was stable and no agglomeration or any other degradation processes were observed.

4 Experimental Results and Discussion

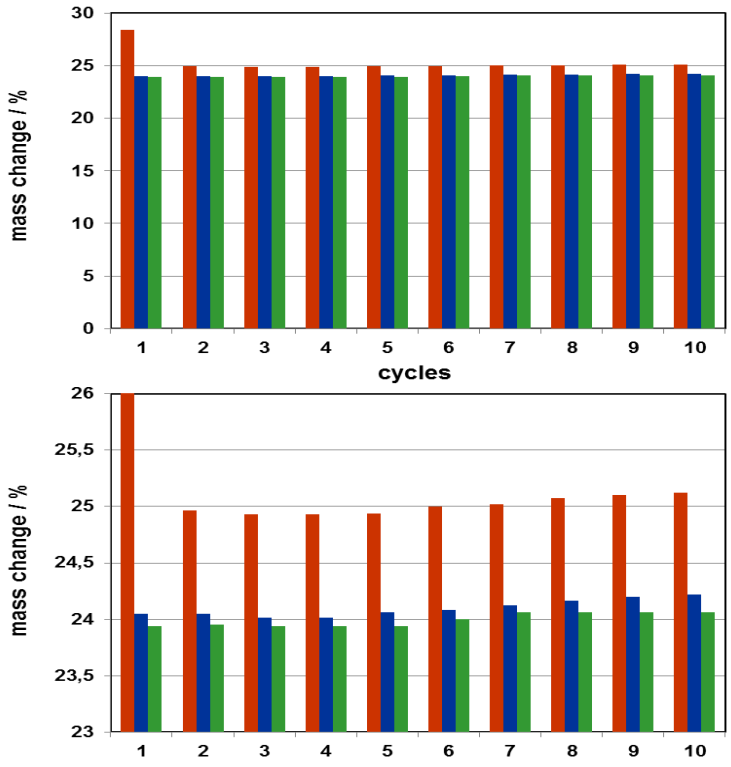

Figure 48: The bar diagram with the mass changes in each atmosphere / reaction and the magnification. The green bars represent the mass exchange during the purge phases.

Figure.49 shows four reductions on the left side and four oxidations at the right side. The reductions showed a significant trend in terms of changing the shape of the measurement curve. The shape of the second reduction was smooth and became sharper over the consecutive cycles. It is pointed out that they all reached the same mass level and no decrease of mass change was observed. The oxidations do not show such a significant trend but they also reached the same mass level at the end of the measurement.

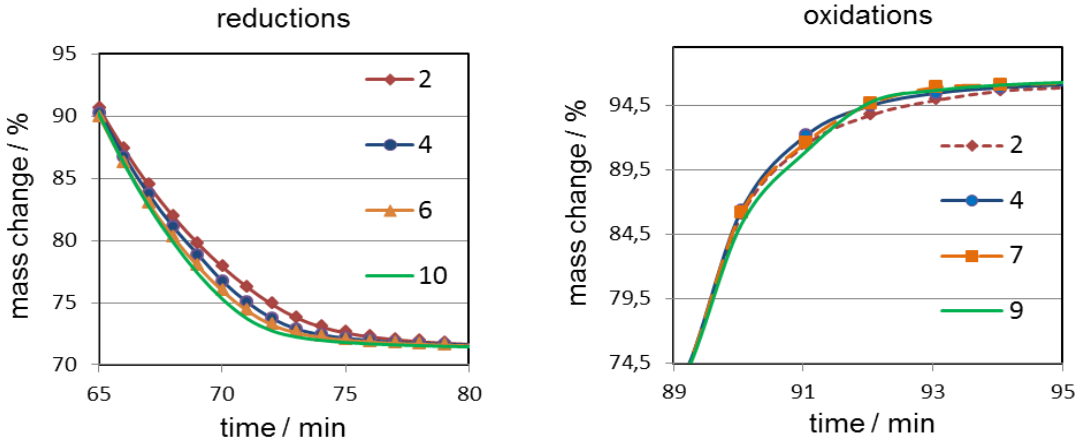

Figure 39: The single reductions (left) and the selected oxidations (right).

Multi cycle measurement:

stabilized 5 % sample @ 600 °C / 200 mg Nr.2:

Table 18: Reaction times and gas flows of the redox cycle measurement.

Reaction phase	time / min	N_2 / ml·min^{-1}	H_2 / ml·min^{-1}	H_2O / ml·min^{-1}
Reduction	60	90	60	
Purge	10	30		
Oxidation	30	30		80

A second measurement with the 5 % sample was performed to evaluate the reproducibility of the measurement. *Figure.50* shows the whole measurement with enhanced gas flows and reaction times. The mass already decreased before the reduction phase. The mass loss before the reduction reaction was around 2 %. This decrease was not totally understood. The mass change stayed constant over the following cycles. The first reduction led to a mass level of 72 % related to the initial weight. This reduction seemed to be completed. That shows a mass loss of 28 % from haematite to iron and is just 0.5 % lower than the theoretical value. The consecutive oxidations were similar to the one in the first measurement in terms of reaction time and constant mass level that was reached. To evaluate this measurement the same technique was used as before.

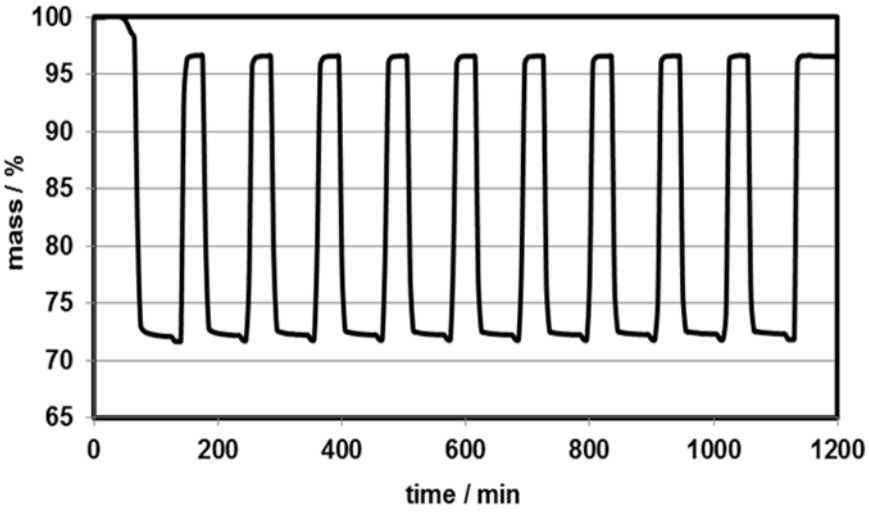

Figure 50: The second measurement of the 5 % sample at 600 °C.

Figure.51 shows a bar diagram of the mass changes for each atmosphere. The first cycle showed a mass change of 24.9 %. The second one was a bit higher with 24.94 % followed by two identical cycles with 24.92 %. The next three cycles showed a slight decrease from 24.86 % to 24.78 % and stayed constant over the following cycles. In this measurement series the measured values are closer to the theoretical value than they have been for the first one. During this series the sample showed

minimal difference in mass change over the first 6 cycles and was constant afterwards. This behaviour is observable in the magnification of the top of the bars.

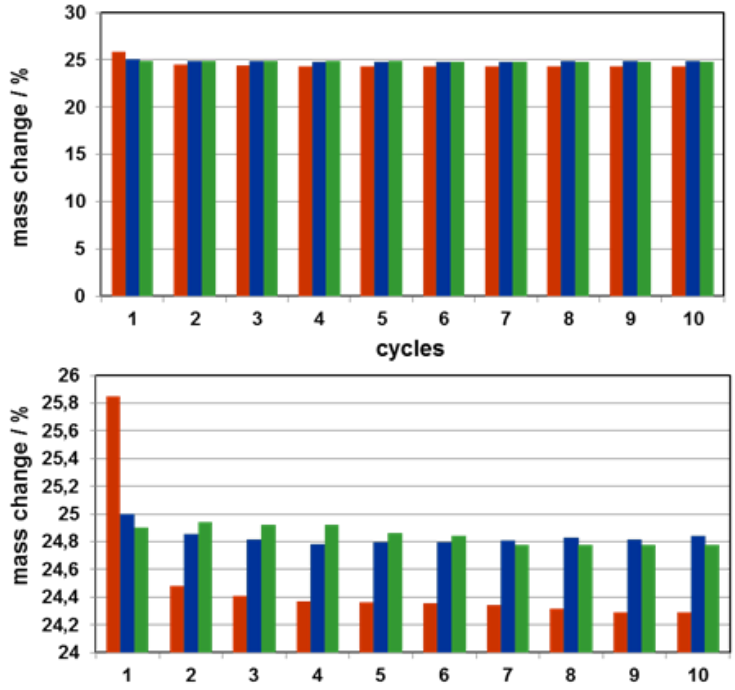

Figure 51: The bar diagram of the second 5 % measurement and the magnification.

Figure.52 shows four single reductions on the left and four single oxidations at the right side. The reductions showed a significant trend that was correlated with the first measurement. The reductions are getting faster over the ten cycles and the mass change was constant. The oxidations had the same form as the previous ones. It is pointed out that the shapes of the eighth and tenth oxidation in *Figure.52* look very similar to the analogous curves 7 and 9 in *Figure.49* but with a more distinct kink in the curve.

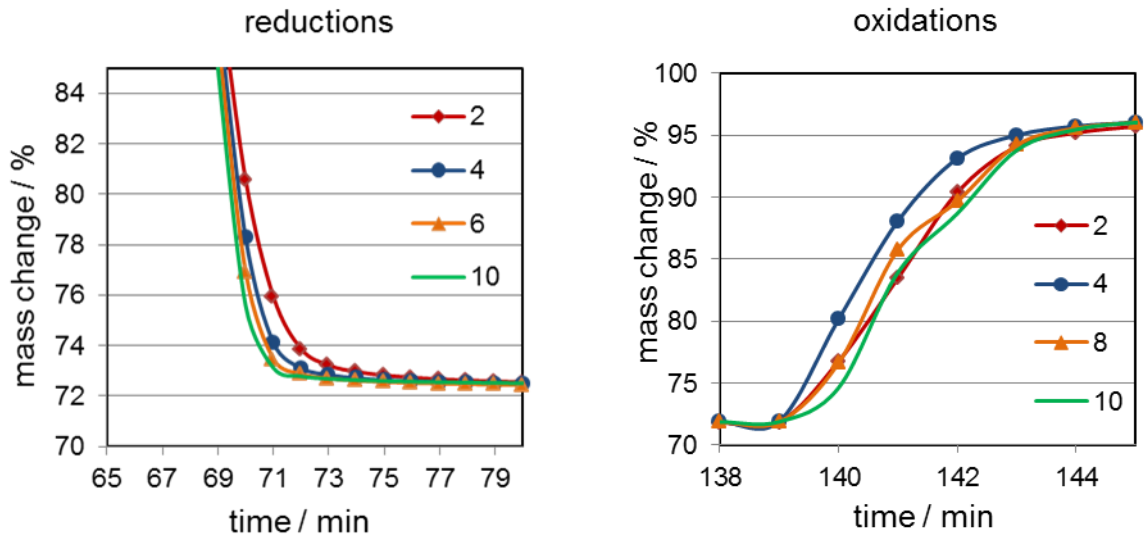

Figure 52: The single reductions which show a distinct trend (left) and the single oxidations (right).

Discussion

Both 5 % samples showed a good performance during the entire measurement. The little discrepancies between the two measurements are explained by the different gas flows used. The reductions from the first series showed a smooth convergence to the final mass level. The reductions in the second series showed a faster convergence to the final mass level. This behaviour is assumed to be caused by the thicker iron layer that is produced in the more reductive atmosphere in the first measurement. The comparison of the oxidations did not show such a distinct trend and this observation was attributed to the same vapor adjustments in both measurements. The kinks that were observed during the later oxidations are probably caused by structural changes of the sample.

4.3.2 Multi cycle measurement: stabilized 5 % sample @ 750 °C / 200 mg:

Table 19: Reaction times and gas flows of the redox cycle measurement.

Reaction phase	time / min	N_2 / ml·min^{-1}	H_2 / ml·min^{-1}	H_2O / ml·min^{-1}
Reduction	90	90	60	
Purge	5	30		
Oxidation	35	30		80

In *Figure.53* the measurement with the 5 % sample at 750 °C is shown. The initial signal shows no mass change during the heating ramp. This is a good sign that the atmosphere was sufficiently inert and no other impurities have been present in the sample. The first reduction reached a constant plateau after a parabolic period of mass change. The purge phase is visible and shows an edge like in the first measurement. The oxidation reached a mass level of 96.8 % and the difference between the initial mass and the mass after the first oxidation fits theory well. The oxidations barely reached a constant value but it was considered that the reaction time was sufficient. This assumption was made because the last oxidation was programmed to be longer than the others and the final mass level in the tenth oxidation is similar to the other.

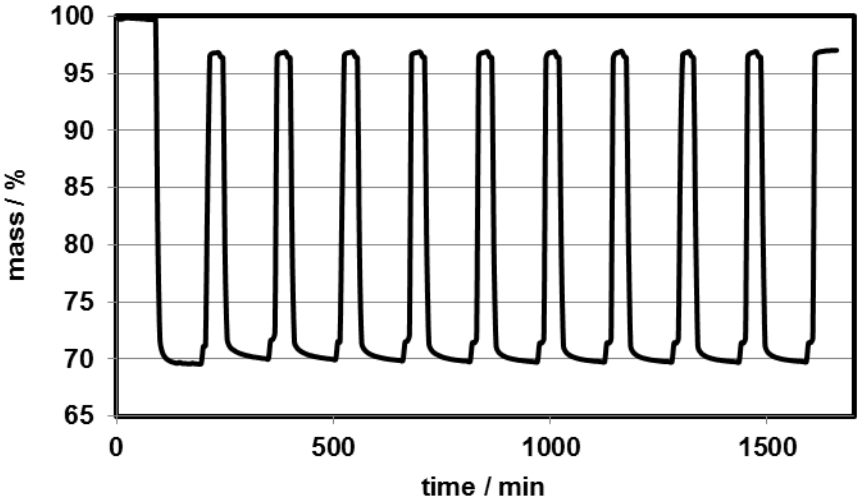

Figure 53: The measurement of the 5 % sample at 750 °C.

The evaluation of the measurement was done as before. In *Figure.56* the bar diagrams according to the different gas atmospheres are shown. The mass change during the first cycle was 25.25 % with just a difference of 0.5 % to the theoretical value. The mass change in the second and third cycle was a little bit lower with 24.82 % and 24.84 %. The mass change in the following cycles was rising continuously up to 25.1 % in the tenth cycle. The results are represented in the bar diagram *Figure.54*.

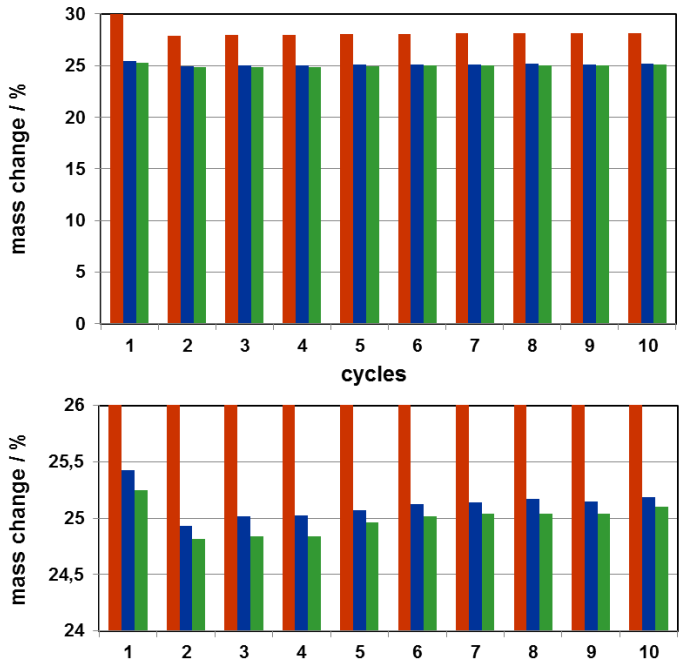

Figure 54: The bar diagrams with the magnification of the tops of the bars. The green bars are representing the mass exchange during the purge phases.

Figure.55 shows four curves of the reduction and the oxidation. The reductions reached a lower weight value in the latter cycles. It has to be pointed out that after the first reduction the following ones reached no defined level. This was an indication that the reaction time was not long enough. The oxidations showed no kinks and there was no distinct trend observable. Overall the performance of the sample was good and no decrease in mass exchange was detected. Because no constant mass level was reached during the reduction a second measurement was done.

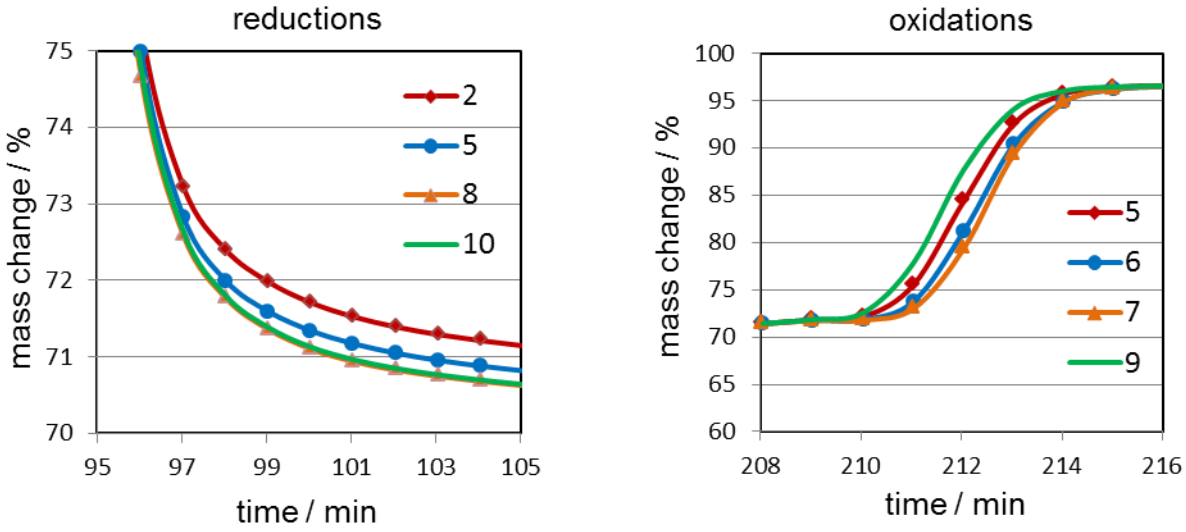

Figure 55: The selected reductions (left) and the oxidations (right).

Multi cycle measurement:

stabilized 5 % sample @ 750 °C / 200 mg Nr.2:

Table 20: Reaction times and gas flows of the redox cycle measurement.

Reaction phase	time / min	N_2 / ml·min^{-1}	H_2 / ml·min^{-1}	H_2O / ml·min^{-1}
Reduction	115	20	80	
Purge	10	100		
oxidation	30	20		80

To evaluate the first 5 % 750°C measurement a second measurement was conducted. The reaction times were enhanced and the gas flows were changed to a more reducing atmosphere. During the oxidations the flow of the purge gas was reduced to have more steam inside the sample chamber and a more reactive atmosphere. *Figure.56* shows the complete measurement of the 5 % sample at 750 °C. In this measurement the reductions seemed to complete. The edge after the reduction was bigger compared to the other measurements and is explained by the increase of the gas flow during the purge phase. The purge phase showed a constant mass level and the following oxidations reached a constant value.

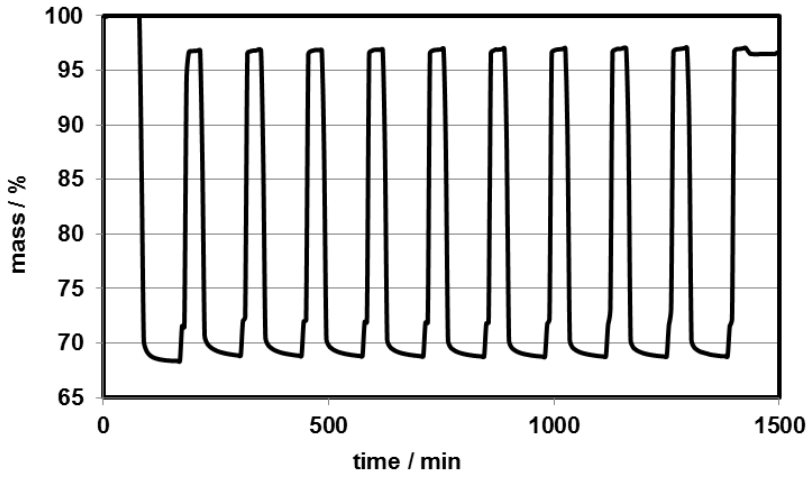

Figure 56: The measurement of the 5 % sample at 750 °C with new adjustments.

The usual evaluation was done and the results are shown in *Figure.57* and *Figure.58*. The mass exchange decreased up to the third cycle and increased afterwards again. After the fifth cycle the mass exchange was constant. The average mass exchange was 24.95 %.

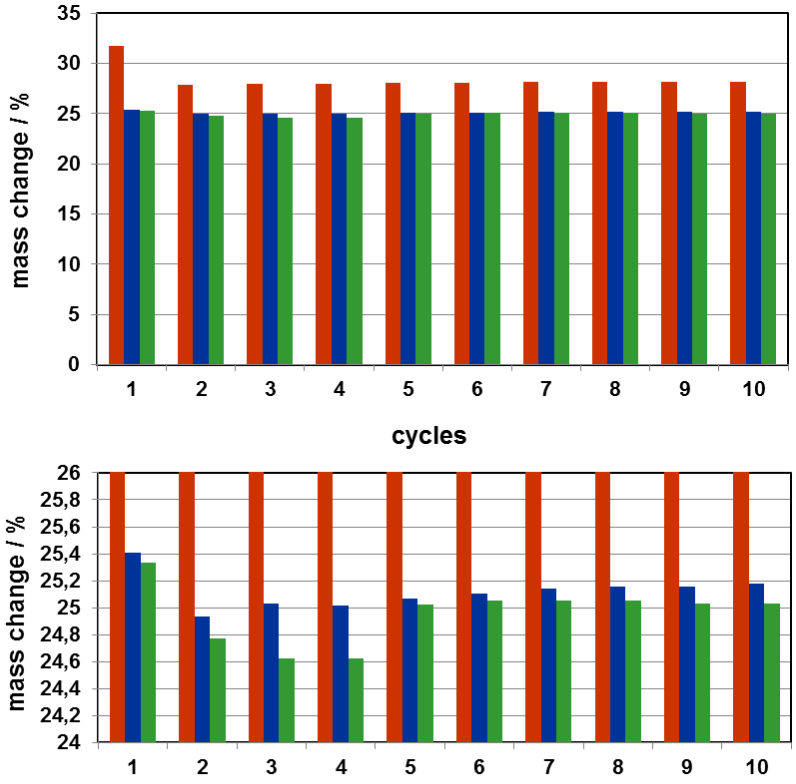

Figure 57: The bar diagram of the 5 % sample at 750 °C with magnification of the bar ends.

In *Figure.58* single reductions and oxidations are shown. The reduction curves tend to a faster kinetic with successive redox cycling of the sample. The second oxidation showed a kink that was also observed in a previous measurement and the kinetic also seems to accelerate.

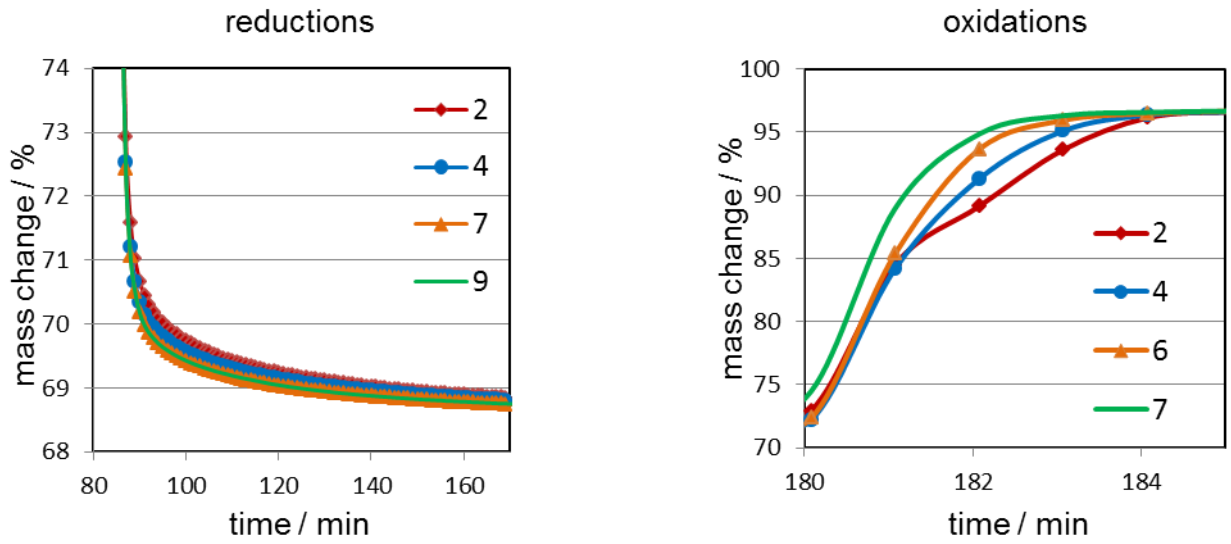

Figure 58: The reductions tend to a faster kinetic (left) and the oxidations which change their shape (right).

Discussion:

Both measurment series showed no constant mass level after the reductions. The shape of the reductions showed the same behaviour as the 600 °C series. In all cases the oxidations had enough time and the amount of steam was sufficient so the oxidations always reached a constant mass level.The mean mass change during ten cycles was 25 % and very close to the theoretical value. The first measurement series showed a 0.5 % lower mass exchange but the overall performance was stable.

4.3.3 Multi cycle measurement: stabilized 5 % sample @ Dynamic conditions / 200 mg:

Table 21: Reaction times and gas flows of the redox cycle measurement.

Reaction phase	time / min	N_2 / ml·min^{-1}	H_2 / ml·min^{-1}	H_2O / ml·min^{-1}
Reduction	20	20	80	
Purge	15/10	50		
oxiation	20	50		80

This measurement was the first one with dynamic temperature adjustments. The purge phases had two time adjustments. The cooling period lasted 15 minutes and the heating after the oxidation took 10 minutes. However this measurement was in the main focus of this work and showed a very interesting behaviour of the sample. The complete measurement is shown in *Figure.59*. The initial signal is not visible and the first reduction did not develop a constant value. The first oxidation did not reach a constant value. An interesting peculiarity was that after the oxidation the mass still rose till the reduction started again. This mass increase during the purge phase is explained in two ways. The first one is the temperature rise during the purge phase that leads to an artificial mass increase. The second and more likely reason was that there was still some steam inside the sample room that slowly reacted further with the residual iron.

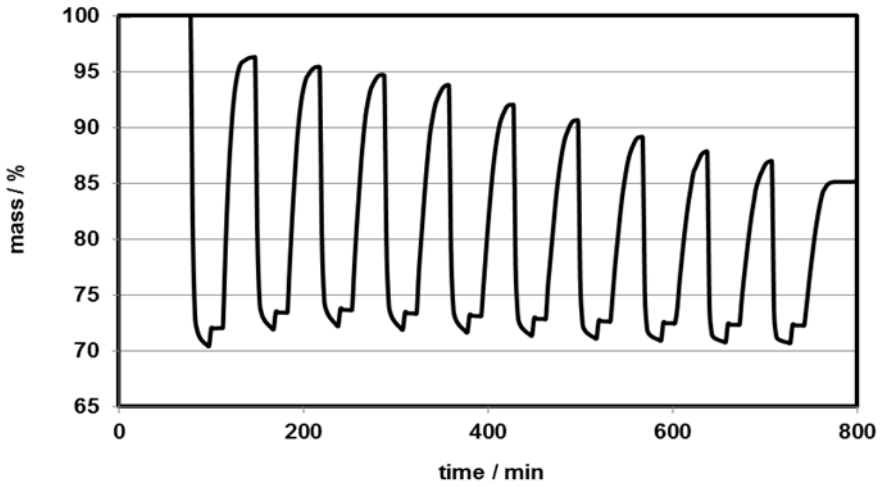

Figure 59: The consecutive mass decrease during a dynamic measurement.

The diagram in *Figure.60* shows the weak stability of the sample under the dynamic conditions. The short reduction time was meant to favour the oxidation. This was assumed because a not totally reduced sample should have a higher porosity than the fully reduced one and would easily allow the steam to get access to the sample pores. Never the less the first oxidation showed a good performance and the second one already had a decrease in the oxygen uptake capability.

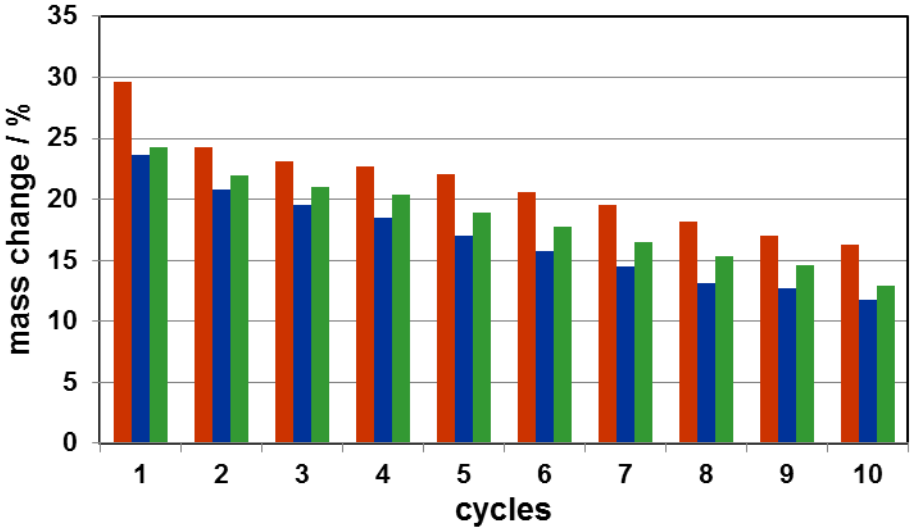

Figure 60: The bar diagram of the 5 % sample during the dynamic measurement without magnification.

After the first cycle the loss of reactive sample became significant. A continuous declension of mass exchange is visible over the following cycles. The first cycle had a mass change from 24.2 % and the tenth cycle had only a mass exchange ability of 11.3 %. The capacity decrease over ten cycles was 12.9 %. The trend lines that are shown in *Figure.61* in the dot plot diagram show an almost linear decrease in the mass exchange.

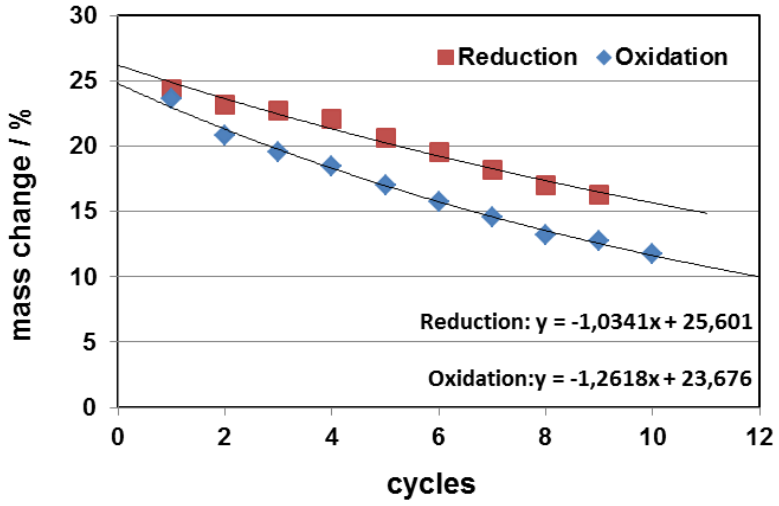

Figure 61: The almost linear decrease of the mass exchange correlated to the cycle number.

The single reductions are represented in *Figure.62* on the left side. They show a faster mass decrease from cycle to cycle and the reactions start from different mass values. These different starting points enable the reaction to proceed the same time in every reduction reaction but the amount of oxygen that has to be removed from the oxide becomes smaller with each cycle. This situation explains the apparent faster kinetics of the later reductions. The oxidations showed a slower kinetic compared to the reduction and did not reach the desired mass level.

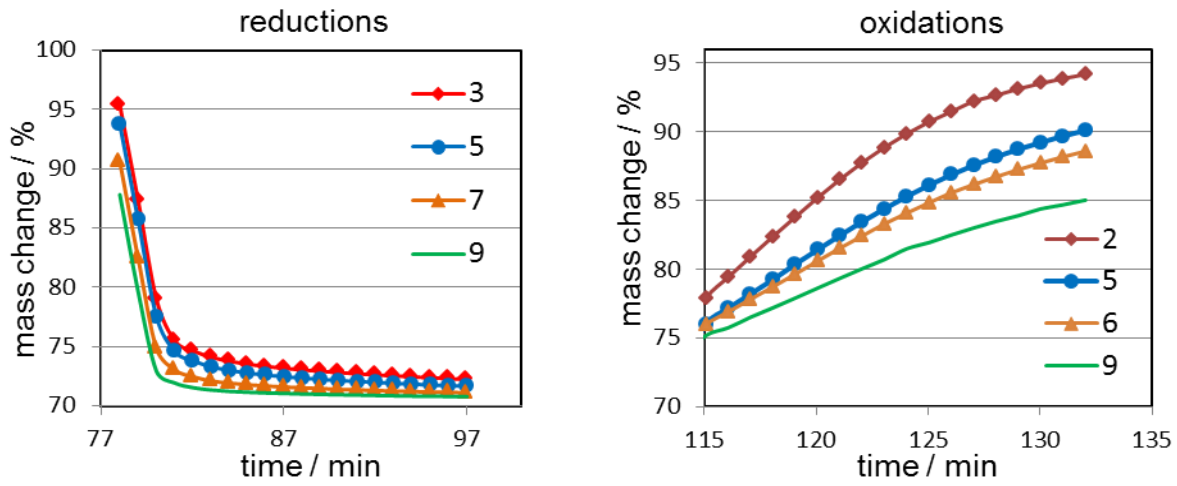

Figure 62: The selected reductions with different starting points (left) and the selected oxidations with different final mass levels (right).

Discussion:

The first two reductions did not reach a constant value but the seventh and ninth reduction did. The ninth reduction shows a kink in the shape that was observed the first time. The ninth reduction developed a constant value and so it was assumed that the reaction was finished. The kink in the ninth reduction can be attributed to the breakdown of the hercynite layer. The oxidations show a clear trend in this measurement. They seem to have a slow reaction kinetic and the shape of the oxidation curves became smoother in the later cycles. It was assumed that the reactive sites of the sample were blocked from the reaction. The slow oxidation kinetic is explained by the dense iron layer that is produced during reduction.

4.3.4 Multi cycle measurement: stabilized 10 % sample @ 600 °C:

Table 22: Reaction times and gas flows of the redox cycle measurement.

Reaction phase	time / min	N_2 / ml·min^{-1}	H_2 / ml·min^{-1}	H_2O / ml·min^{-1}
Reduction	90	90	60	
Purge	5	30		
Oxidation	35	30		80

The measurement is represented in *Figure.63* and shows the behaviour of the 10 % sample. The first reduction did not develop a constant value and reached a mass level of 72 % which was 1 % lower than the theoretical value. The following reductions showed a faster mass decrease and ended at the same value. The purge phases showed no anomalies and the oxidations reached the same mass in each cycle.

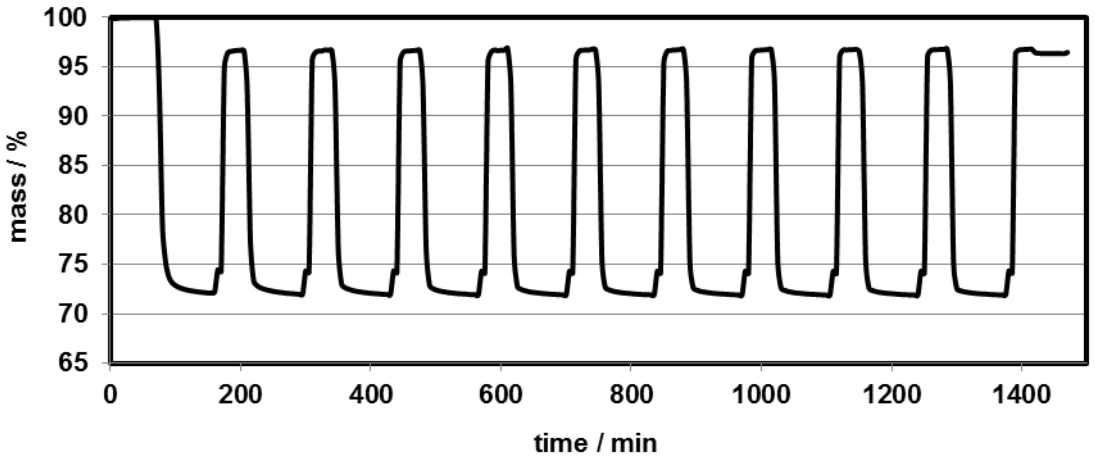

Figure 63: The isothermal measurement of ten redox cycles with a 10 % supported sample at 600 °C.

In the bar diagram in *Figure.64* it is notable that the sample had a good performance in terms of stability. In the magnification of the bar tops the trend of the mass exchange capability is visible. The oxygen capability developed from 22.2 % to 22.5 % in the tenth cycle. This denotes a capability enhancement of 0.3 % over ten cycles. The theoretical maximal value for the capability was calculated to be 24.47 % and a deviation of around 2 % was observed. It was assumed that an inhomogeneous distributed sample has been the reason for the deviation. In the first cycles the reduction definitely did not reach completion. The following cycles achieved a more reduced state than the first one.

4 Experimental Results and Discussion

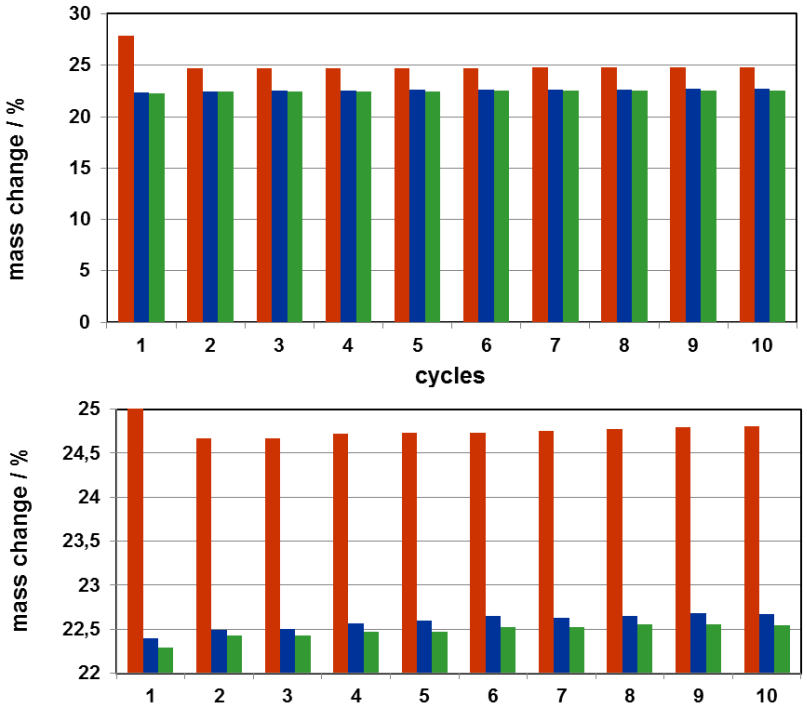

Figure 64: The bar diagram of 10 % sample at 600 °C with the magnification of the bar ends.

The reductions in *Figure.65* show that the later reductions lead to a lower mass level and that a constant value was reached. It is also visible that the later reactions were faster than the earlier ones. The oxidations on the right side did not show any distinct trend.

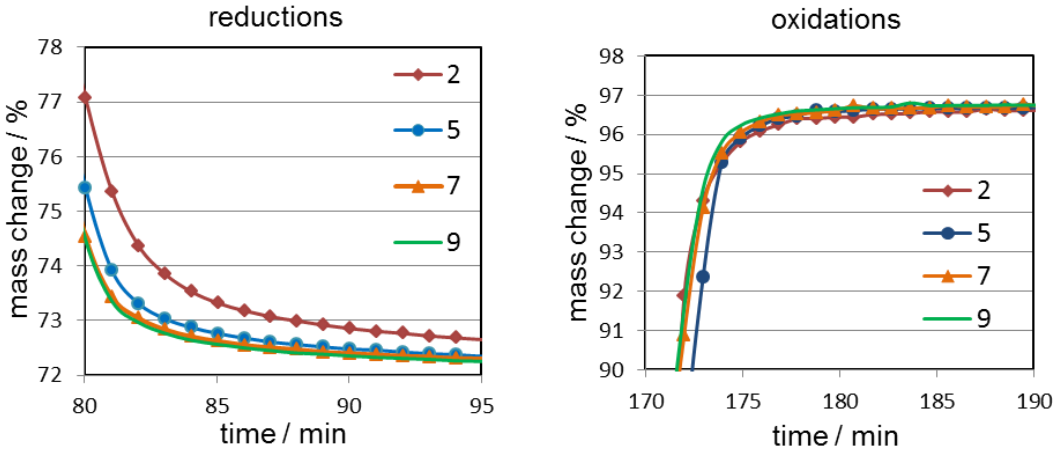

Figure 65: The reduction curves of the 10 % sample show a faster kinetic in the latter cycles (left) and the oxidations do not show any trend (right).

Discussion:

This measurement seemed to be similar to the 5 % sample. The mass exchange was below the one of the 5 % series and was about 2 % lower. The slow kinetics at the end of the reduction can be explained by an oxygen diffusion barrier caused by the aluminium oxide. It is also known that hercynite is reduced only under extreme conditions and that the hercynite first has to be reduced to release the aluminium oxide.

4.3.5 Multi cycle measurement: stabilized 10 % sample @ 750 °C:

Table 23: Reaction times and gas flows of the redox cycle measurement.

Reaction phase	time / min	N_2 / ml·min^{-1}	H_2 / ml·min^{-1}	H_2O / ml·min^{-1}
Reduction	90	90	60	
Purge	5	30		
oxiation	35	30		80

The measurement of the 10 % sample at 750 °C is represented in *Figure.66*. The sample showed a constant performance over the ten cycles. The first reduction reached a mass level of 70.5 %. This mass decrease was bigger than the calculated one. The purge phase showed no anomalies and the first oxidation ended at a constant mass at 96.8 %. The mean value of the mass exchange was 23.6 % and had a deviation of less than 1 % compared to the calculated maximal value of 24.4 %.

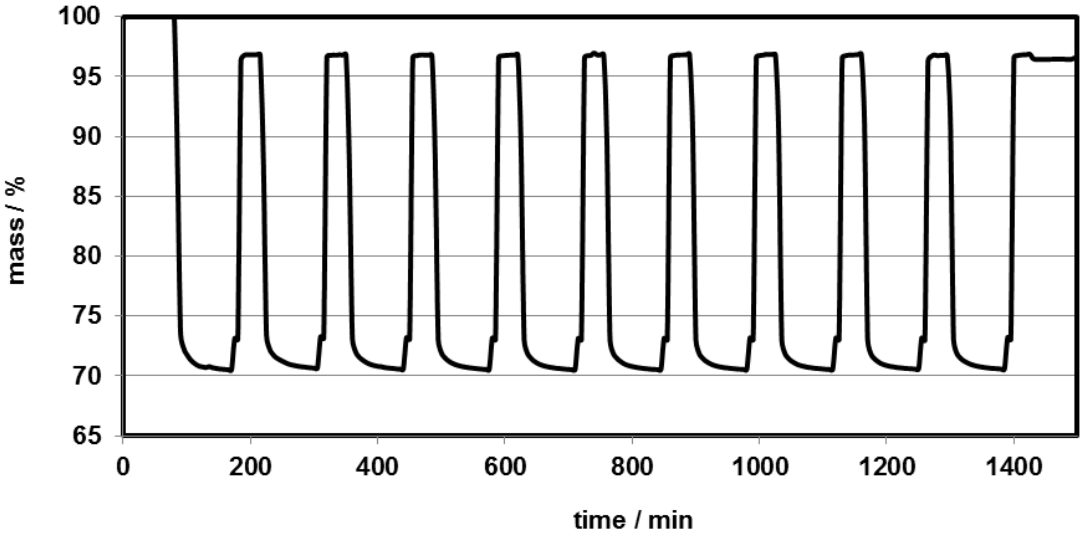

Figure 66: The isothermal measurement at 750 °C with the 10 % sample.

The magnification of the bar diagram in *Figure.67* shows that the mass exchange capability of the sample fell in the second cycle and rose up to the eighth repetition. In the ninth and tenth cycle the amount of exchanged mass decreased again.

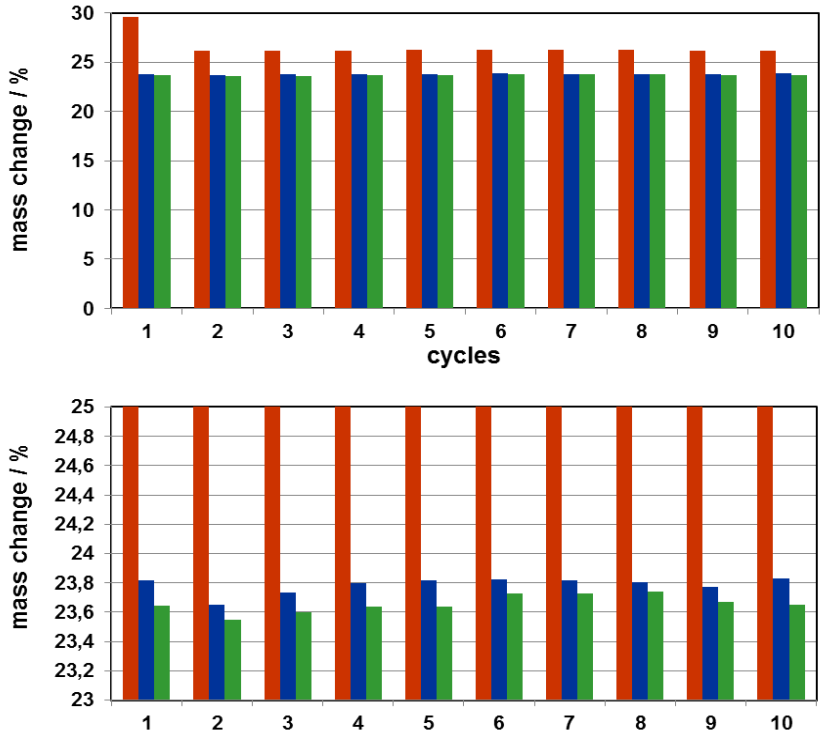

Figure 67: The bar diagram and the magnification of the tops of the bars.

The reductions in *Figure.68* look very similar to previous ones with the exception of the dynamic reductions. It is visible that the second reduction takes more time and does not reach the final mass level compared to the subsequent reductions. The second and third oxidations show a kink in the weight region of the wustite /magnetite

transition. This kink became smoother in the seventh and ninth cycle but was still visible. This behaviour could be caused by a kind of homogenization of the sample through the repeating redox cycles.

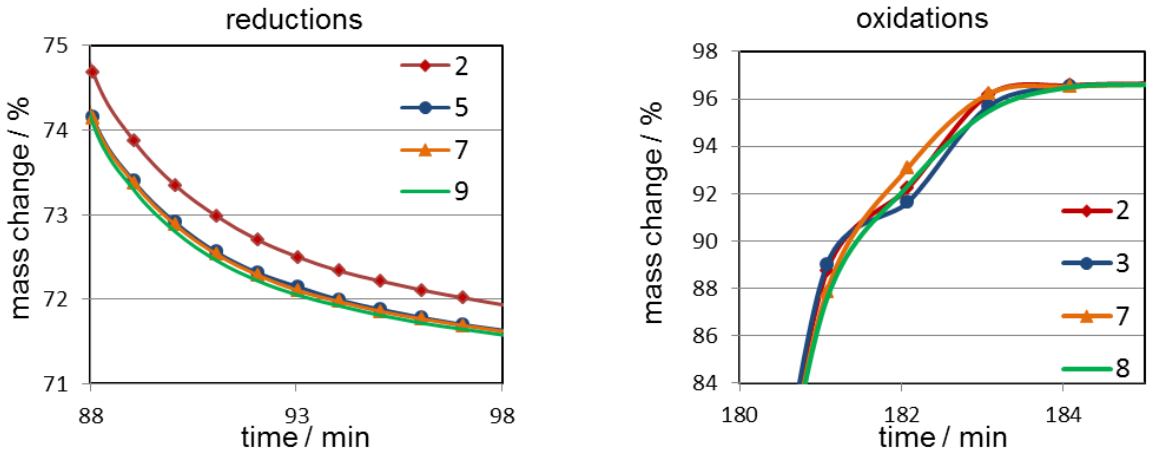

Figure 68: The single reductions (left) and the single oxidations with different shapes of the curves (right).

Discussion:

The entire measurement showed a good stability concerning the mass exchange capability. The reductions approximated their shape with consecutive cycling and it was challenging to separate the last cycles because they were very similar to each other. All the oxidations reached the same mass plateau in the same time. The differences in the shape of the oxidations signals are expected to be caused through structural changes of the sample. In comparison with the 5 % series at 750 °C the difference in the mass change was around 1.5 %. However the series looked very stable and showed no degradation of contact mass

4.3.6 Multi cycle measurement: 10 % sample @ Dynamic conditions:

Table 24: Reaction times and gas flows of the redox cycle measurement.

Reaction phase	time / min	N_2 / ml·min^{-1}	H_2 / ml·min^{-1}	H_2O / ml·min^{-1}
Reduction	10	40	60	
Purge	15/10	60		
Oxidation	10	60		80

The 10 % dynamic measurement was programmed in such way that the reaction times were reduced compared to the first dynamic measurement. This was done to

see the effect of an incomplete reduced sample in respect to the consecutive oxidation. The oxidation time was also reduced because the reaction times should fit each other. The complete measurement is shown in *Figure.69*.

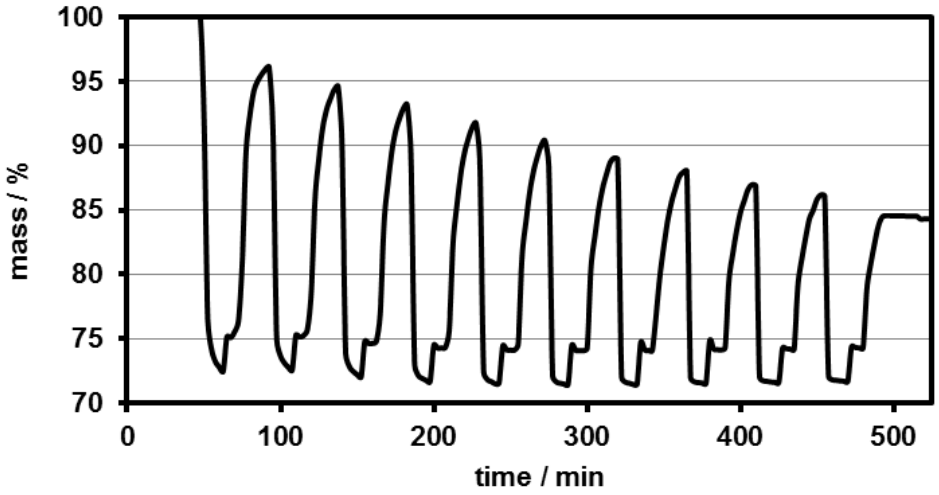

Figure 69: The performance of the 10 wt % sample during the dynamic measurement.

The first reduction led to a mass level of 72.38 % according to a mass change of 27.2 %. The first oxidation reached a level of 96.13 % but it is pointed out that the mass rises also after the oxidation period like in the first dynamic measurement. The oxygen exchange capability changes from 20.9 % in the first cycle to 10.2 % in the tenth cycle. This decrease denotes a loss in the capability of 10.6 % over ten cycles. The loss of the oxygen exchange ability is clearly pointed out in *Figure.70*. The bar diagram and the associated trend lines in the dot plot diagram *Figure.71* show a linear correlation between the cycle number and the exchanged mass during the reactions.

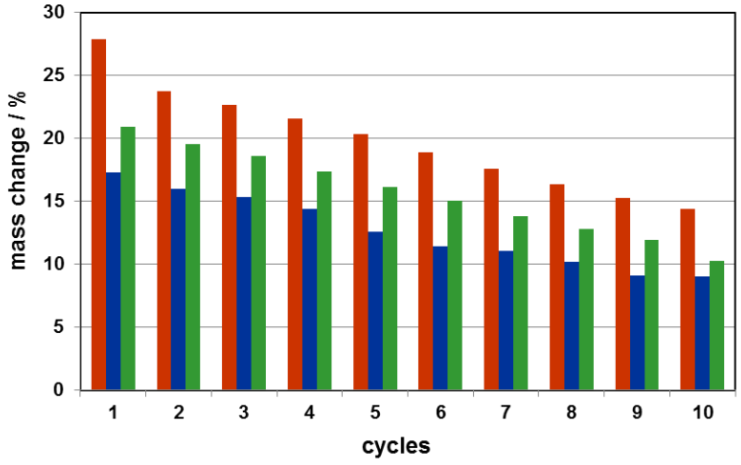

Figure 70: The bar diagram of the mass exchange during the different gas atmospheres.

4 Experimental Results and Discussion

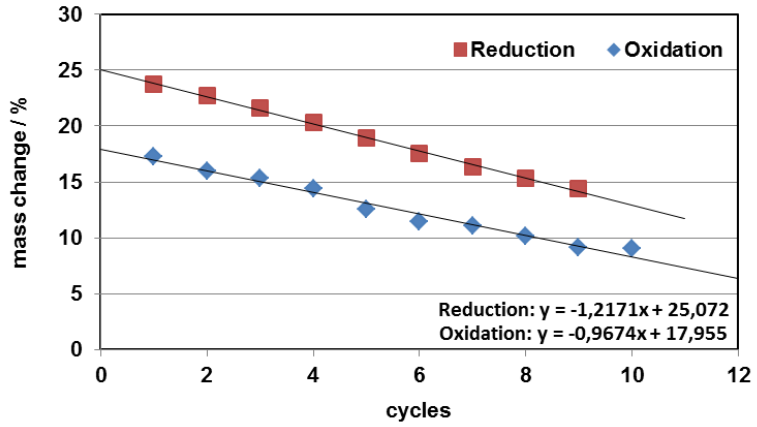

Figure 71: The almost linear decrease of the mass exchange capability of the 10 % sample.

The single reaction curves are represented in *Figure.72* and are indicating the trend of the stability. The reductions in *Figure.72* show a faster reaction kinetic in the later cycles and the reduction level was getting lower. The sixth and the eighth cycle reached a constant value and the reduction seemed to be completed. With a detailed examination this behaviour can also be seen in *Figure.69*. This performance is similar to the one of the 5 % sample with the difference that the 5 % sample was more stable over the first three cycles. The oxidations show the opposite trend. The slopes on the right side show a slower reaction kinetic in the later cycles and the oxidation states that are reached during the reaction are getting lower with repeating cycles. The reason for the behaviour of the sample during the reduction in the dynamic measurement was explained in the first dynamic measurement. Why the oxidation showed such a weak performance is open to speculation but too much dilution of the steam with the inert gas could be a reason. It was assumed that the steam access to the reactive iron was blocked or the oxygen insertion was affected by a diffusion barrier. As mentioned before the aluminium oxide acts as an oxygen barrier up to the wustite level and upon this oxide state the hercynite is the compound that causes the slow oxygen diffusion.

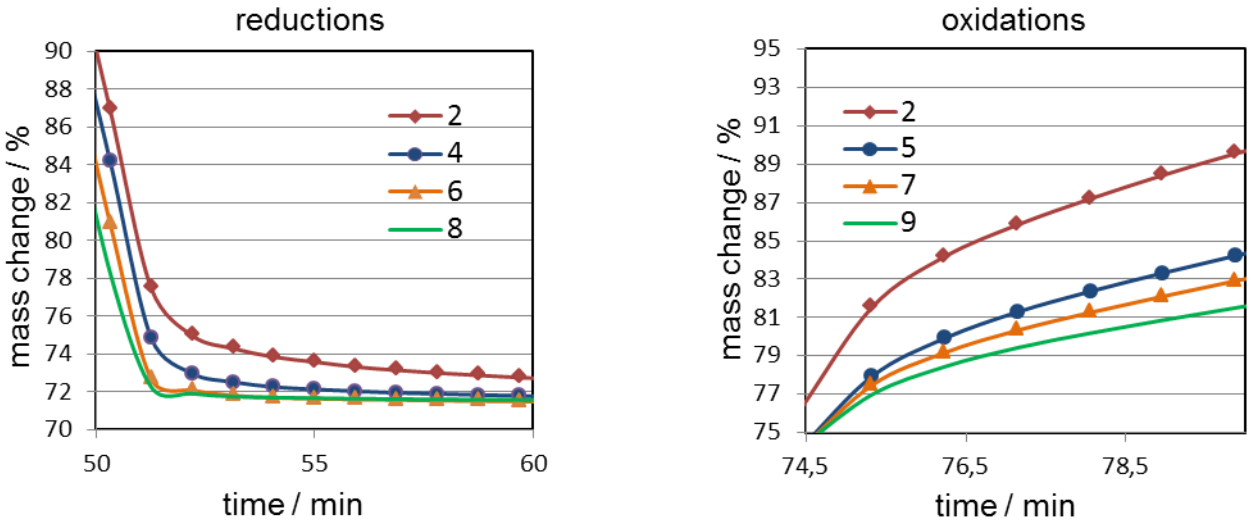

Figure 72: left: The reduction curves of the dynamic 5 % measurement (left) and the oxidation curves (right).

Discussion:

Both dynamic measurements did not have a constant mass level during the first few cycles. The last two reductions show a constant mass value. The oxidations continuously deteriorated over the repeating cycles. So the behaviour was similar to the 5 % sample.

4.3.7 Multi cycle measurement:

stabilized 20 % sample @ 600 °C:

Table 25: Reaction times and gas flows of the redox cycle measurement.

Reaction phase	time / min	N_2 / ml·min^{-1}	H_2 / ml·min^{-1}	H_2O / ml·min^{-1}
Reduction	75	60	90	
Purge	10	30		
Oxidation	20	30		80

The 20 % sample measurement showed an explicit mass decrease before the reduction phase. This mass decrease ended at around 97 % and fitted to the mass difference between haematite and magnetite. This mass decrease was assumed to be produced due residual hydrogen in the sample chamber. A little mass exchange decrease was observable during the first cycles but the sample showed a constant performance in the later cycles.

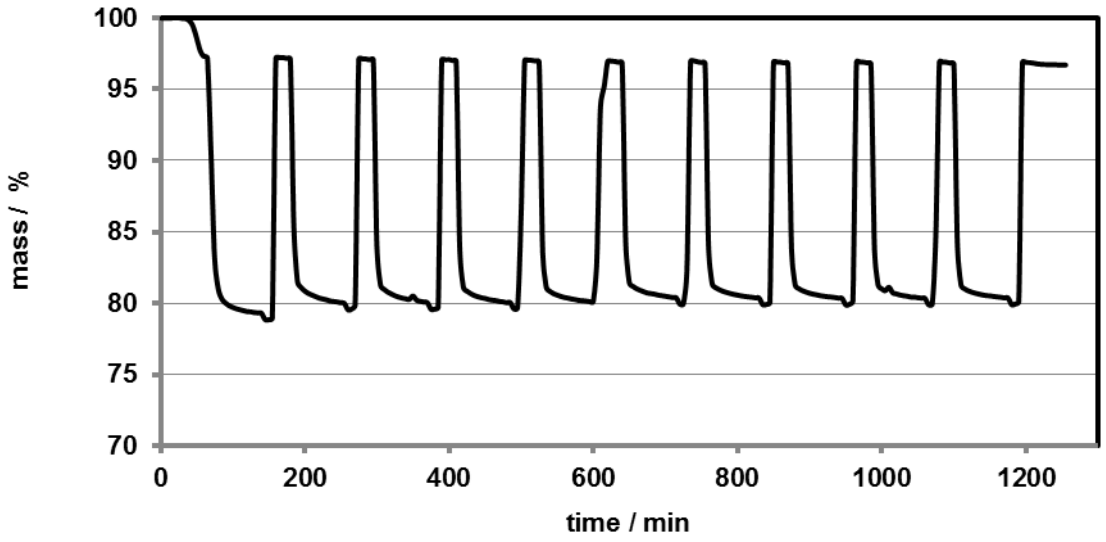

Figure 73: The performance of a 20 % sample at 600 °C.

During the third and ninth reduction a little peak was produced and the shape of his peak had a form that was typical for movement of the sample. This statement is related to the information that is delivered from the operation manuals of the thermo balance.

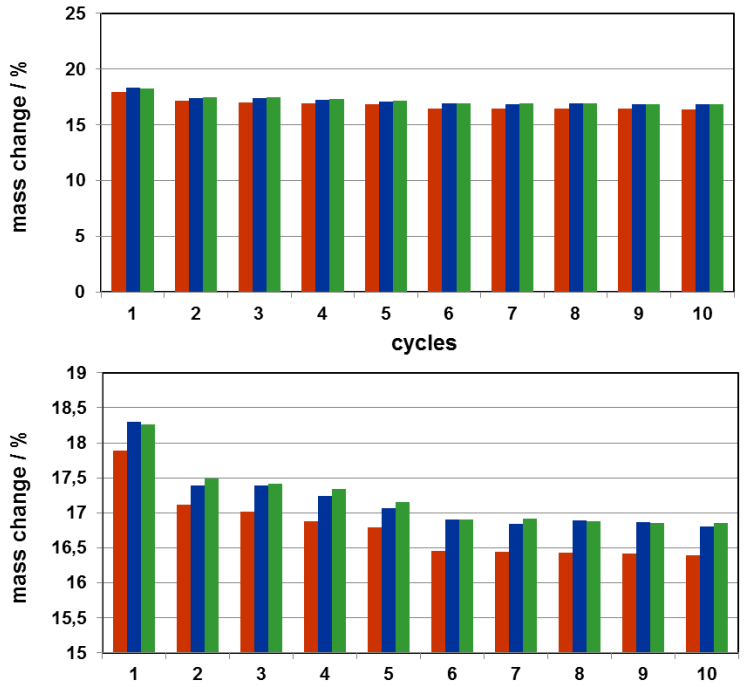

Figure 74: bar diagram of the isothermal 20 % sample at 600 °C.

The bar diagram in *Figure.74* shows the mass changes for all cycles. The magnification of the top of the bars clearly shows an initial decrease of exchanged mass. The first reduction reached a mass level of 79.3 % according to a mass change of 20.7 %.The theoretically calculated value would be around 24 %. This

discrepancy could be due to an inhomogeneous sample. The amounts of additive that was calculated and the measured concentrations are listed in *Table.13*. The first cycle was not considered here because the initial reduction would bias the results. The mass change in the second cycle was 17.5 % and evolved to 16.8 % in the tenth cycle. This denotes a decrease in the oxygen exchange capability of 0.7 % from the second to the tenth cycle.

Each cycle from the reduction *Figure.75* shows the same behaviour as it is reflected in the bar diagrams. The second cycle took more time to reach the same value as the later ones but led to a lower mass level and the final mass did not have a constant value. The fourth cycle showed a faster mass decrease than the second one but the final mass was a bit higher than in the second cycle. The eighth and tenth cycle looked very similar and seemed to be faster but with less oxygen removal compared to the earlier ones. All the oxidations were equal except the second one which had a higher mass level than the other ones. There was no distinct trend observable.

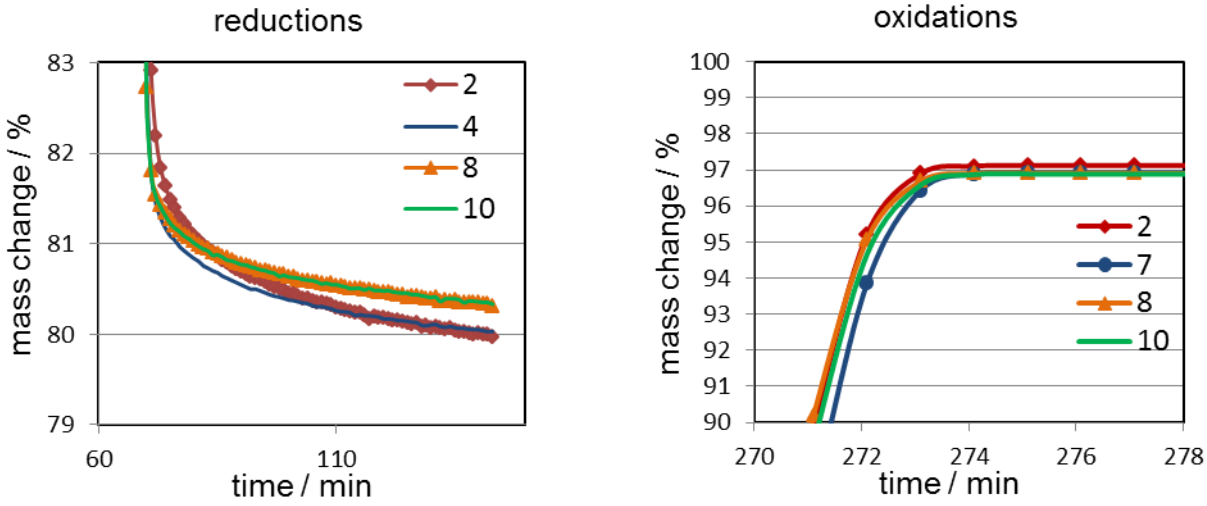

Figure 75: Single reduction curves of the 20 % sample at 600 °C (left) and the oxidations (right).

Discussion:

This series also showed a quite stable performance. A visible difference to the other series is that the reductions showed some peaks which were typical for pressure drops inside the furnace or abrupt movement of the sample. This is indicating that more aluminium content in the sample is promoting more mechanical stress. Another interesting result is that the failure of one purge phase did not affect the following cycles. The diagram shows that the program failed the purge step after the fifth reduction and started directly with the oxidation. This failure did not harm the contact mass in the following cycles. After a decreasing performance in the first cycles the sample showed a constant mass exchange capability.

4.3.8 Multi cycle measurement: Stabilized 20 % sample @ 750 °C:

Table 26: Reaction times and gas flows of the redox cycle measurement.

Reaction phase	time / min	N_2 / ml·min^{-1}	H_2 / ml·min^{-1}	H_2O / ml·min^{-1}
Reduction	60	30	100	
Purge	10	30		
Oxidation	45	30		80

This sample also showed a mass decrease before the reduction period. The measurement signal created a plateau at around 97 % according to the mass difference between haematite and magnetite. The reason for this behaviour was not totally understood but it was attributed to residual hydrogen in the sample chamber.

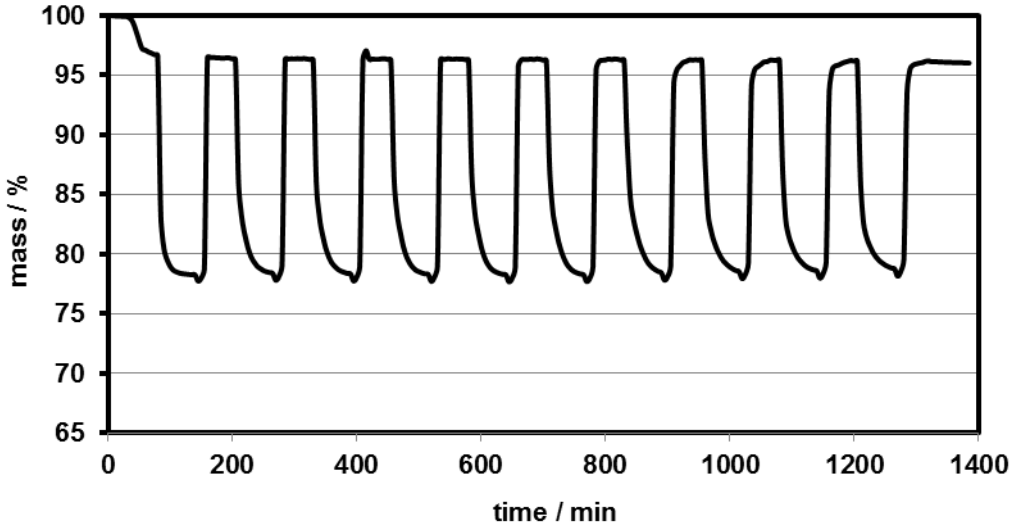

Figure 76: The complete measurement of the 20 % sample at 750 °C.

The bar diagram in *Figure.77* shows the mass changes of the sample over ten cycles. The first reduction ended at a mass level of 78.2 % and showed a constant value at the end of the reduction. The maximal calculated mass change was 24 % and the high amount of support material led to a mass change of just 21.8 %. The mass exchange capability developed from 18.6 % in the first cycle to 18.2 % in the tenth cycle which corresponds to a loss of the capability of 0.4 %. The maximal calculated mass exchange between the magnetite and the iron was determined to be 19.7 %. The bar diagram with the entire mass scaling looks very stable but the magnification of the tops of the bars show a constant loss in the mass exchange capability after six cycles. This continuous loss of capability is assumed to increase with consecutive reactions.

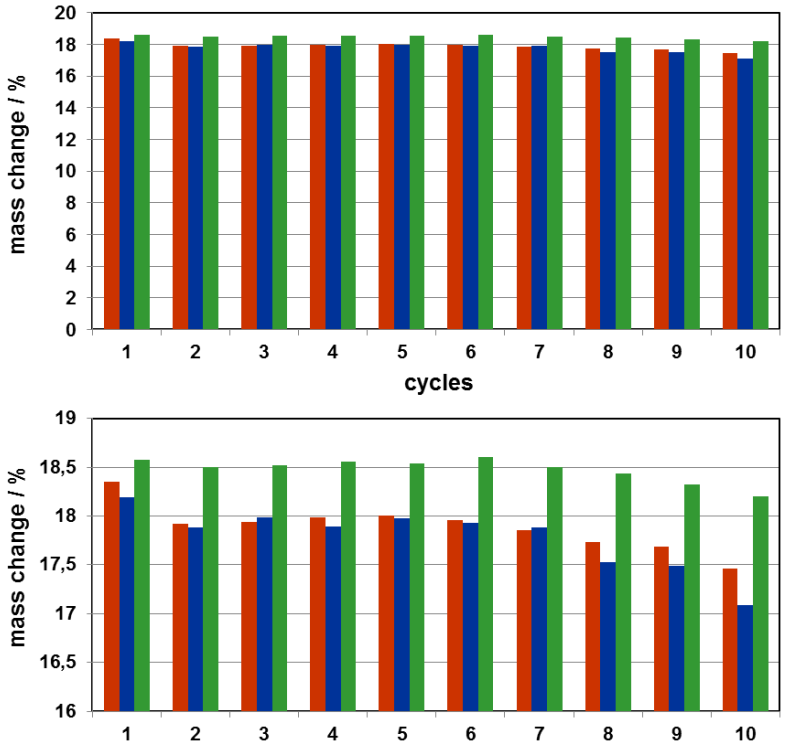

Figure 77: The performance of the 20 % sample at 750 °C and the magnification of the tops of the bars.

The magnification of the bar tops shows a variation of the capability over the first six cycles and a drop at the seventh cycle. The reductions and oxidations are represented in *Figure.78* and explain the results that are visible in the magnification of the bar diagram. The reductions showed a faster kinetic in the later cycles but the exchanged mass was lower than in the earlier reductions. The oxidations showed a slower kinetic with repeating redox reactions and the final desired mass took more time to reach the same value as the earlier ones. In the ninth cycle a kink in the slope appeared. As mentioned before the kink is located in the mass region of the wustite/magnetite transformation but additional research is necessary to identify the reaction mechanism that is acting here.

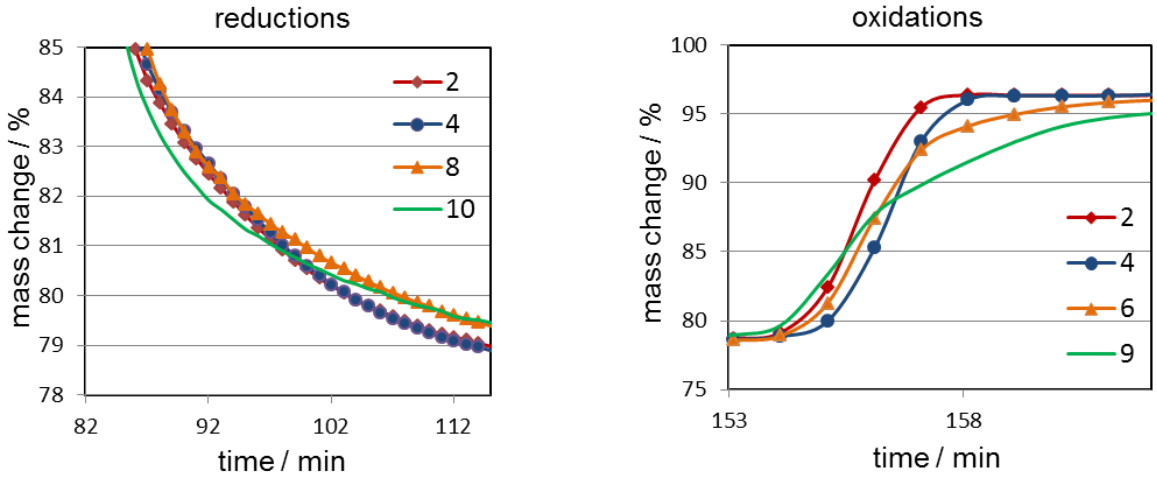

Figure 78: The single measurement curves of the reductions (left) and the oxidations (right).

Discussion:

An interesting result of this series is that the mass exchange capability shows a distinct decrease after the sixth cycle. By splitting the reductions in two phases the first one seems to get faster and the second one slower. This was the first measurement were the oxidation also showed a distinct trend and is getting slower with consecutive cycles. The slowdown of the oxidations is assumed to be caused by a change of the reactivity of the surface of the sample.

4.3.9 Multi cycle measurement: stabilized 20 % sample @ dynamic conditions:

Table 27: Reaction times and gas flows of the redox cycle measurement.

Reaction phase	time / min	N_2 / ml·min^{-1}	H_2 / ml·min^{-1}	H_2O / ml·min^{-1}
Reduction	75	30	120	
Purge	10	30		
Oxidation	30	30		80

The dynamic measurement was augmented to see if the short reaction times in the other dynamic measurements caused the weak performance of the sample. Here the initial signal also showed a mass decrease of around 3 %. The measurement that is represented in *Figure.79* showed some spurious effects. The first four cycles all developed a constant mass level and seemed to be completed. The following reductions looked like they completed but the oxidations showed weak performance and did not reach a constant value during the oxidation period.

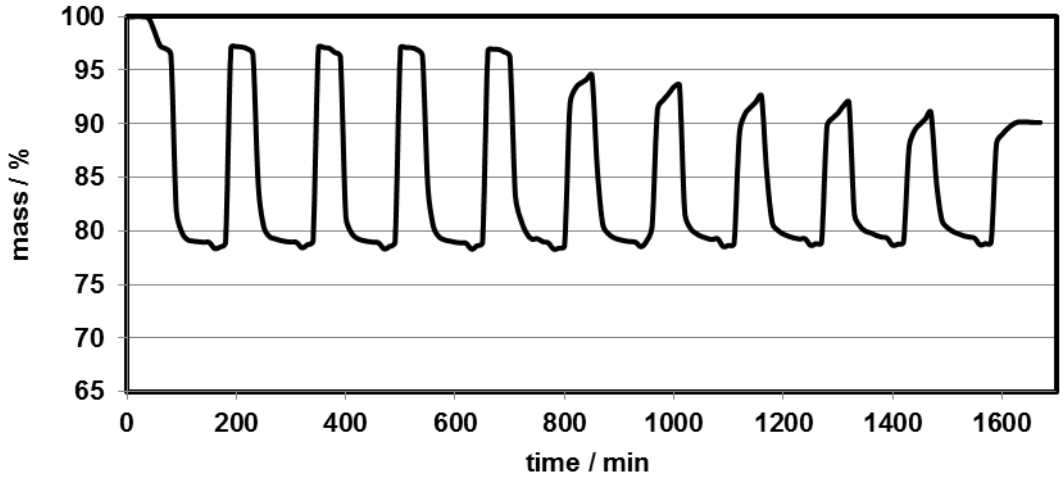

Figure 79: The measurement of the 20 % sample where the sample resisted a capacity decrease up to the fourth cycle but failed afterwards.

The first reduction reached a constant mass plateau at 78.8 %. The mass change of 21.2 % was smaller compared to the theoretical value of 24 %. The possible reasons were already discussed. The bar diagram in *Figure.80* clearly shows a stable performance over four cycles and a constant decrease afterwards. The mass change developed from 18 % in the first cycle to 11.4 % in the tenth cycle. The loss in the exchange capability was 6.6 % over ten cycles. In this case no magnification of the bar diagram was necessary.

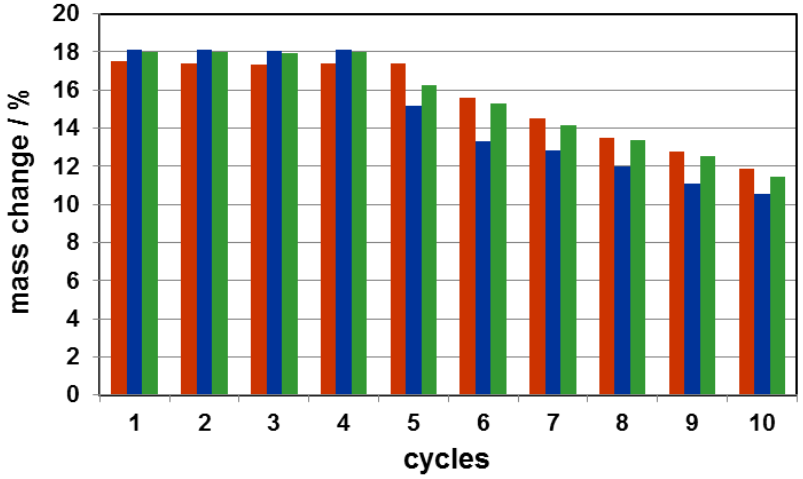

Figure 80: the bar diagram without the magnification of the tops.

The dot plot diagram in *Figure.81* shows a correlation between the mass exchange decrease and the cycle number.

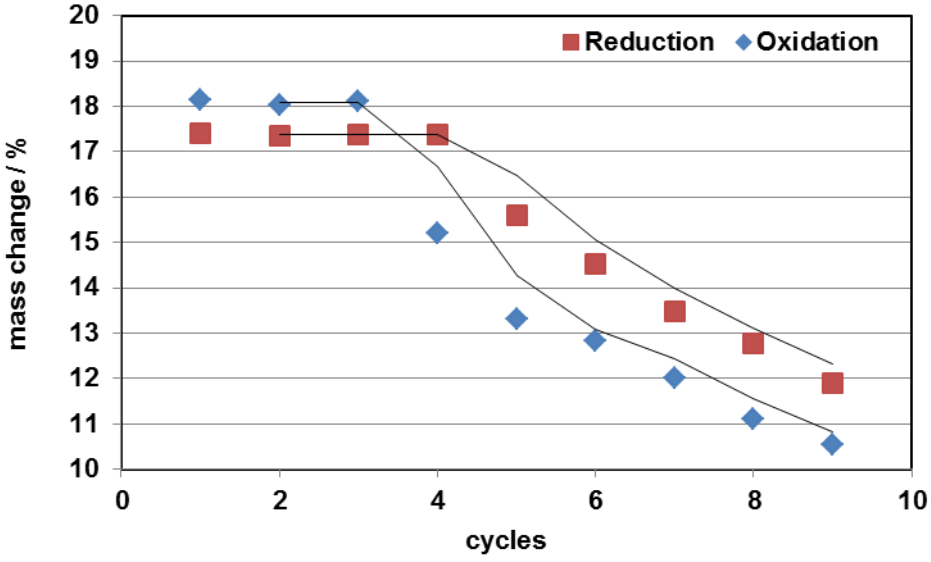

Figure 81: The trend line shows the breakdown of the stability of the contact mass after the fourth cycle.

The single reactions in *Figure.82* had a similar behaviour as the other dynamic measurements. The reductions became faster because they had always the same time to release a smaller amount of oxygen over the consecutive cycles. Also the fact that the final mass level was higher in the later reductions was similar to the other

ones. The oxidations showed a very distinct trend in terms of reaction kinetics and the final mass value. The first two cycles looked similar but the second one took more time to reach the same mass level as the first one. The last two oxidations showed a mass increase in the beginning and changed their shapes to a smooth curve. No kinks in the measurement curves like in the other series were observed.

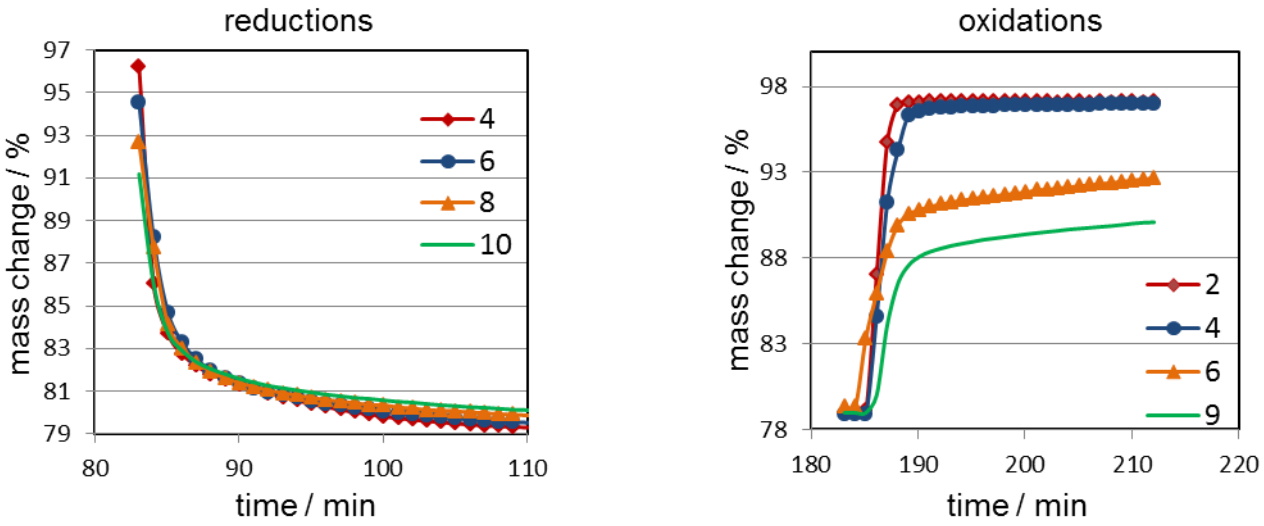

Figure 82: The single dynamic reductions (left) and the oxidations (right) of the dynamic 20 % measurement.

Discussion:

Interestingly the first four reductions seemed to perform like the isothermal measurements. Afterwards the sample showed the same behaviour as the other dynamic series. It should be noted that during the isothermal measurements the first few cycles altered in their mass exchange capability and showed a constant performance afterwards. In contrast this sample showed a stable performance in the beginning and the mass exchange capability decreased after the fourth cycle. This behaviour shows that it is not possible to reach a final conclusion if just some cycles are conducted. It seems that at least five to ten cycles are necessary to get an idea how the sample will perform in a long term application.

4.3.10 Long time measurement : Stabilized 5 % sample @ 600 °C:

Table 28: Reaction times and gas flows of the redox cycle measurement.

Reaction phase	time / min	N_2 / ml·min^{-1}	H_2 / ml·min^{-1}	H_2O / ml·min^{-1}
Reduction	15	60	120	
Purge	10	60		
Oxidation	15	60		80

To get an impression of the long time performance of the contact mass a measurement over fifty redox cycles was conducted. The reaction times were lowered and the gas flows were enhanced because of time limitations. *Figure.83* represents the entire measurement. The first reduction reached a value of 71.7 % and the first oxidation ended at 96.6 %. This mass exchange from 24.9 % is very close to the calculated maximal value of 25.7 %. This capability developed from an average of 24.68 % in the first ten cycles to 24.72 in the next ten cycles. The mean value for the next ten cycles was 24.79 % followed by 24.74 % in the following ten repetitions. The last ten cycles showed a mean value of 24.81 %.

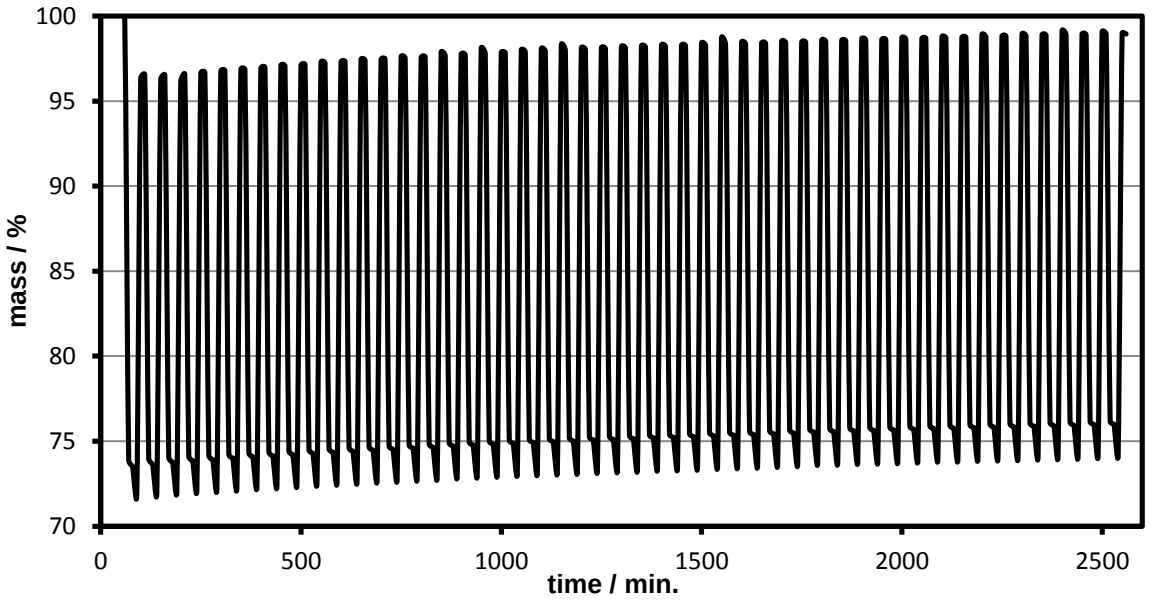

Figure 83: The fifty cycle measurement of the 5 % sample which shows a drift that is produced by the apparatus.

It is obvious that the apparatus showed a drift to higher values during this measurement. This drift did not influence the evaluation of the data because the drift changed the values into the same direction. The bar diagram with the entire mass scaling showed a very stable performance of the sample during the repeating redox cycles. The magnification of the bar diagram shows an altering performance that had the shape of a wave and is shown in *Figure.84*.

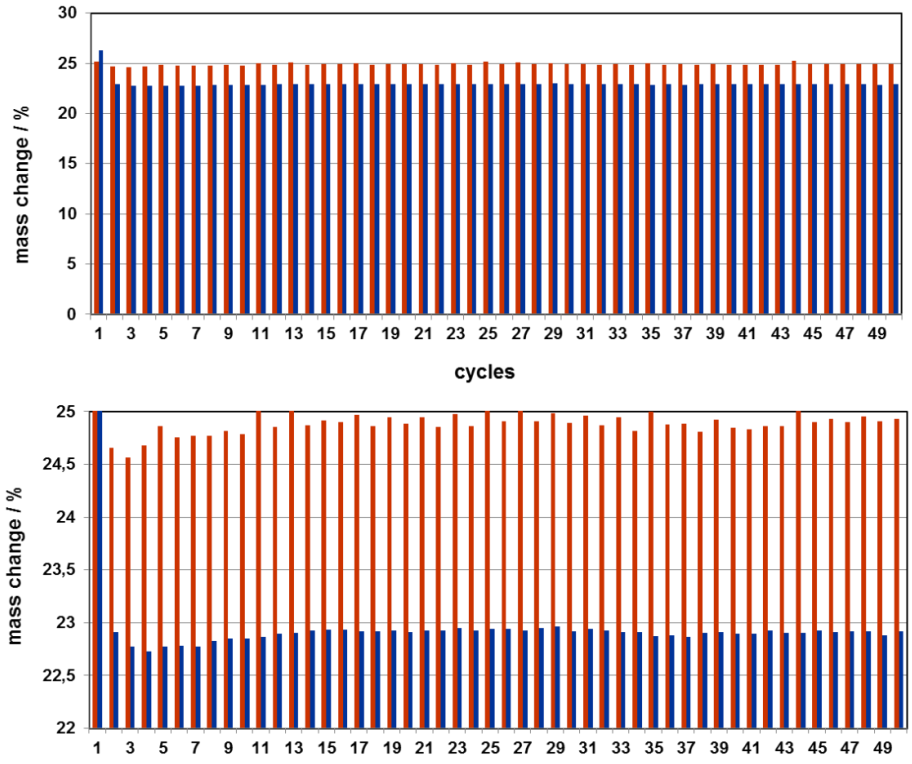

Figure 84: The bar diagram of the fifty cycle measurement with the magnification of the bar tops.

The dot plot diagram in *Figure.85* was chosen to represent the entire behaviour of the sample. The gradient of the trend line is positive and indicates that the performance becomes better in latter cycles. The consistency of the trend line is not good but this uncertainty came from the alternating performance that was described by the wavelike shape of the bar diagram before.

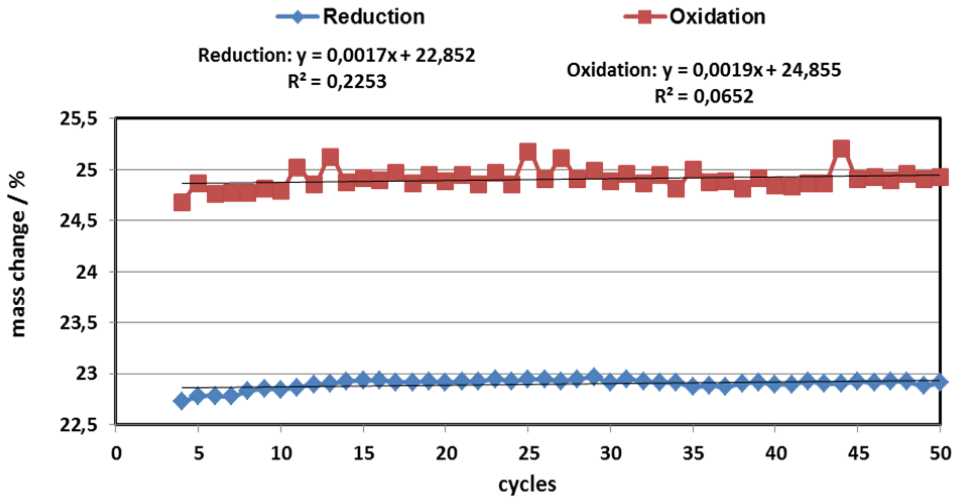

Figure 85: Dot plot diagram of the long time measurement with trend lines and the linear equation

Discussion:

This measurement shows a good performance of the sample and that the exchange capability increases with consecutive cycling reactions. The sample showed no agglomeration and was easily replaced from the sample carrier. The adjustments were set such that a lot of cycles could be conducted in a short time. Also with these adjustments the cycles completed

4.3.11 Long time measurement:

stabilized V2 sample (10wt %) @ 600 °C:

Table 29: Reaction times and gas flows of the redox cycle measurement.

Reaction phase	time / min	N_2 / ml·min^{-1}	H_2 / ml·min^{-1}	H_2O / ml·min^{-1}
Reduction	15	60	120	
Purge	10	60		
Oxidation	15	60		80

To compare a dry mixed and a wet impregnated sample a fifty cycle measurement also was done with the V2 sample. The reaction times and the gas flows were the same as for the wet impregnated sample. The first reduction ended at a mass level above 76 % indicating a blockage of the reaction. This blockage was not observable in the following cycles. There are some spikes visible during the oxidation and they are explained through little plugging effects at the exhaust of the measurement furnace. Also this sample showed a good stability over the entire measurement.

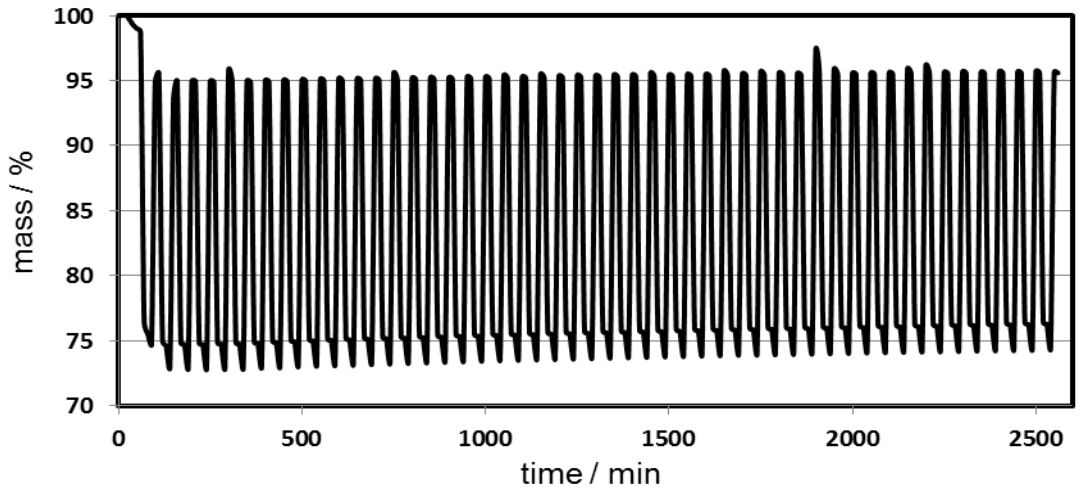

Figure 86: The long time measurement of the dry mixed V2 sample over fifty cycles.

4 Experimental Results and Discussion

The average mass exchange in the first ten cycles was about 21.74 %. That value was lower in the next ten cycles and was determined to be 21.71 %.From the twentieth to the thirtieth repetition the mean value was 21.58 % which decreased to 21,28 % over the ten following cycles. The last ten cycles showed an average mass change of 21.22 %. This results are also reflected in the bar diagram in *Figure.89*. The magnification shows a continuous loss in the exchange capability.

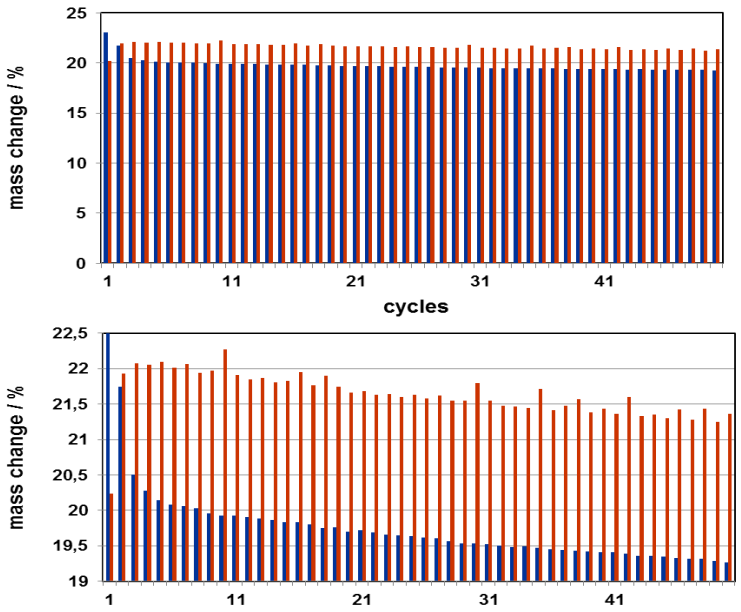

Figure 87: The stability decrease of the V2 sample over fifty cycles.

The dot plot diagram in *Figure.88* was chosen for the comparison with the wet impregnated 5 % sample. The gradient of the trend line has a negative value and shows the contrary trend than the 5 % sample.

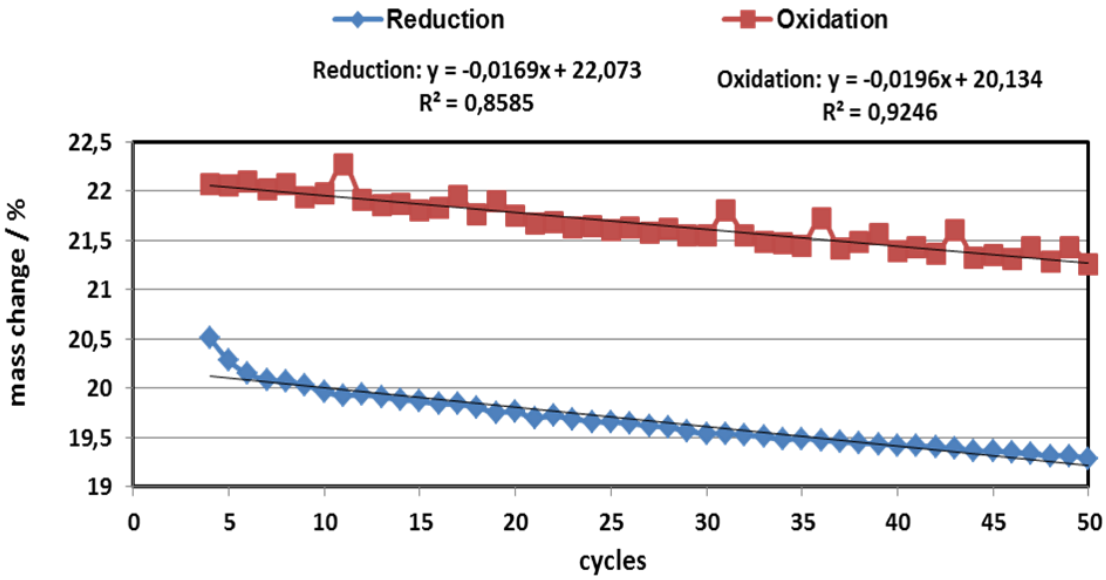

Figure 88: Dot plot diagram of the long time measurement with trend lines and the linear equation.

Discussion:

The behaviour of the dry mixed sample is assumed to be caused by an inhomogeneous distribution of the aluminium oxide on the sponge iron power. This heterogeneous distribution could cause agglomeration and consequently a lower amount of reactive iron would be present.

4.3.12 V7 powder measurement (10wt %) @ 750 °C:

Table 30: Reaction times and gas flows of the redox cycle measurement.

Reaction phase	time / min	N_2 / ml·min^{-1}	H_2 / ml·min^{-1}	H_2O / ml·min^{-1}
Reduction	60	30	100	
Purge	10	30		
Oxidation	30	30		80

The dry mixed powder sample showed an initial mass decrease. The signal developed a plateau at around 95 % and this value did not fit to any transformation of the oxides. The first reduction ended at 71.8 % and showed a constant mass value. The first oxidation ended at 94.9 % and also reached this value in all other cycles. The second and third reduction reactions seemed to reach a constant value but they were above the first reduction. After the third reduction the reaction did not come to an end and the amount of removed oxygen became lower with consecutive cycles.

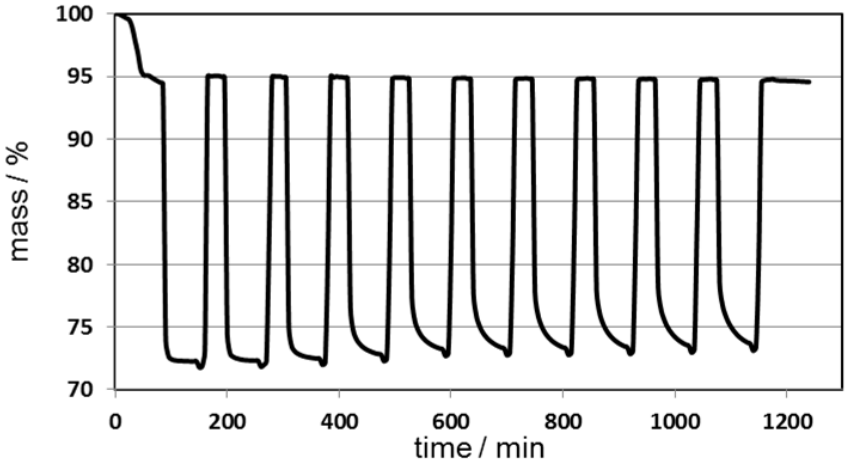

Figure 89: The V7 powder measurement over ten redox cycles at 750 °C.

The bar diagram in *Figure.90* shows the loss of the oxygen exchange ability. The mass exchange developed from 23 % in the first to 21.8 % in the last cycle. This is not a big deactivation but if this effect continues over more cycles this sample would not be feasible. Because of the weak stability no further evaluation was done.

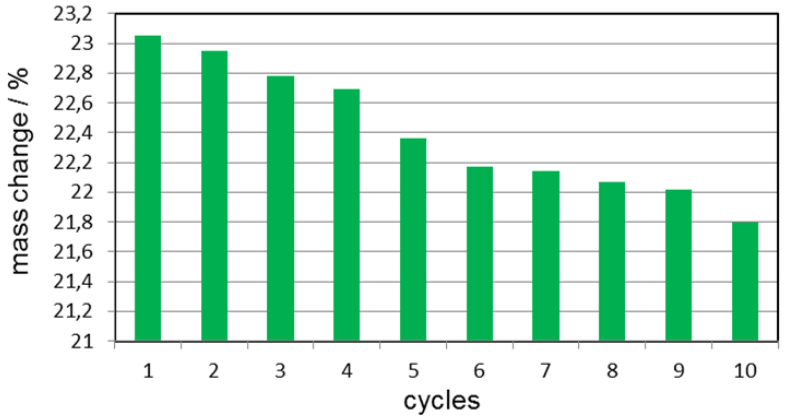

Figure 90: The performance of the V7 powder sample over ten redox cycles.

4.3.13 V7 pellet measurement (10wt %) @ 750 °C:

Table 31: Reaction times and gas flows of the redox cycle measurement.

Reaction phase	time / min	N_2 / ml·min^{-1}	H_2 / ml·min^{-1}	H_2O / ml·min^{-1}
Reduction	30	30	100	
Purge	10	30		
Oxidation	30	30		80

Pellets with a diameter between 0.5 and 1 mm were produced from the V7 powder sample. This was done because the industry and the researchers in the field of process engineering favour pellets much more instead of powders. This is especially valid for tubular reactors that are also used at this institute.

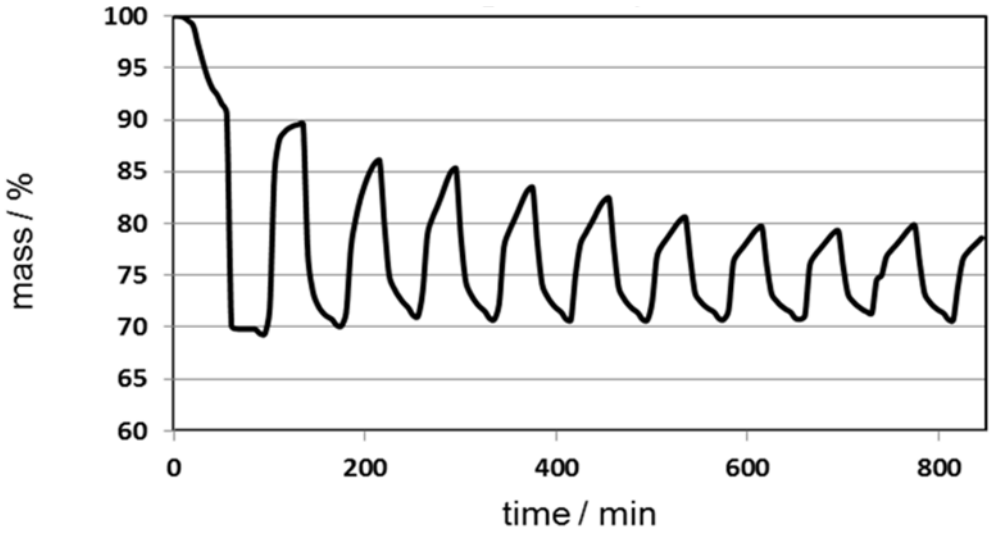

Figure 91: The performance of the pellet measurement over ten redox cycles.

The pellet measurement also showed a massive mass decrease during the heating period. The pellet measurement showed significant differences to the powder sample. The loss in the exchange capability was around 10 % which is ten times more compared to the powder sample. This bad performance was considered to be due to pore closing processes and other structural changes of the pellet. It has to be mentioned that the closing of the pores hinders the gases to reach the reactive sites and causes a lower mass exchange. Another important fact is that if a pore is once closed in one cycle this pore is not necessarily closed in another cycle. These closed pores lead to cavities inside the pellet and the cavities can built up pressure because of the reversible hydrogen oxidation like it is explained in *Figure.23*. These structural changes can also explain the different shapes of the measured curves. This result shows that a powder and a pellet measurement are not comparable. To get similar results between the powder and the pellet samples the adjustments of the pellet characteristics like the pore size and wall thickness have to be in an ideal balance. In our case it seems that the pores are closed even after the first cycle. One reason for this behaviour is that the oxidation had not enough time to proceed to reach a constant mass value. Another reason could be that after the first reduction tight iron is present inside the pellet and the steam was not able to re-oxidize this tight iron core. The following reduction would form a tight iron layer over the oxide scale and prevent the hydrogen from reaching the iron oxide that is located between the inner iron core and the outer iron layer. It seems that after the fifth cycle a kind of equilibrium situation was attained so the amount of exchanged oxygen stayed quite similar. Because of the weak stability no further evaluation was done.

5 Conclusions:

The average mass exchange capabilities of each sample at different temperatures are listed in *Table.32*. The mass exchanges of the isothermal experiments were calculated for the last four cycles, since the first few cycles showed instable performance. In order to determine the sample degradation, the dynamic experiments were evaluated over ten cycles.

Table 32: Summary of the average mass exchange capabilities

Samples: / Temperature Program:	5 %	5 % Nr.2	10 %	20 %	5 % / 50 cycles	V2 / 50 cycles	V7 / powder	V7 / pellet
600 °C	24.6	24.78	22.5	16.9	24.81	21.2	-	-
750 °C	25	25.05	23.65	18.35	-	-	22	9
Dynamic (loss over ten cycles)	12.6	-	10.6	6.6	-	-	-	-

The results of the theoretical and the measured examinations agree with results published in literature, like C.D Bohn claimed a smaller oxygen exchange capability with rising amount of support material [30].

The experiments showed a distinct relationship between the amount of support material and the change in mass. This correlation is attributed to two contrary effects of the support material. On one hand the support enhances the stability, on the other hand iron, the reactive part of the contact mass, is reduced. In addition the formation of the intermediate hercynite takes place. Hercynite is mixable with the iron oxides only in small amounts e.g. with magnetite which can be seen in *Figure.92*. Beyond this miscibility the hercynite forms precipitates which act like foreign particles and also have two effects. Firstly hercynite acts as an oxygen diffusion barrier. This phenomenon becomes noticeable after the first cycle. Secondly hercynite acts like a catalyst for the iron precipitation.

The main focus of this work was set on the stability of the contact mass and the results of the measurements show that it is possible to prevent the contact mass from agglomeration. **The longest measurement was conducted over fifty repeating redox cycling reactions with a 5 % sample. This sample showed a discrepancy of about 1 % compared to the calculated maximal value**. The results of the 5 % sample showed a stable performance in the isothermal measurements. The measurement with a reduction temperature of 750 °C and an oxidation temperature of 600 °C showed a distinct decrease in the mass exchange. The decrease of mass exchange during the dynamic measurements could be caused by phase separation processes and through cation distribution processes that had not enough time to reach there equilibrium state.

This assumption is based on the phase diagram of the magnetite-hercynite system that is shown in *Figure.92*.

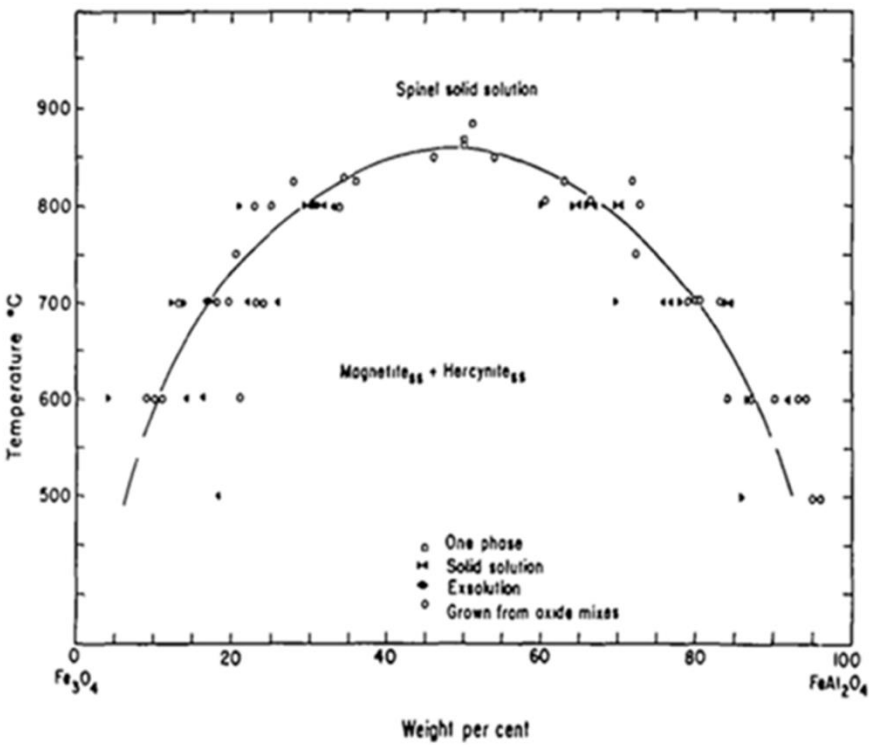

Figure 92: The miscible diagram of haematite and hercynite [100].

Magnetite and hercynite have both a cubic crystal system and a spinel structure. The spinel and the inverse spinel just differ in the arrangement of their cations. At high temperatures the cations can move and change their position leading to a change in the crystal structure e.g. form spinel to inverse spinel. If the temperature stays constant it can be assumed that one of the two spinel structures is favoured. If the temperature changes and no preferred structure can develop the cations will be thermodynamically instable. So it is assumed that the weak performance in the dynamic measurements can also be caused by changes of the crystal structure.

The reductions of the 5 % sample tended to a faster reaction kinetic in the later cycles. The oxidations showed no distinct trend and the shape of the measurement curves changed in some cases. This effect was attributed to structural changes in and outside the sample. The 10 % sample showed a similar behaviour with the difference of less oxygen exchange. Also in these measurements the reductions became faster later in the process. The oxidations showed no clear trend. The dynamic measurement conditions had a bad influence on the stability of the sample. Similar to the 5 % measurements a continuous degradation of the exchange ability was observed. The 20 % measurements also showed a stable performance during the isothermal measurements but the reductions were more hindered than in the other measurements. During the dynamic measurement the sample stayed stable over four cycles and showed an explicit decrease in the oxygen exchange capability afterwards. The dry mixed V7 sample showed a less stable performance compared

to the impregnated samples. This behaviour is attributed to an inhomogeneous distribution of the support material. The pellet measurement showed a fast deactivation and this is assumed to be caused through sintering effects inside the pores of the pellets.

With all the results and experience that was acquired during this work it was proven that the contact mass is able to process fifty redox reactions without any noticeable loss of the mass exchange capability. **By comparing each sample it can be seen that for an isothermal measurement the wet impregnated 5 % sample showed the best performance.** In the case of the dynamic measurements the 5 % sample showed the weakest stability. The 20 % sample showed the lowest mass exchange capability but showed best performance in the dynamic measurement. The 10 % sample showed a mean performance compared to the other samples. The dry mixed sample had the weakest performance in the isothermal measurement.

The results of this work show that a stable contact mass can be produced. This claim is valid for the reduction with hydrogen and the oxidation with steam. The low reaction kinetics can be dealt with in two basic ways. The first is to modify the aluminium oxide support and to lower the oxygen diffusion barrier. The second is to add chemical or physical promoters to the iron oxide matrix. For a chemical support the alkali and earth alkali elements are believed to fasten up the reaction. For physical promoters large ions are inserted into the iron oxide matrix and spread the lattice. The widening of the lattice causes faster oxygen diffusion and accelerates the reactions. The difficulty with these additives is that it is not predictable how they will influence the performance of the iron oxide.

Another aspect that is very important for the efficiency of the whole process is the kind of reactor that is used. Tubular reactors have the benefit that they are compact, robust and easy to maintain. These reactors open the opportunity to produce pressurized hydrogen which increases the efficiency if hydrogen storage is intended.

Further research should focus on a more practical use of the contact mass in terms of industrial reduction gas compositions and pellet geometries. The gas composition that is available from industrial processes mostly consists of a mix of H_2/CO and CO_2. The carbonaceous gas compounds tend to deposit solid carbon on the contact mass with a resulting loss of reactive surface and impurities in the hydrogen. Also the applicability of pellets should be more investigated.

.

6 References:

[1] International Energy Agency, 'WORLD ENERGY OUTLOOK 2015', www.iea.org, 2015

[2] J. G. Canadell, C. Le Quéré, M. R. Raupach, C. B. Field, E. T. Buitenhuis, P. Ciais, T. J. Conway, N. P. Gillett, R. Houghton and G. Marland, "Contributions to accelerating atmospheric CO2 growth from economic activity, carbon intensity, and efficiency of natural sinks.," Proc. Natl. Acad. Sci. U. S. A., vol. 104, no. 47, pp. 18866–70, Nov. 2007

[3] T. Malthus and V. Smil, "Why Malthus Got His Forecast Wrong," p. 1–5, 2014

[4] J. Chow, R. J. Kopp, and P. R. Portney, "Energy resources and global development" Science, vol. 302, no. 5650, pp. 1528–31, Nov. 2003

[5] M. Mehrara, "Energy consumption and economic growth: The case of oil exporting countries," Energy Policy, vol. 35, no. 5, pp. 2939–2945, May 2007

[6] P. Refi and P. Trade, "BP Statistical Review of World Energy About this review Contents," June, 2014

[7] www.uni-stuttgart.de/hi/gnt/ausstellungen/zeppelin/3.1_wasserstoff.html. 2014

[8] M. Selan, J. Lehrhofer, K. Friedrich, K. Kordesch, and G. Simader, "Sponge iron : economic, ecological, technical and process-specific aspects and gas conditioning," vol. 61, pp. 247–253, 1996

[9] P. Kurzweil, "Brennstoffzellentechnik," Springer Vieweg, p. 5–7, 2012

[10] www.hydrogeit.de/bz-typen.htm, 2014

[11] www.weltderphysik.de/gebiet/technik/energie/speichern-und-transportieren/strom/brennstoffzellen/metallpartikel/, 2014

[12] S. Helmut and R. Anderl, "Leistungsvergleich von Nieder- und Hochtemperatur- Brennstoffzellen – Experimentelle Untersuchungen, Modellierung und numerische Simulation," August, 2010

[13] N. Armaroli and V. Balzani, "The hydrogen issue.," ChemSusChem, vol. 4, no. 1, pp. 21–36, Jan. 2011

[14] H. Hofbauer, "Brennstoffzellentauglicher Wasserstoff aus Biomasse mittels Dampfreformierung," 2012

[15] J. Ada, L. F. De Diego, F. Garcı, P. Gaya, A. Abad, and M. L. Casta, "Selection of Oxygen Carriers for Chemical-Looping Combustion," no. 3, p. 371–377, 2004

6 References

[16] V. A. Heinzel and B. Vogel, “Reformierung von Kohlenwasserstoffen” no. 3, 2000

[17] S. Czernik, R. French, C. Feik, and E. Chornet, “Biomass Thermoconversion Processes,” pp. 4209–4215, 2002

[18] www.fz-juelich.de/iek/iek-3/DE/Forschung/BGE/Brennstoffzellenseiten/Gasnachbehandlung/Wasser-Gas- Shiftreaktion/_node.html p. 3, 2014

[19] J. D. Holladay, J. Hu, D. L. King, and Y. Wang, “An overview of hydrogen production technologies,” Catal. Today, vol. 139, no. 4, pp. 244–260, Jan. 2009

[20] www.ipc.uni-stuttgart.de/demokurs/Elektrolyseur.pdf, pp. 1–13. , 2014

[21] http://www.biofachforum.ch/chemrep/redox4e2.html, 2014

[22] T. Smolink, M. Günther, J. Garche, “Stand und Entwicklungspotential der Wasserelektrolyse zur Herstellung von Wasserstoff aus regenerativen Energien’’NOW-Studie, Frauenhofer ISE, FCBAT, Revision.1, 2011

[23] I. Abe, “Alkaline Water Electrolysis’’ Energy Carrier and Conversion Systems, office terra, Japan, Vol.1, 2009

[24] A. Meier, and C. Wieckert, “Wasserstoff aus Wasser und Sonnenenergie.” www.pre.ethz.ch Bulletin SEC/AES 24/25, 2005

[25] S.Hurst, “Production of hydrogen by the steam iron method,” Oil Soap, vol. 16, no. 2, 1939

[26] B. H. Lane, “THE LANE HYDROGEN PRODUCER” www.flightglobal.com/pdfarchive/view.html, 1909

[27] www.dingler.culture.hu-berlin.de/journal , D.F.G., 2014

[28] V. Hacker, “A novel process for stationary hydrogen production: the reformer sponge iron cycle (RESC),” J. Power Sources, vol. 118, no. 1–2, pp. 311–314, May 2003

[29] V. Hacker, R. Fankhauser, G. Faleschini, H. Fuchs, K. Friedrich, M. Muhr, and K. Kordesch, “Hydrogen production by steam–iron process,” J. Power Sources, vol. 86, no. 1–2, pp. 531–535, Mar. 2000

[30] C. D. Bohn, “The Production of Pure Hydrogen with Simultaneous Capture of Carbon Dioxide,” Dissertation, University of Cambridge, 2010

[31] M. Thaler and H. Raupenstrauch, “Kontaktmassenentwicklung für den Metall-Dampf-Prozess zur Erzeugung und Speicherung von Wasserstoff für Brennstoffzellen” Dissertation, Technische Universität Graz, 2009

6 References

[32] http://www.fhi-berlin.mpg.de/acnew/department/pages/teaching/pages/teaching__wintersemester__2007_2008/schmidt_catalyst_preparation_021107.pdf

[33] L-S. Fan, ‘‘Chemical Looping Systems for Fossile Energy Conversion‘‘, AIChE, The Ohio State University Columbus, Wiley, s.84, 2010

[34] M. Thaler and V. Hacker, “Storage and separation of hydrogen with the metal steam process” Int. J. Hydrogen Energy, vol. 37, no. 3, pp. 2800–2806, Feb. 2012

[35] http://webmineral.com/data/Hematite.shtml, Miner. Data Publ., no. 3, 2005

[36] www.a-m.de/deutsch/lexikon/eisenoxid.htm, 2014

[37] www.geodz.com/deu/d/Morin Phasenübergang , 2014

[38] www.ep4.ruhr-uni-bochum.de/imperia/md/content/skripte/ss05/mediziner/festkröpermagnetismus.pdf Festkörpermagnetismus.” 2014

[39] http://dieckmann.mse.cornell.edu/Teil06.PDF, pp. 284–297., 2014

[40] www.tu-ilmenau.de/fileadmin/media/wt/Lehre/Seminare.pdf, 2013

[41] W. Scherer and A. Reller, www-4.physik.uni-augsburg.de/chemie/lehre/downloads/pdfxws0607fkch/chemIII_WS06-07_02.pdf” 2014

[42] M. E. Fleet, “The Structure of Magnetite,” Acta Crystallogr,vol. 24, no. B, pp. p917–p920, 1981

[43] www.chemie.de/lexikon/Magnetit.html. 2014

[44] http://webdoc.sub.gwdg.de/ebook/diss/2003/fu-berlin/2003/12/Kapitel2.pdf, 2003

[45] www.wmi.badw.de/teaching/Lecturenotes/magnetismus/Kapitel-1.pdf. 2005

[46] E. D. Wyckoff, R. W. G. Crittenden, “Herstellung und Kristallstruktur von Ferrooxyd” Zeitschrift fuer Krist., vol. 63, pp. p144–p147, 1926

[47] www.mineralienatlas.de/lexikon/index.php/MineralData?mineral=Wüstit, 2014

[48] http://gestis.itrust.de/nxt/gateway.dl, no. wustite, p. 1190, 2014

[49] http://ruby.chemie.uni-freiburg.de/Vorlesung/metalle_8_5.html,” p. 8, 2013

[50] “http://www.chemie.de/lexikon/Wustit.html,” p. 3, 2014

6 References

[51] H.-J. Engell, “Über die Reduction von Wüstit, Magnetit und Eisen - Mangan - Mischoxide,” Springer, p. p.5 – p.8, 1969

[52] P. Jun-Woo, K. Sung, C. Suk-Ho, and L. Hosun, “Optical Properties of Transition-metal Oxides of MnO and Fe 0.925 O Crystals Studied with Spectroscopic Ellipsometry and Raman Spectroscopy,” New Phys. Sae Mulli, vol. 63, no. 7, p. 818, Jul. 2013

[53] A. W. Hull, “Crystal structure of alpha-iron,” Phys. Rev., vol. 10, no. 1917, pp. p661–p696, 1969

[54] K. Schubert, “Ein Modell für die Kristallstrukturen der chemischen Elemente,” Acta Crystallogr. Sect. B Struct. Crystallogr. Cryst. Chem., vol. 30, no. 1, p. 193–204, Jan. 1974

[55] Y. Zhang, J. R. G. Evans, and S. Yang, “Corrected Values for Boiling Points and Enthalpies of Vaporization of Elements in Handbooks,” J. Chem. Eng. Data, vol. 56, no. 2, pp. 328–337, Feb. 2011

[56] http://universal_lexikon.deacademic.com/75260/Eisenschwamm. 2013

[57] https://roempp.thieme.de/roempp4.0/do/data/RD-01-01812. 2013

[58] http://gestis.itrust.de/nxt/gateway.dll/gestis_de. 2013

[59] E. L. Owen, E.A.; Yates, “Precision measurements of crystal parameters,” Philos. Mag., vol. 7, pp. p472–p488, 1955

[60] A. F. Holleman and E. Wieberg: Lehrbuch der Anorganischen Chemie. p.91-100, Walter de Gruyter, Berlin New York 1985

[61] H. D. Lewis, J. Schwarzenbach and D. Flack, “Electric field gradients and charge density in corundum, alpha-Al2O3,” vol. 38, pp. p733–p739, 1982

[62] R.J. Hill “X-ray powder diffraction profile refinement of synthetic hercynite “American Mineralogist, vol.69, p937-p942, 1984

[63] B. Hou, H. Zhang, H. Li, and Q. Zhu, “Study on Kinetics of Iron Oxide Reduction by Hydrogen,” Chinese J. Chem. Eng., vol. 20, no. 1, pp. 10–17, Feb. 2012

[64] W. K. Jozwiak, E. Kaczmarek, T. P. Maniecki, W. Ignaczak, and W. Maniukiewicz, “Reduction behaviour of iron oxides in hydrogen and carbon monoxide atmospheres,” Appl. Catal. A Gen., vol. 326, no. 1, pp. 17–27, Jun. 2007

[65] E. Lorente, J. Herguido, and J. A. Peña, “Steam-iron process: Influence of steam on the kinetics of iron oxide reduction,” Int. J. Hydrogen Energy, vol. 36, no. 21, pp. 13425–13434, Oct. 2011

6 References

[66] K. Piotrowski, K. Mondal, H. Lorethova, L. Stonawski, T. Szymanski, and T. Wiltowski, “Effect of gas composition on the kinetics of iron oxide reduction in a hydrogen production process,” Int. J. Hydrogen Energy, vol. 30, no. 15, pp. 1543–1554, Dec. 2005

[67] D. Yu, M. Zhu, T. a. Utigard, and M. Barati, “TGA kinetic study on the hydrogen reduction of an iron nickel oxide,” Miner. Eng., vol. 54, pp. 32–38, Dec. 2013

[68] K. Piotrowski, K. Mondal, H. Lorethova, L. Stonawski, T. Szymanski, and T. Wiltowski, “Effect of gas composition on the kinetics of iron oxide reduction in a hydrogen production process,” Int. J. Hydrogen Energy, vol. 30, no. 15, pp. 1543–1554, Dec. 2005

[69] W. Schatt,“Einführung in die Werkstoffwissenschaften Schatt,” Alfred Hüthig Verlag, Heidelberg, 6. Auflage,p. 74. Nov. 1995

[70] J. N. Bogdandy, L. ; Schulz, H.P. ; Würzner, B. ; Stranski, “Der Mechanismus der Reduktion von porigen Eisenerzen durch Wasserstoff,” Arch. für das Eisenhüttenwes., p.401 – 409, 1963

[71] K. Landler, P. Komarek, “Reduction of Wustite within the Wustite Phase in H_2-H_2O mixtures” Trans. Metall. Soc. Aime, vol. 236, no. Heft.23, p.138 – 149, 1966

[72] H. W Gudenau, W.-G. Buchard, Schiller, M. , “ Ausscheidungsverhalten von Eisen auf Wüstit während der Reduktion“ Prozeßkinetik und Prozesstechnik im Hüttenwesen, DFG – Sonderband 1986, Verlag Stahl Eisen, 1986

[73] M.Ottow, “Ursachen der Zerstörung von Hämatitpellets aus sehr reinem Magnetitkonzentrat während der Reduktion und Versuche zur Qualitätsverbesserung “ TU Berlin, F. f. Bergbau u. Hüttenw, 1966

[74] http://www.google.com.do/patents/US6569377; 2014

[75] http://abulafia.mt.ic.ac.uk/shannon/ptable.php., 2014

[76] H. C.Schaefer, “Mechanismen der Ausscheidung von Eisen aus Wüstit bei der Reduktion von Eisen-oxiden: In-Situ Untersuchungen im Rasterelektronenmikroskop unter Hochtemperatur- und Reduktionsgas-einwirkung,” 1984

[77] H. Kortmann, K. Koch, B. Grover, O.Burghardt, G. Trömel,“Bedeutung der Gangart für das Schwellverhalten von Eisenerzpellets,“ Stahl und Eisen 93, S. 463 – 471.,” vol. 93, 1973

[78] H. W. Gudenau, “Eisenerzreduktion in der Wirbelschicht mit Wasserstoff reichen Gasen. “ Aachen, 1998

6 References

[79] Y. M. Shin, “Corex plant in Posco,” in Meeting of the VDEh blast furnace committee and the committee for metallurgical fundamentals in Düsseldorf, Fachausschussbericht 0,020, p. 20. 1993

[80] V. V. Boldyrev, M. Bulens, B.Delmon,” The control of the reactivity of solids” Elsevier Scientific Publishing Company, Amsterdam, 1979

[81] K. Watts, A. Young, C. McG Bowling, “Batch reduction of iron ore with hydrogen in a fluidized bed,” Trans Instn Min. Met., vol. 97, no. june, pp. S.61–71, 1988

[82] G. Schürmann , E. Willems, J. Sommer, “Sauerstoffabbaugeschwindigkeit bei der Reduktion von Eisenerzen mit einem Gasgemisch aus Kohlenmonoxyd, Kohlendioxyd, Wasserstoff und Stickstoff,” Arch. für das Eisenhüttenwes., vol. 1, no. 35. Jahrgang. 1964

[83] H. Shigematsu, N. Iwai, “Effect of the addition of Al2O3 and CaO on the reduction of dense wustite with hydrogen,” Trans. ISIL, vol. 24, p. 72, 1989

[84] R. Degel,“Stickingvermeidung im Fluidatbett in Wasserstoffhaltiger Atmosphäre“; Dissertation RWTH - IEHK, Aachen,” p. 5. 1996

[85] W. D. Piepenbrock, R. Koch, K. Trömel, G. Fix, “Über den Verlauf der Reduktion von Wüstit mit Zusätzen an Fremdoxiden,” Arch. für das Eisenhüttenwes., vol. 3, no. 47 p.141–146, 1976

[86] A.Galerie, Y.Wouters , M.Caillet , “ The Kinetic Behaviour of Metals in Water Vapor at High Temperatures: Can General Rules be Proposed ?, “ Mater Sci. Forum, no. 231, p.369 – 372, 2001.

[87] A. Rahmel, J. Tobolski, “Einfluß von Wasserdampf und Kohlendioxyd auf die Oxydation von Eisen-Silicium-Legierungen in Sauerstoff bei Temperaturen von 750 bis 1050°C.” Werkstoffe und Korrosion,“ p. 662-676 Corros. Sci.; 5; p.333, 1965.

[88] A. Rahmel, “Das Verhalten von Stählen gegen Korrosion durch heisse Gase, Verbrennungsprodukte und Schmelzen ,“ Werkst. Korros., no. 16, p. 662, 1968

[89] S. Hayashi , T. Narita, ”Competitive Effect of Water Vapor and Oxygen on the Oxidation of Fe–5 wt.% Al Alloy at 1073 K,” Oxid. Met., no. 56, p. 251, 2001

[90] S. M. Klotsman, A. N.Timobeyev, I. Sh. Traktenberg,” Nonstochiometric Oxides,“ Phys. Met. Metall.; p.228, vol. 93, 1960

[91] R. Lundner , Ark. Kemi, vol. 4, p. 381, 1952

[92] W.W. Schmelzer, D.J. Young , “Prog.Solid State Chem. “ vol. 10, p.17, 1975

[93] L. Himmel , R. F.Mehl, C. E. Birchenall , “Trans. AIME,“ no.197, p.827, 1953

6 References

[94] W.C. Hagel, Trans. AIME , no. 179, p. 236, 1966

[95] J. H. Swisher, E.T. Turkdogan, Trans. AIME; no. 239; p. 426, 1967

[96] J. Paidassi , Rev. Met., vol.54, p.569, 1957

[97] H. Li, J. Zhang, and D. J. Young, “Oxidation of Fe–Si, Fe–Al and Fe–Si–Al alloys in CO2–H2O gas at 800°C,” Corros. Sci., vol. 54, pp. 127–138, Jan. 2012

[98] D. J. Young, “Effects of Water Vapour on Oxidation 10.1.,” Corros. Ser., p. 455–495, 2006

[99] D. J. Young, “Oxidation of Pure Metals,” Corros. Ser., vol. 1, no. High Temperature Oxidation and Corrosion of Metals, pp. 81–137, 2008

[100] D.J. Young “Corrosion Series Volume 1“High Temperature Oxidation and Corrosion of Metals,” vol. 1, p.1-574, 2008 of Metals,” vol. 1, p.1-574, 2008

[102] D.J Young “Corrosion Series Volume 1“,Chapter 6, Alloys II:,p. 247-314

[101] W. Christ, A. Rahmel, M. Schütze, Oxid. Met. ; vol.1, p.31, 1989.

[103] P. Hancock, R.C.Hurst, “Advances in Corrosion Science and Technology,“ M. G. Fontana and R.W. Staehle, New York, vol .4, p.1, 1974

[104] www.chem.pku.edu.cn/instlab/pdf/ONLINETRAIN/SDT2960-DSC2010-3.pdf

[105] www.personal.uni-jena.de/~cim/AnleitungTA.pdf. 2014

[106] www.tf.uni-kiel.de/matwis/amat/def_en/kap_2/basics/b2_1_6.html, 2014

[107] www.chemie.uni-hamburg.de/ac/prosenc/1196091354/v6.pdf, 2014

[108] http://gasifiers.bioenergylists.org/node/188, 2014

[109] H. P. Eugster, “Fe — Al Oxides : Phase Relationships,” vol. 3, 1962

[110] C.A. F. Yen, “Electric Conductivity in the FeO-Fe_2O_3-Al_2O_3-SiO_2 System,” 1977

[111] www.centralclubs.com/ellingham-richardson-diagram-t66760.html, 2014

[112] D. J. Young, Corrosion Series Volume 1, vol. 1, p.1–574, 2008

[113] http://chemie.degruyter.de/riedel/data/figure/05/16/104/image.jpg

7 Appendix:

Table 1: Explanation of the acronyms for the different fuel cell types and their operation temperature.

Fuel cell types (acronym)	Fuel cell types (full name)	Operating temperature of the fuel cell types
AFC	Alkaline fuel cell	80 °C
PEMFC	Proton exchange membrane fuel cell	80 – 120 °C
DMFC	Direct methanol fuel cell	90 – 120 °C
PAFC	Phosphoric acid fuel cell	200 °C
MCFC	Molten carbonate fuel cell	650 °C
SOFC	Solid oxide fuel cell	1000 °C

Table 2: The different types of fuel cell systems with their specifications [9].

Fuel Cell	Power [kW]	el. Efficiency [%]	Application
AFC	10 – 100	Cell: 60 – 70 System: 60	Aerospace and automobiles
PEMFC	0,1 – 500	Cell: 50 – 70 System: 30 – 50	Aerospace and automobiles
DMFC	0,01 – 1	Cell: 20 – 30	Small devices
PAFC	≤ 10 000	Cell: 55 System: 40	Small Power plant
MCFC	≤ 100 000	Cell: 55 System: 50	Power plant
SOFC	≤ 100 000	Cell: 60 – 65 System: 55 _ 60	Power plant and APU

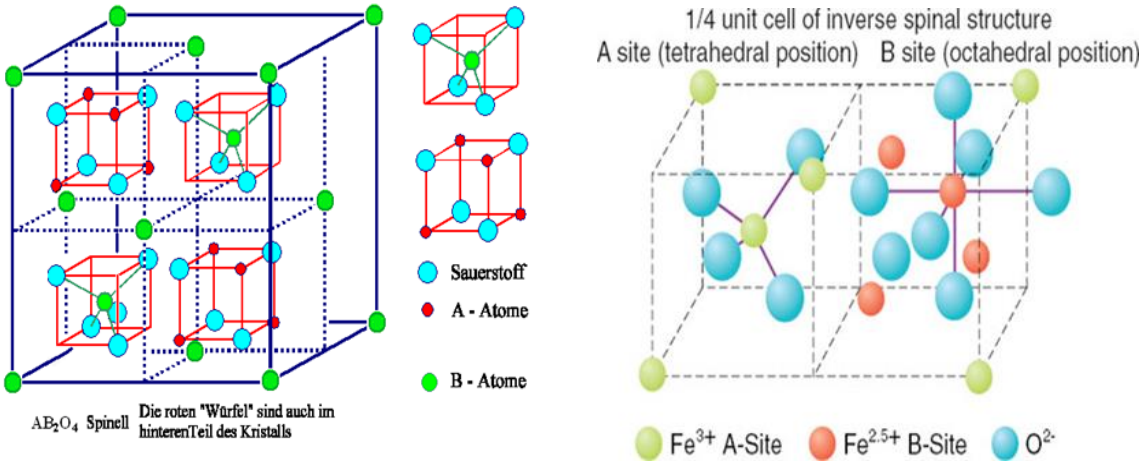

Figure 1: The structure of a spinel crystal. The red cubes are also present in the back of the big unit cell but they are inverted [105].

7 Appendix

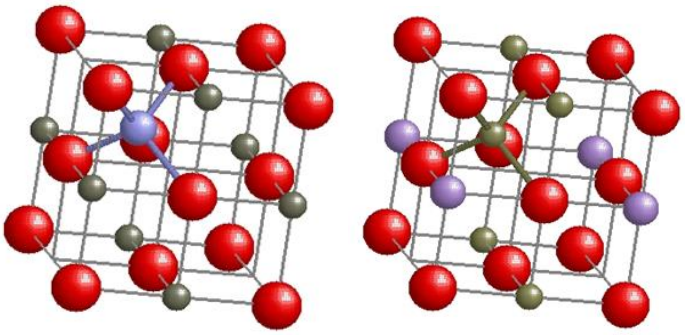

Figure 2: The normal spinel structure (left) and the inverse spinel structure (right). red: oxygen ions; violet: Fe^{+3} ions; grey: Fe^{+2} ions [106].

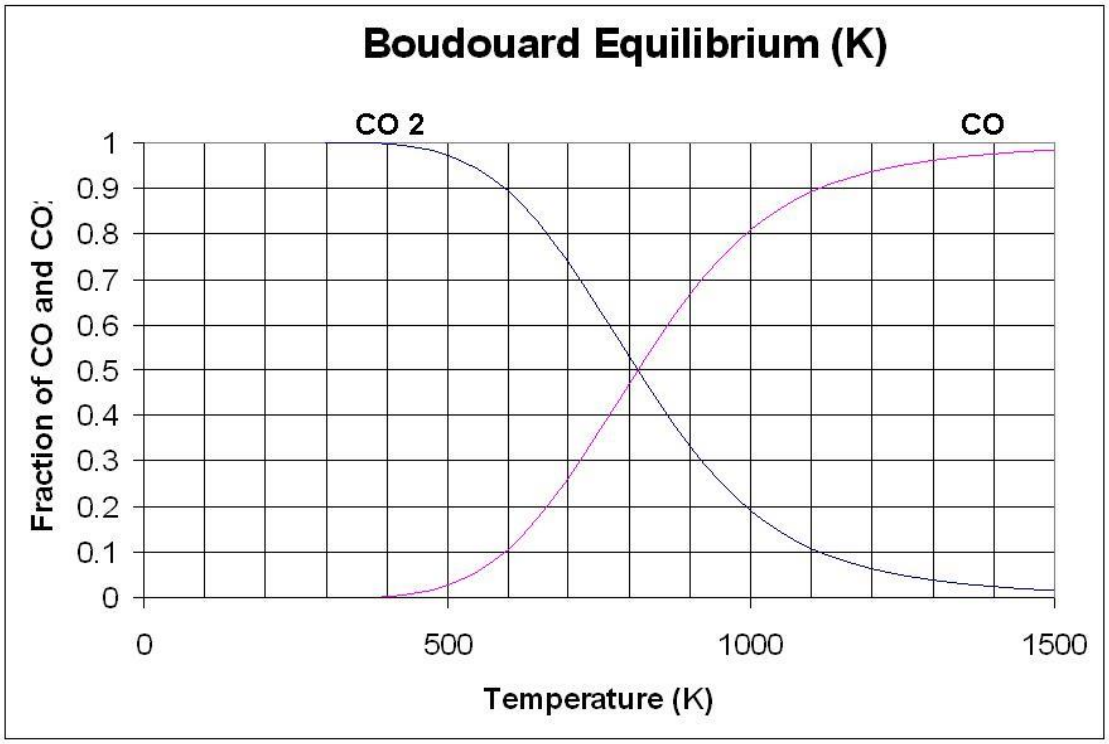

Figure 3: The Boudouard diagram showing the ratios of CO/CO_2 according to the temperature [107].

7 Appendix

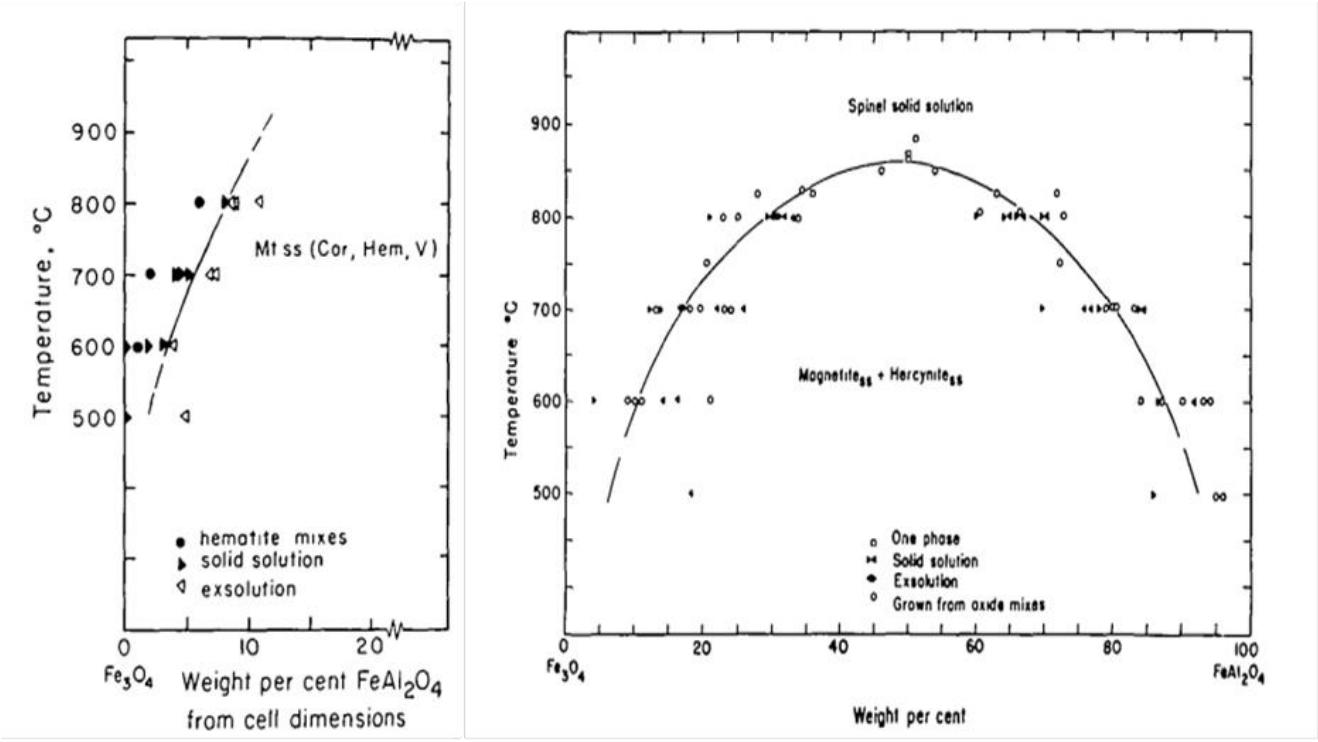

Figure 4: The miscibility diagram of the $FeOAl_2O_3$ / Fe_3O_4 system [97].

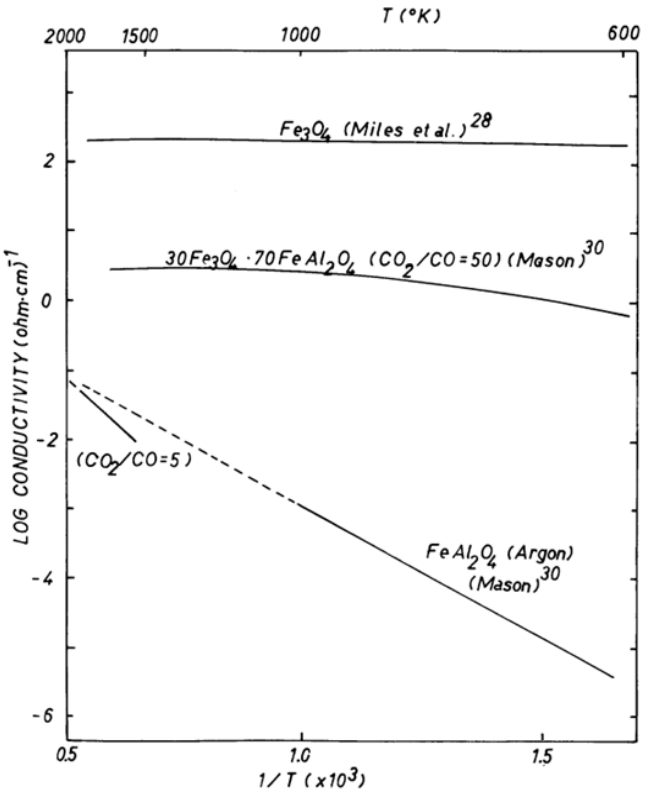

Figure 5: The conductivity diagram shows the effect of hercynite compounds in magnetite[110].

7 Appendix

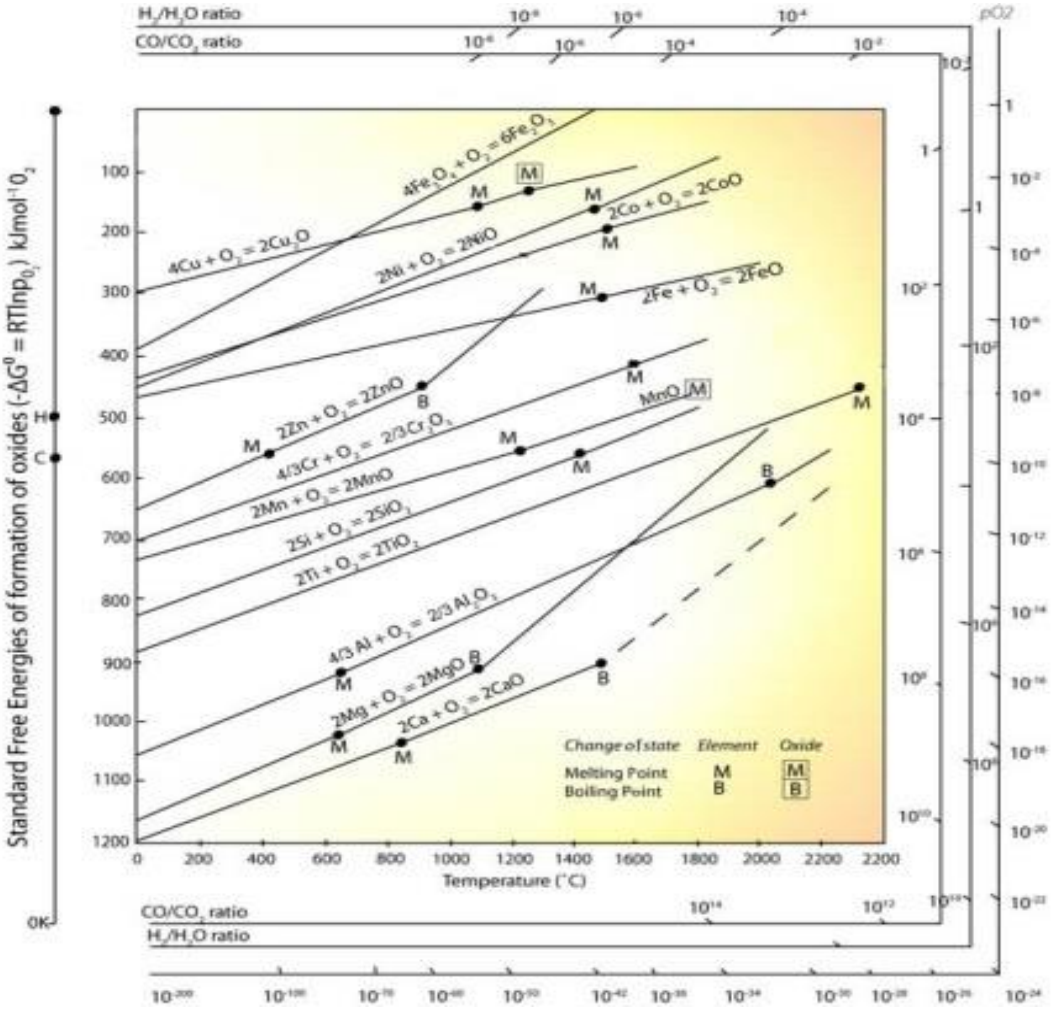

Figure 6: The Richardson diagram reflecting the standard Gibbs free energy of the metal oxidation reaction for different metals and oxidation states in different atmospheres and temperature. The lines that are lower in the diagram show that the according metal oxidation is favoured in respect to the higher ones. e.g. aluminium is much easier oxidized than iron [111].

7 Appendix

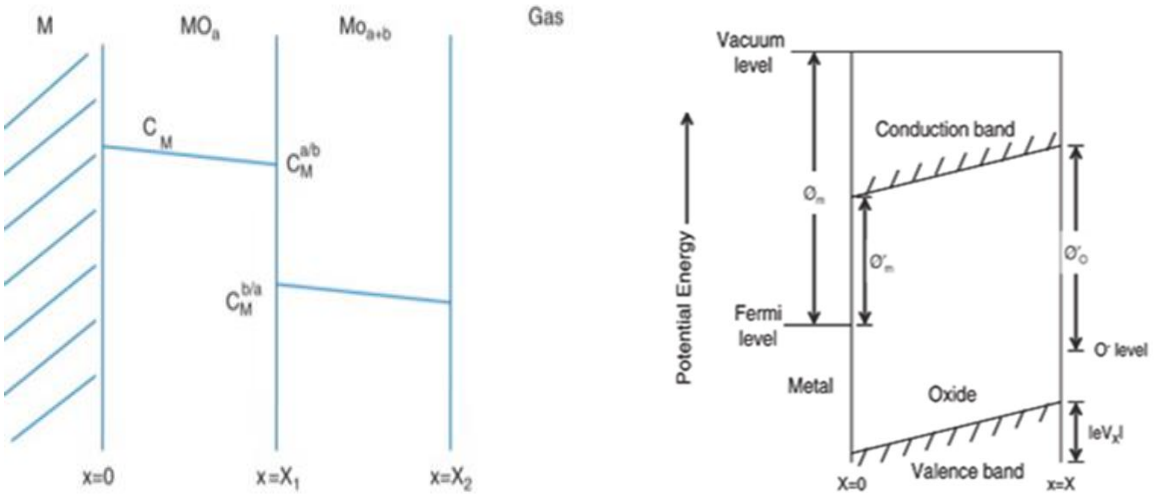

Figure 7: The different species that occur during oxidation and the according concentration differences (left). The schema of the potential energies according to the metal, the first oxidation state and the oxygen in the atmosphere (right) [111, 112].

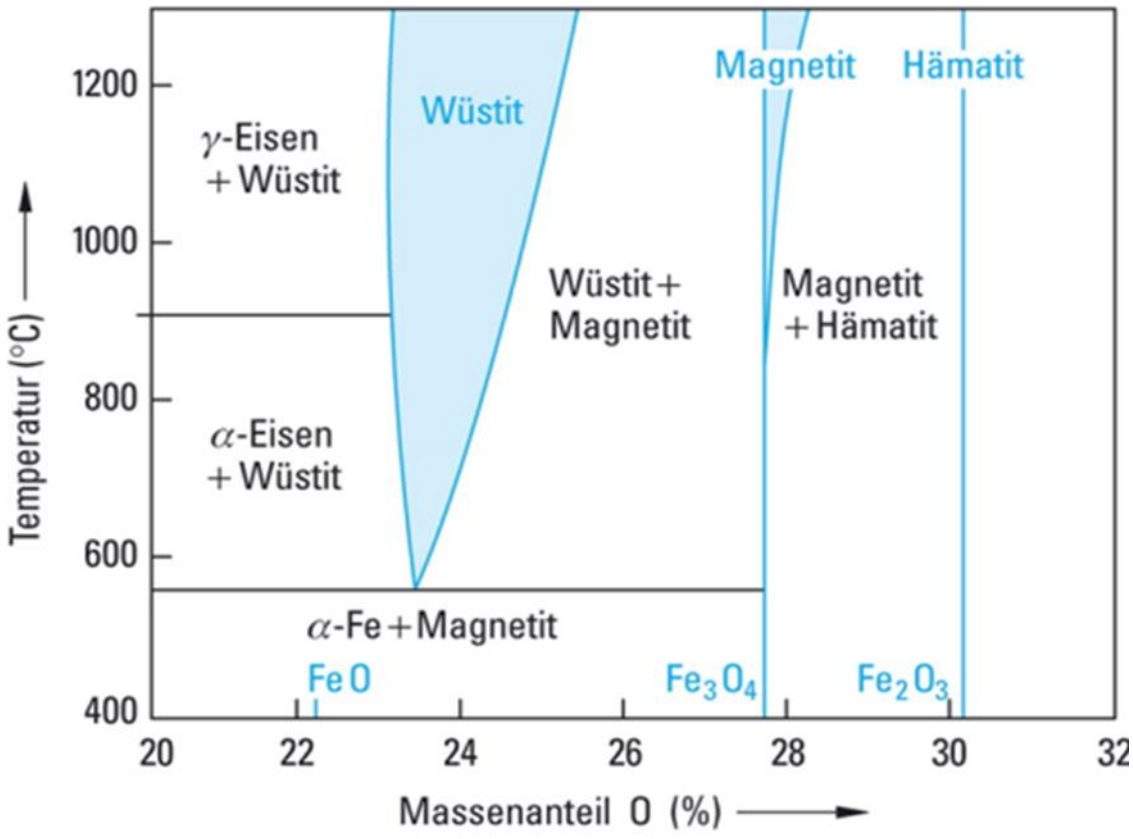

Figure 8: For better illustration of the Baur Glaessner diagram the iron oxygen equilibrium diagram is shown here and it is highlighted that in most cases the different oxides coexist in the same temperature region [113].